



POLITECNICO DI MILANO
FACOLTÀ DI INGEGNERIA INDUSTRIALE
CORSO DI LAUREA IN INGEGNERIA AERONAUTICA

**FINITE ELEMENTS MODELING OF GUIDED
WAVE PROPAGATION IN COMPOSITE
LAMINATES FOR STRUCTURAL HEALTH
MONITORING APPLICATIONS**

Relatore: prof. Giuseppe SALA
Co-relatore: ing. Alessandro AIROLDI

Tesi di Laurea di:
Michele CÈ Matr. 718653

ANNO ACCADEMICO 2009 - 2010

Sommario

La continua necessità dell'industria aerospaziale di ridurre i costi, ma di mantenere alti standard di sicurezza ha portato allo sviluppo di applicazioni di Structural Health Monitoring (SHM). L'obiettivo di un sistema di SHM è quello di permettere una rilevazione facile ed economica dei danni prima che possano raggiungere livelli critici. Siccome la diffusione di materiali compositi pone problemi di tolleranza al danno e osservabilità del danno, lo SHM si presenta come una delle tecniche più promettenti per lo sviluppo di strutture più leggere, più efficienti ed affidabili. Una delle tecniche più interessanti per l'identificazione dei danni è quella che usa le onde guidate, che possono essere prodotte ed osservate in-situ e per la possibilità di correlare le anomalie nella propagazione con i danni della struttura. La possibilità di modellare queste onde attraverso uno strumento versatile come gli Elementi Finiti (EF) permette di migliorare notevolmente la ricerca nel campo dello SHM, perchè si possono ridurre le analisi sperimentali e quindi i costi di sviluppo di un sistema di SHM. Tuttavia, data la natura complessa di queste onde, soprattutto in laminati compositi, bisogna fornire una validazione dei modelli ad EF. Questo è l'obiettivo della tesi. Per raggiungerlo si sono confrontati i risultati dei modelli ad EF con quelli di un'altra tecnica numerica, sviluppata specificatamente per modellare le onde nelle piastre, nota come Semi-Analytical Finite Element (SAFE). Questo confronto è possibile solo dopo aver applicato una particolare tecnica di elaborazione, che implica l'uso ricorsivo della trasformata di Fourier, agli spostamenti ricavati dai modelli ad EF. Infine questi risultati sono confrontati con quelli ottenuti dall'analisi sperimentale di tre diversi tipi di laminato. Siccome i risultati degli EF, del SAFE e quelli sperimentali sono molto simili tra loro, è stato dimostrato che i modelli ad EF analizzati riproducono correttamente la propagazione delle onde in piastre di materiale composito.

Abstract

The necessity of the aerospace industry to reduce the cost, but to keep good safety standards has brought to the improvement of Structural Health Monitoring (SHM) applications. The objective of a SHM system is to allow an easily an low-cost detection of damages, before critical levels. As the diffusion of composite materials poses relevant problem regarding damage tolerance and damage detectability, SHM is one of the most promising technique for the development of lighter, more efficient and more reliable structures. Guided waves are one of the most interesting instruments for damage identification, basing on in-situ actuation and acquisition and on the possibility to correlate anomalies in wave propagation with internal damage. Modeling this kind of waves with a versatile approach as the Finite Elements (FE) allows great improvements in the SHM field of research, because this approach can reduce the experimental analyses and thus the development costs of a SHM system. Since the complex nature of the guided waves, especially in composite laminates, a validation of these FE models must be provided. This is the objective of this thesis. To accomplish this task the results obtained by the FE models are compared with the ones provided by another numerical technique expressly developed to model waves in plates. Such a technique is known as Semi-Analytical Finite Element (SAFE). This comparison is only possible after a particular post-processing technique, which involve the recursive use of the Fourier transform, of the displacements measured in the FE models. Finally these data are compared with the ones obtained from an experimental analysis of three different type of laminates. Since the results of the FE, of the SAFE and of the experiments are very similar, it is demonstrated that the FE models provided are well-suited to represent wave propagation in composite plates.

Contents

Introduzione	1
Introduction	3
1 Structural Health Monitoring and wave propagation	5
1.1 Brief review of state of art in SHM technique	6
1.2 Theory of waves in solid media	7
1.2.1 Waves in taut string	8
1.2.2 String on an elastic base - Dispersion	11
1.2.3 Group velocity	15
1.2.4 Wave in plates - Lamb waves	18
1.3 Objective of the present work	22
2 FE modeling for wave propagation in isotropic and anisotropic plates	23
2.1 Overview of Abaqus/Explicit	24
2.2 Model of an isotropic plate	25
2.3 Wave propagation in an isotropic plate	34
2.3.1 The aspect ratio behavior	36
2.4 Other application of wave propagation in isotropic plates	37
2.5 Model of an anisotropic plate	41
2.5.1 Wave propagation in quasi-isotropic carbon laminate	45
2.6 Alternative modeling technique	46
2.6.1 Alternative hybrid 2D/3D modeling technique	46
2.6.2 Validation of the alternative modeling technique	56
2.6.3 Motivation for the use of the alternative modeling technique	58
2.7 Wave propagation in anisotropic plates	59
2.7.1 Confrontation of standard and alternative technique	62
2.8 The need for model validation	67

3	Semi-Analytical FE for the dispersion analysis of composite plates	69
3.1	Overview	70
3.2	Cross-sectional discretization	71
3.3	Modeling and shape functions	72
3.4	Solution	76
3.5	Implementation and examples	79
3.6	Validation through spatial Fourier Analysis	87
3.6.1	Fourier transform	89
3.6.2	Two and three dimensional Fourier transform of numerical data	93
3.6.3	Comparison of numerical and Semi-Analytical Finite Elements predictions for isotropic	97
3.6.4	Comparison of numerical and Semi-Analytical Finite Elements predictions for composites	99
4	Experimental analysis	103
4.1	Experimental setup	103
4.2	Experimental results	111
4.3	Comparison with Semi-Analytical Finite Element predictions for composite plates	113
	Conclusions and future works	119
	Conclusioni e sviluppi futuri	123
	Bibliography	130

List of Figures

1.1	Differential element of taut string	8
1.2	Deflections of an infinite long string at successive times	10
1.3	Undistorted propagation of wave envelope	10
1.4	Differential element of a string on an elastic base	11
1.5	Distorted propagation of a wave envelope	13
1.6	Frequency spectrum for a string on an elastic foundation	14
1.7	Two-dimensional representation of the frequency spectrum showing relation between chord slope and phase velocity	14
1.8	Dispersion curve for a string on an elastic foundation	15
1.9	Group velocity example	17
1.10	Group velocity variation with phase velocity	17
1.11	Directions of particle motion for the case of harmonic waves in infinite media	19
1.12	Symmetric and anti-symmetric Lamb wave modes	21
1.13	Phase velocity dispersion curves for an aluminum plate	21
1.14	SH wave mode propagation	22
2.1	Linear brick element with reduced integration and hourglass control (C3D8R)	26
2.2	Group velocity dispersion curves of Lamb waves in Aluminum	28
2.3	The aspect ratio of the element is $AR=a/b$	28
2.4	Pure modes by excitation of the plate on both sides	30
2.5	Input excitation signal in time and frequency domain, 5.5 cycles at 200kHz	31
2.6	Dimensions of the plate and position of the load	33
2.7	Model of the plate	34
2.8	Field output of the out-of-plane displacement U2 for the isotropic plate	35
2.9	Cross-section deformation along the long side of the plate at $20\mu s$	36

2.10	Field output of the out-of-plane displacement U2 for isotropic plate at different aspect ratios	36
2.11	Model of the plate for the scattering analysis	39
2.12	Time histories of the displacements along the radius U_r and the tangent U_θ of the circumference of the transducers and perpendicular to the plate U_z	41
2.13	Analytical results calculate by Grahn for a partial hole half plate deep	42
2.14	Scattering polar plots for a partial hole of 5 mm of diameter, half plate thickness deep and excitation frequency of 316 kHz	42
2.15	Field output of the out-of-plane displacement U2 for Plate1, modeled with the standard technique	47
2.16	Forces and stresses that act on the composite laminate and on the sub-laminate in bending	48
2.17	Scheme of the composite laminate in the alternative modeling technique	50
2.18	Displacements between two adjacent sub-laminates	50
2.19	Detail of a FE scheme for the alternative modeling technique	52
2.20	Cut out view of Plate1 modeled according to alternative technique	53
2.21	Cross-section of the standard and the alternative FE technique to model composites	53
2.22	Free end displacements of the validation model for different refinements levels	56
2.23	Force-displacement curves for the reference and alternative models	57
2.24	Stress component σ_{11} for the reference and alternative models	57
2.25	Stress component σ_{12} for the reference and alternative models	58
2.26	Stress component σ_{22} for the reference and alternative models	58
2.27	Field output of the out-of-plane displacement U2 for Plate1, modeled with the alternative technique	60
2.28	Field output of the out-of-plane displacement U2 for Plate2, modeled with the alternative technique	61
2.29	Field output of the out-of-plane displacement U2 for Plate3, modeled with the alternative technique	62
2.30	Position of the measure point in the plate	63
2.31	Confrontation of the field output of the out-of-plane displacement U2 for Plate1 at $20\mu s$ for the standard and alternative modeling technique	64
2.32	Out-of-plane U2 displacement histories for standard and alternative technique	64

2.33	Integration points for the standard and alternative technique .	65
2.34	σ_{11} stress histories for standard and alternative technique. Lower element	65
2.35	σ_{22} stress histories for standard and alternative technique. Lower element	66
2.36	σ_{12} stress histories for standard and alternative technique. Lower element	66
3.1	SAFE discretization of an infinitely wide plate using mono-dimensional three-node elements. In the triangle there is the ID of the element	72
3.2	Shape function for the quadratic mono-dimensional elements. .	72
3.3	Wavenumber, phase and group velocity dispersion curves of the isotropic, 1mm thick, aluminum plate	81
3.4	Wavenumber and phase velocity dispersion curves of the unidirectional $[0_8^{\circ}]$ fibre glass plate at different angle θ	82
3.5	Wavenumber and phase velocity polar plots of the unidirectional $[0_8^{\circ}]$ fiber glass plate	83
3.6	Group velocity dispersion curves of the unidirectional $[0_8^{\circ}]$ fiber glass plate at different angle θ	84
3.7	Wavenumber, phase and group velocity dispersion curves of the $[0_2^{\circ} 90_2^{\circ}]_s$ fiber glass plate	85
3.8	Wavenumber and phase velocity polar plots of the $[0_2^{\circ} 90_2^{\circ}]_s$ fiber glass plate	86
3.9	Wavenumber, phase and group velocity dispersion curves of the $[0^{\circ} 45^{\circ} 90^{\circ} - 45^{\circ}]_{2s}$ carbon fiber plate	87
3.10	Wavenumber and phase velocity polar plots of the $[0^{\circ} 45^{\circ} 90^{\circ} - 45^{\circ}]_{2s}$ carbon fiber plate	88
3.11	Node at coordinated $x=36$ mm, $z=24$ mm on the top surface .	90
3.12	Displacement history of a node and its frequency content for the FE model of the aluminum plate	90
3.13	Line of nodes along the 0° direction on the top surface of the FE model	91
3.14	Displacement along the 0° line and its wavenumber content for the FE model of the aluminum plate	92
3.15	Frequency-wavenumber plot for FE model of aluminum plate along 0° line	94
3.16	Frequency-wavenumber plots for FE model of aluminum plate along 0° line at different zero-padding expansions	94
3.17	Nodes on the top surface of the FE model	95
3.18	Organization of the data in the three dimensional structure . .	95

3.19	Distribution of the Fourier coefficients in the resulting 3D structure	96
3.20	Bi-dimensional wavenumber plots at a given frequency for FE model of aluminum plate at different zero-padding expansions	97
3.21	Frequency-wavenumber along 0° line and bi-dimensional wavenumber plot for the FE model of aluminum plate	98
3.22	Frequency-wavenumber along 0° line and bi-dimensional wavenumber plot for the FE model (alternative technique) of Plate1	99
3.23	Frequency-wavenumber along 0° line and bi-dimensional wavenumber plot for the FE model (alternative technique) of Plate2	100
3.24	Frequency-wavenumber along 0° line and bi-dimensional wavenumber plot for the FE model (alternative technique) of Plate3	101
4.1	Experimental setup	104
4.2	Schematic representation of the Laser Doppler Vibrometer	105
4.3	Plate2 prepared for the experimental analysis	107
4.4	Plate clamped and positioned perpendicular to the laser beam	108
4.5	Function generator Agilent 33220A	108
4.6	Vibrometer controller and data management system	109
4.7	Representation of the scanned area of the plate	109
4.8	Frequency-wavenumber along 0° line and bi-dimensional wavenumber plot for experimental data of Plate1	111
4.9	Top view of the plate rotated to catch the in-plane wave SH_0	112
4.10	Frequency-wavenumber along 0° line and bi-dimensional wavenumber plot for experimental data of Plate1 14° tilted	113
4.11	Frequency-wavenumber plot for experimental Plate1, 14° tilted along 0° line	114
4.12	Bi-dimensional wavenumber plot for experimental Plate1, 14° tilted	114
4.13	Frequency-wavenumber plot for experimental Plate2, 14° tilted along 0° line	115
4.14	Frequency-wavenumber plot for experimental Plate2, 14° tilted along 90° line	116
4.15	Bi-dimensional wavenumber plot for experimental Plate2, 14° tilted	116
4.16	Frequency-wavenumber plot for experimental Plate3, 14° tilted along 90° line	117
4.17	Bi-dimensional wavenumber plot for experimental Plate3, 14° tilted	118

List of Tables

2.1	Displacements along the axes of the model	25
2.2	Properties of aluminum adopted for the isotropic model	27
2.3	Dimensions of the element in the isotropic model	29
2.4	Time step and observation time	30
2.5	Characteristics of the input signal	31
2.6	Characteristics of the output file	32
2.7	Dimensions of the plate	33
2.8	Dimension of the FE problem and computational time for the isotropic plate	34
2.9	Characteristics of the model for the scattering analysis	38
2.10	Values of computational time and damping ratios for different damping coefficients	39
2.11	Characteristics of the FE model for the scattering analysis	40
2.12	Position and number of the transducers and observation time	41
2.13	Characteristics of the carbon fiber lamina	43
2.14	Characteristics of the glass fiber lamina	43
2.15	Summary of the anisotropic plates analyzed in this work	44
2.16	Common characteristics of the anisotropic plates	45
2.17	Specific characteristics of the anisotropic plates	46
2.18	Material characteristics for each type of element in the alternative modeling technique	54
2.19	Densities adopted for the alternative modeling technique	55
2.20	Dimensions of the bi-dimensional element in the alternative modeling technique	55
2.21	Dimensions of the FE problem and computational times for the plates modeled with the alternative technique	55
4.1	Summary of the anisotropic plates analyzed in this work	106
4.2	Characteristics of the piezoelectric disk actuator	107
4.3	Resume of the specification of the experimental system	110

Introduzione

Le sempre più stringenti esigenze di riduzione dei costi a cui è sottoposta l'industria aerospaziale hanno portato all'utilizzo sempre più diffuso di materiali compositi. Questi materiali, dotati di elevati rapporti resistenza-peso e rigidità peso, consentono di realizzare strutture sempre più leggere ed efficienti, in grado di aumentare il carico pagante e ridurre i consumi. Tuttavia le strutture in materiale composito sono molto vulnerabili ai danni, soprattutto alla delaminazione che può essere introdotta sia in fase di realizzazione, sia durante la vita operativa. La presenza di delaminazione può portare, se trascurata, anche al cedimento catastrofico di un'intera struttura

La sicurezza non può mai passare in secondo piano rispetto alla riduzione dei costi. Per questo motivo negli ultimi anni la ricerca si sta impegnando nella realizzazione di sistemi di monitoraggio del danno sempre più sofisticati, in grado di dare valutazioni in tempo reale dello stato di integrità strutturale. Questo filone di ricerca è noto con il termine di Structural Health Monitoring (SHM), letteralmente monitoraggio della salute strutturale.

La ricerca condotta in questa tesi si inserisce in questo ambito. La possibilità di utilizzare una tecnologia flessibile come quella fornita dagli Elementi Finiti (EF) per la modellazione di un potente strumento di identificazione del danno, come quello fornito dalle onde guidate, ha ispirato questo lavoro. La creazione di modelli numerici in grado di predire la corretta propagazione delle onde permetterebbe di implementare sistemi di SHM in grado di monitorare l'eventuale presenza di danno nelle strutture oltre alla sua posizione e dimensione.

Data la complessità dell'argomento trattato si è scelto di indirizzare la ricerca su un semplice elemento strutturale, quale la piastra. L'obiettivo principale di questo lavoro è quello di verificare che la propagazione ondo-sa ottenuta nei modelli ad EF rispecchi il reale andamento delle onde, che sono governate da leggi molto complesse, soprattutto nei materiali compositi. Questa verifica viene condotta anche per piastre modellate utilizzando una particolare tecnica sviluppata al Politecnico di Milano ed utilizzata per studiare la propagazione del danno nei materiali compositi. Questa scelta è

stata fatta in previsione di un possibile sviluppo futuro in cui lo stesso modello numerico danneggiato possa essere ulteriormente analizzato per la progettazione di un sistema di SHM. Per la realizzazione di questi obiettivi si rende necessaria l'implementazione di un altro strumento di analisi numerica noto come tecnica degli elementi finiti semi-analitici, in inglese Semi-Analytical Finite Element (SAFE). I risultati ottenuti dall'analisi ad EF devono quindi essere confrontati con quelli forniti dall'approccio SAFE. Per questo motivo si rende necessario lo sviluppo di una particolare tecnica di elaborazione dei dati che consenta di ottenere dei risultati confrontabili. Infine i dati numerici, provenienti sia dall'analisi ad EF che da quella SAFE, devono venire confrontati con i risultati misurati sperimentalmente.

Il percorso seguito da questa tesi per raggiungere questi obiettivi si sviluppa in quattro capitoli. Il primo capitolo definisce in maggior dettaglio lo SHM, riporta lo stato dell'arte a riguardo e fornisce una breve introduzione sulla teoria delle onde nei materiali solidi.

Nel secondo capitolo viene descritta la tecnica di modellazione e il modello ad EF sia per la piastra in materiale isotropo, sia per quella in materiale composito. Viene descritta poi la tecnica particolare, sviluppata al Politecnico, per la modellazione dei compositi e vengono quindi riportati i risultati ottenuti.

Il terzo capitolo sviluppa la tecnica chiamata SAFE, viene descritta la procedura e vengono riportati i risultati ottenuti. Viene poi sviluppato il metodo di elaborazione dei dati che consente di confrontare i risultati forniti dagli EF con quelli calcolati per mezzo dell'approccio SAFE. Infine vengono riportati i risultati del confronto.

Il quarto capitolo è centrato sull'analisi sperimentale eseguita presso il Georgia Institute of Technology di Atlanta. Viene spiegata la procedura sperimentale e vengono forniti i risultati ottenuti. Quindi viene riportato il confronto tra i dati sperimentali e quelli forniti dal SAFE.

Introduction

Aerospace industry is characterized by continuously growing cost safe requirements. This fact leads to the exponential increase in the use of composite materials. With such feature as high strength-to-weight and stiffness-to-weight ratios, these materials allow the manufacturing of lighter and more efficient structure, with respect to aluminum alloys, in order to increase the payload and to reduce the fuel consumption. However composite structures are very vulnerable to structural damage, in particular the delamination that can be introduced during manufacturing or service. The occurrence of delamination could potentially leads to a catastrophic failure of the whole structure if it accumulates above a critical level.

Cost saving must never be considered without safety. For this reason in the last years researchers are developing ever more sophisticated damage monitoring systems, which are able to evaluate the health of a structure in real-time. This branch of research is known as Structural Health monitoring (SHM).

The present thesis is inserted in this field of research. The motivation that inspired this work lies in the possibility to utilize a flexible instrument, such as the Finite Elements (FE), to model a powerful damage identification tool, such as the guided waves. A numerical model that can predict the exact propagation of waves in material, could lead to the implementation of SHM systems able to monitor the presence of defects in the structure, their positions and dimensions.

Because of the complexity of this argument, it is chosen to focus the attention on a simple structural element, such as the plate. The main objective of this work is to verify the correctness of the wave propagation modeled with the FE. This is not a trivial task because of the complex nature of wave propagation in plates, especially for the composite materials case. This verification is done also for a FE plate modeled using a particular technique developed at Politecnico di Milano and utilized to predict the damage propagation in composite materials. This choice is done according to an eventual future development, in which the same damaged numerical model could be

further analyzed for a SHM system design. To pursue this objectives another instrument of numerical analysis must be developed. This instrument is the technique known as Semi-Analytical Finite Element (SAFE). The results coming from the the FE analyses must be compared with the results given by the SAFE approach. For this reason a special post-processing technique must be developed in order to produce comparable results. Finally the numerical data, from FE and SAFE, must be compared with the results experimentally measured.

The approach followed in this thesis is divided into for chapter. The first one presents a description of the SHM, along with the state of the art on this technique. Moreover a brief introduction to the theory of waves in solid materials is provided.

In the second chapter the modeling technique of the FE models adopted is extensively described, for both the isotropic and the composite material case. Then the description of the particular technique, developed at Politecnico, for the modeling of composite materials is provided, along with the obtained results.

The third chapter develops the technique known as SAFE, a description of the procedure is provided and the obtained results are reported. Then it is developed the post-processing technique that allows the confrontation of the data, coming from the FE, with the results calculated with the SAFE approach. Finally this confrontation is reported.

The fourth chapter is centered on the experimental analysis carried out at the Georgia Institute of Technology of Atlanta. An explanation of the experimental setup is provided along with the obtained results. Then the confrontation between experimental data and SAFE approach is reported.

Chapter 1

Structural Health Monitoring and wave propagation

The process of implementing a damage identification strategy for aerospace, civil and mechanical engineering infrastructure is referred to as Structural Health Monitoring (SHM). This process involves the observation of a structure or mechanical system over time using periodically spaced measurements, the extraction of damage-sensitive features from these measurements and a statistical analysis of these features to determine the current state of system health. This process can be repeated periodically, to monitor the aging of the structure and damage accumulation, or, in case of an extreme event, it can be used for a rapid condition screening. This possibility shows the benefits that SHM can bring to safety, by monitoring the presence of damages and to operative costs, by reducing maintenance. Moreover SHM may allow to reduce the safety margin of structure, because any damage can be identified at its creation, allowing an immediate planning of maintenance. For all these reason, in the last decade, the interest in SHM is growing further.

The damage identification may be performed by different techniques such as ultrasonic testing, radiographic testing, electromagnetic testing, etc. In SHM applications a damage identification technique must satisfy requirements of implementability, reliability, speed and cost. One of the most promising technique, which satisfy all these requirements, is the one based on the guided waves. This technique consists in exciting the structure in order to generate waves in the material. Then, through the measurements of these waves, by means of a series of transducers, it is expected to identify the presence of damage, its dimension and its position. The correct modeling of waves in structure has a fundamental importance for the definition of a damage identification strategy based on guided waves. For this reason the present work is focused on the possibility to correctly model the wave

propagation in composite plate through the use of the finite element method. Since the argument of waves is widely discussed in this work, it is necessary to present an introduction to wave theory, dealing with the main aspects that will be treated. This introduction is presented in the second sections of the chapter, whereas a review on the state of the art of SHM techniques is reported in the first section.

1.1 Brief review of state of art in SHM technique

The past 10 years have seen a rapid increase in the amount of research related to SHM, as quantified by the significant escalation of papers published on this subject [1]. Another indicator of the increased interest in this technology is the constantly growing number of international conferences that focus directly on SHM. In this sections the state of art of this technology is briefly summarized.

Since SHM may involve different domain of research, especially for the damage identification phase, such as wave propagation, heat-transfer, x-rays, the interest must be focused on one particular technique. Guided waves are one of the most encouraging tool for SHM applications. In plates these waves can propagate for large distances, they are sensible even to small defect and they involve the whole material thickness, meaning that a defect can be identified also if it is in the middle of the plate. One distinction that can be done on papers dealing with SHM by means of Lamb waves, lies in the selection of the mode used for the investigation. The chosen mode should be able to offer a very low dispersion, low attenuation with the distance, high sensitivity to damages, easy excitability and good detectability. Some authors [2] consider the S_0 mode as the proper one, for its low dispersion, low attenuation in amplitude and its velocity of propagation. Other authors [3,4] prefer the A_0 mode, because, even if it is more dispersive for low frequencies, it has lower wavelength than the S_0 mode, thus it can detect smaller defects.

Since the use of composite materials is increasing in many industrial fields, in particular in the aerospace sector, the interest of Lamb waves based SHM is focusing on these materials, which have a much more complex behavior with respect to the homogeneous materials. Moreover composite structures are more vulnerable to structural damage, in particular the delamination that can be introduced even during manufacturing. A review on the state of art of SHM using guided waves in composite plates is given in reference [5]. In this article every step in the SHM process are reviewed, such as the excitation of

the specimen, the techniques adopted to model the propagation of the Lamb waves, the processing of the signal and the algorithms used for the damage identification.

The present work is focused is the possibility to model wave propagation in composite plates by means of Finite Elements (FE) method. The first papers, in which this application of FE is presented, use very simple bi-dimensional models, of simple structure, such as beams [6], made of homogeneous materials. With the increasing computational power available, the complexity of the model is increasing too, from bi-dimensional to three-dimensional. These days it is possible to study the wave propagation even in large structures. These structures can be simple plates [7] or more complex structures as stiffened plates [8] made in isotropic or composite materials. Another interesting aspect that is modeled through the FE method is the real behavior of a piezoelectric actuator on a composite plate [9]. In this article a simple summary of the characteristics that a FE model should have to correctly represent the waves it is presented, even though nothing is said about some important aspects as the aspect ratio of the solids elements.

The state of art in FE modeling, is the investigation of the scattered waves that originate when Lamb waves hit a defect. To model the defect different technique are available, in isotropic material it is possible to remove the elements simulating a crack in the material [10] or a through-thickness hole [11], while in composite materials it is possible to reduce the elastic properties of the elements forming the damage [12]. The objective of all these investigations is to define a standard that allows the modeling of any structure, of any material, in order to identify the behavior of the guided waves and their reaction to the presence of a damage. With such a standard it should be possible to predict what answer should be expected from sensors in the case of damage in one particular region of the structure. The availability of such a numerical instrument could significantly reduce the experimental analyses and thus the costs. Moreover it could lead to the implementation of an efficient SHM system that could improve the safety and reduce the operative costs of structures.

1.2 Theory of waves in solid media

In this section a brief description of the main aspects of the wave theory in solid media is presented. The approach adopted by the authors of two reference book [13,14] is followed. Waves in a taut string are first investigated because they require a simple mathematical approach and because nearly all the basic concepts of propagation, such as dispersion and group velocity,

are introduced. Then the waves in plate, such as the Lamb waves, will be investigated.

1.2.1 Waves in taut string

The governing equation for a taut string is now developed. Since boundaries introduce complication an infinite length string is considered. The differential string element under tension F of Fig.1.1 is considered. It is assumed

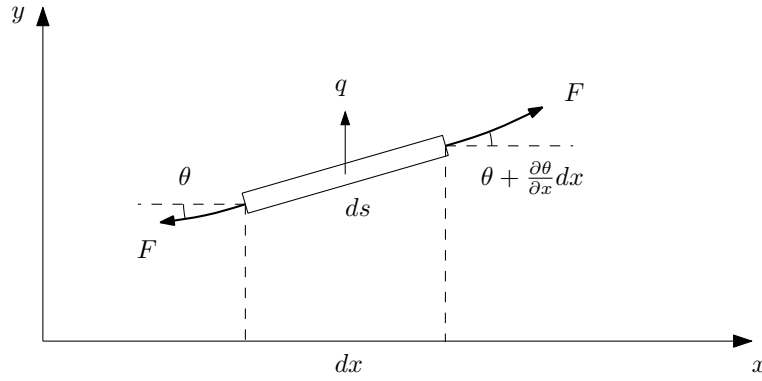


Figure 1.1: Differential element of taut string

that any variation in the tension due to string displacement is negligible. The mass density per unit length is ρ and the external loading is $q(x, t)$. The equation of motion in the vertical direction y is Eq.1.1.

$$-F \sin \theta + F \sin \left(\theta + \frac{\partial \theta}{\partial x} dx \right) + q ds = \rho ds \frac{\partial^2 y}{\partial t^2} \quad (1.1)$$

The arc length ds is given by $\sqrt{1 + y'^2} dx$. If small deflection are assumed $ds \approx dx$, $\sin \theta \approx \theta$ and $\theta \approx \partial y / \partial x$, the preceding equation becomes Eq.1.2.

$$F \frac{\partial^2 y}{\partial x^2} + q = \rho \frac{\partial^2 y}{\partial t^2} \quad (1.2)$$

Of particular interest is the form of the homogeneous equation obtained by setting $q = 0$, giving Eq.1.3.

$$\frac{\partial^2 y}{\partial x^2} = \frac{1}{c_0^2} \frac{\partial^2 y}{\partial t^2} \quad c_0 = \sqrt{\frac{F}{\rho}} \quad (1.3)$$

This equation is known as the wave equation and the term c_0 denotes the velocity of wave propagation.

Now, using the separation of variable approach, the propagation of a simple harmonic wave is investigated. The term $y = Y(x)T(t)$ is substituted in Eq.1.3 giving Eq.1.4.

$$\frac{Y''}{Y} = \frac{T''}{c_0^2 T} = -k^2 \quad (1.4)$$

The resulting solution for $y(x, t)$ is expressed in Eq.1.5

$$y = (A_1 \sin kx + A_2 \cos kx)(A_3 \sin \omega t + A_4 \cos \omega t) \quad (1.5)$$

where the radial frequency is given as $\omega = kc_0$. Regrouping and multiplying Eq.1.6 is obtained.

$$y = A_1 A_4 \sin kx \cos \omega t + A_2 A_3 \cos kx \sin \omega t + A_2 A_4 \cos kx \cos \omega t + A_1 A_3 \sin kx \sin \omega t \quad (1.6)$$

Using trigonometric identities as $\sin(\alpha + \beta) = \sin \alpha \cos \beta + \cos \alpha \sin \beta$ the solution can be put in the form of Eq.1.7.

$$y = B_1 \sin(kx + \omega t) + B_2 \sin(kx - \omega t) + B_3 \cos(kx + \omega t) + B_4 \cos(kx - \omega t) \quad (1.7)$$

Any of the four terms of this equation, as the one in Eq.1.8.

$$y = A \cos(kx - \omega t) = A \cos k(x - c_0 t) \quad (1.8)$$

Each term can show the wave propagation in the direction of positive x. Considering the argument of Eq.1.8 as the phase, which is defined in Eq.1.9, the wave can be visualized as in Fig.1.2.

$$\phi = kx - \omega t = k(x - c_0 t) \quad (1.9)$$

It can be noted that for increasing time, increasing values of x are required to maintain the phase constant. The shape of the deflections at successive instants of time should be represented as in Fig.1.2. The propagation velocity of the constant phase is c_0 and it is defined as phase velocity. Constancy of phase for increasing time requires $x = c_0 t$. Referring to Fig.1.2, the distance between two successive points of constant phase is called wavelength and indicated by the symbol λ . The wavelength is related to the parameter k by Eq.1.10.

$$k = \frac{2\pi}{\lambda} \quad (1.10)$$

The parameter k is called wavenumber. It is inversely proportional to the wavelength and it represents the number of waves in the unit length. Having considered the characteristics of a typical harmonic wave, it is seen that the

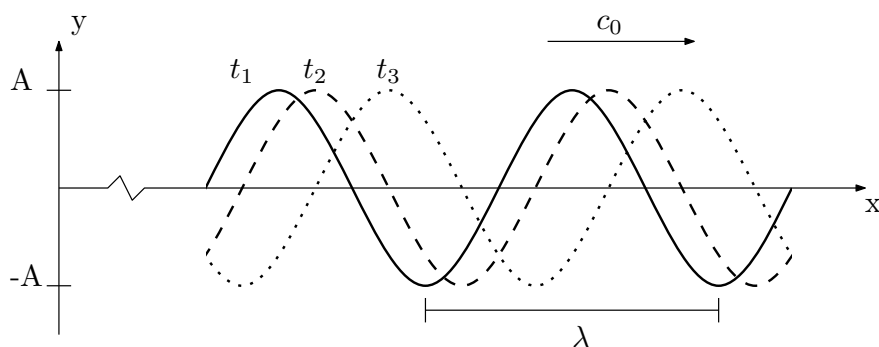


Figure 1.2: Deflections of an infinite long string at successive times

remaining terms of Eq.1.7 are similar in nature. The major point of difference is that terms having the argument $(kx + \omega t)$ are propagating in the negative x direction.

Another solution to the wave equation is given by D'Alembert and it is reported in Eq.1.11.

$$y(x, t) = f(x - c_0 t) + g(x + c_0 t) \quad (1.11)$$

This equation satisfies Eq.1.3 for any arbitrary function f and g , as long as the initial and boundary conditions can eventually be satisfied. The functions f and g represent propagating disturbance. Whatever the initial shape of the disturbances, that shape is maintained during the propagation, so the waves propagate without distortion, as represented in Fig.1.3. The undistorted

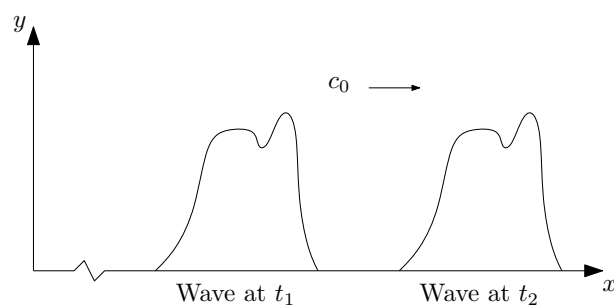


Figure 1.3: Undistorted propagation of wave envelope

nature of wave propagation represents a fundamental characteristics of the one-dimensional wave equation.

1.2.2 String on an elastic base - Dispersion

The wave equation Eq.1.3 considered up to this point is simple. Moreover, in the system described by this equation, the pulses propagate without distortions. Now a more complicated situation, in which the string rests on an elastic foundation, is considered. This situation is represented in Fig.1.4. The external load may be interpreted as due to the elastic foundation, as

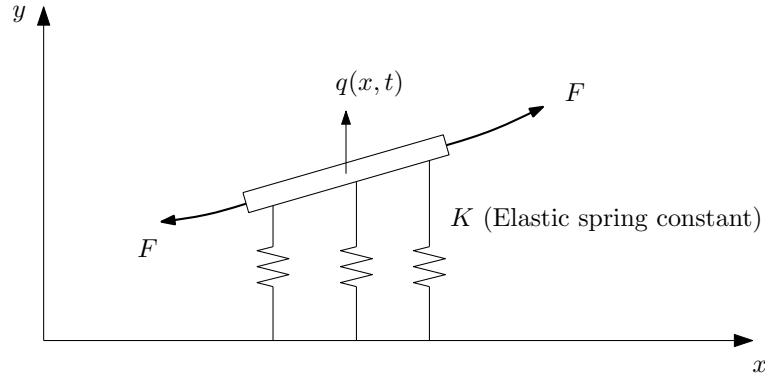


Figure 1.4: Differential element of a string on an elastic base

expressed by Eq.1.12

$$q(x, t) = -Ky(x, t) \quad (1.12)$$

where K is the elastic modulus of the foundation. The resulting governing equation, in the absence of other external forces, is given by Eq.1.13.

$$\frac{\partial^2 y}{\partial x^2} - \frac{K}{F}y = \frac{1}{c_0^2} \frac{\partial^2 y}{\partial t^2} \quad c_0 = \sqrt{\frac{F}{\rho}} \quad (1.13)$$

This equation is no longer of simple wave equation form. Thus a solution of the form $f(x \pm c_0 t)$ may not satisfy it. Since the major characteristic of such a solution is undistorted wave pulse propagation, it is now logical to expect some type of distortion. This phenomenon is known as dispersion.

Now the necessary conditions for the propagation of harmonic waves are determined. Assuming the solution Eq.1.14

$$y(x, t) = Ae^{i(kx - \omega t)} \quad (1.14)$$

and substituting in Eq.1.13, it gives the expression Eq.1.15, which is called characteristic equation or dispersion equation.

$$\left(-k^2 - \frac{K}{F} + \frac{\omega^2}{c_0^2}\right) e^{i(kx - \omega t)} = 0 \quad (1.15)$$

This equation must fulfill Eq.1.16 in order to admit non-trivial solutions

$$\omega^2 = c_0^2 \left(k^2 + \frac{K}{F} \right) \quad \omega = \omega(k) \quad (1.16)$$

or, alternatively, Eq.1.17.

$$k^2 = \frac{\omega^2}{c_0^2} - \frac{K}{F} \quad k = k(\omega) \quad (1.17)$$

Here the phase velocity c_p is different from the c_0 of the taut string. Indeed, substituting $\omega = kc_p$ in Eq.1.16 or Eq.1.17, the result of Eq.1.18 is obtained.

$$c_p^2 = c_0^2 \left(1 + \frac{K}{Fk^2} \right) \quad c_p = c_p(k) \quad (1.18)$$

Alternatively, one can obtain the results in Eq.1.19.

$$k^2 = \frac{K/F}{(c_p^2/c_0^2) - 1} \quad k = k(c_p) \quad (1.19)$$

Another set of relations can be obtained by eliminating k from Eq.1.17 or ω from Eq.1.19, to give Eq.1.20

$$\omega^2 = \frac{KFc_p^2}{(c_p^2/c_0^2) - 1} \quad \omega = \omega(c_p) \quad (1.20)$$

and Eq.1.21.

$$k^2 = \frac{\omega^2 c_0^2}{\omega^2 - (kc_0^2/F)} \quad k = k(\omega) \quad (1.21)$$

The results show that an harmonic wave of frequency ω can propagate only at a specific velocity c_p as it is indicated by the relation $\omega = \omega(c_p)$. Considering a pulse shape at a given time $t = t_0$ as a Fourier superposition of harmonic waves, as the time advances, each Fourier component of the original pulse will propagate with its own individual velocity. The various components will become increasingly out-of-phase relative to their original position so that the original pulse shape will become increasingly distorted, as shown in Fig.1.5. In the taut string, where $K = 0$, this phenomenon is not present.

Another important result comes from the analysis of the roots of Eq.1.17

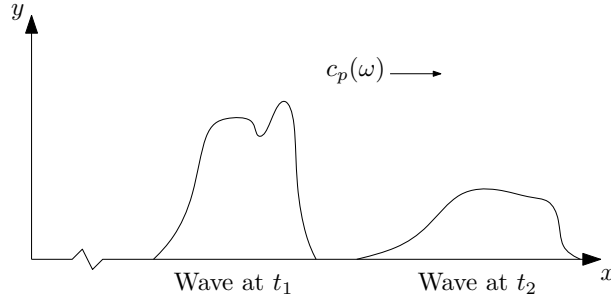


Figure 1.5: Distorted propagation of a wave envelope

which are reported in Eq.1.22.

$$k = \pm \sqrt{\frac{\omega^2}{c_0^2} - \frac{K}{F}} \quad (1.22)$$

The roots are real if $\omega^2/c_0^2 > K/F$, thus the propagation is possible to the right or left, depending on which sign is selected, as expressed by Eq.1.23.

$$y = Ae^{-i(\pm kx + \omega t)} \quad (1.23)$$

On the other hand, if $\omega^2/c_0^2 < K/F$ then the wavenumber k is imaginary. Defining $\bar{k}^2 = -k^2$ the motion of the string is given by Eq.1.24.

$$y = Ae^{\pm \bar{k}x} e^{-i\omega t} \quad (1.24)$$

This corresponds to a spatially varying but non-propagating disturbance. Since the interest is on the conditions under which an harmonic wave can exist, the results for imaginary wavenumbers are not considered in the study of propagating waves, since they are non-propagating. Finally, the case $\omega^2/c_0^2 = K/F$ represents the transition from propagation to non-propagation. Defining $\omega_c = c_0\sqrt{K/F}$, the string motion is the one reported in Eq.1.25.

$$y = Ae^{-i\omega_c t} \quad (1.25)$$

The frequency ω_c is called cutoff frequency of the propagating mode. There is no spatial variation in the motion, so the string is vibrating as a simple spring-mass system.

The basic factors governing propagation in a string on an elastic foundation have been presented. Now these results are displayed in graphical form. Typically two types of displays are used: the plot of frequency versus wavenumber which is called frequency spectrum of the system and the plot

of phase velocity versus wavenumber, which is called dispersion curve of the system. To plot the frequency spectrum the Eq.1.22 should be considered. Assuming the frequency as real and positive, it is possible to get both real and imaginary wavenumbers if $\omega < \omega_c$ and $\omega > \omega_c$ respectively. The results are shown in Fig.1.6. The curves on the real plane are hyperbolas, while the

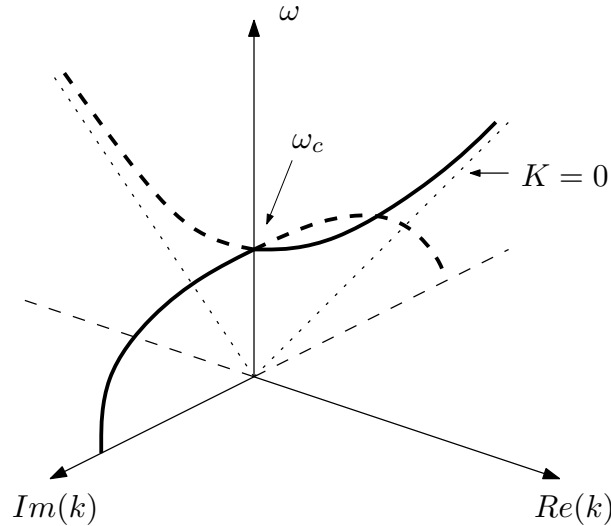


Figure 1.6: Frequency spectrum for a string on an elastic foundation

imaginary curves are ellipses. The line $K = 0$ is the non-dispersive result for the taut string. It is possible to extract the phase velocity from the frequency spectrum by the relation $\omega = c_p k$. Graphically, taking a point on the real curve of the spectrum, the slope of the chord between the point and the origin is the phase velocity $c_p = \omega/k$. This relation is shown in Fig.1.7. In this fig-

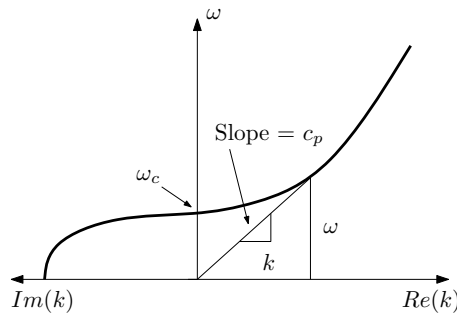


Figure 1.7: Two-dimensional representation of the frequency spectrum showing relation between chord slope and phase velocity

ure it is also shown an alternative way to represent the frequency spectrum.

Since the spectrum is usually symmetric with respect the $Re(k) = 0$ and the $Im(k) = 0$ planes, it is sufficient to present a two-dimensional plot of the ω on the $Re(k) > 0$ and $Im(k) > 0$ axes. Phase velocity is often presented independently by dispersion curves. Although it is possible to consider c_p as positive, negative, real and imaginary, depending on k , the most physical meaningful information is contained in a plot which has as axes $Re(c_p) > 0$ and $Re(k) > 0$, as shown in Fig.1.8. The horizontal line is the result of the

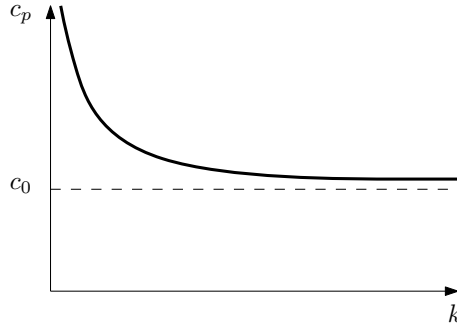


Figure 1.8: Dispersion curve for a string on an elastic foundation

non-dispersive string, where all the wavelength propagate at the same velocities c_0 . Usually in structural health monitoring applications the dispersion curves present the phase velocity as function of frequency ω .

1.2.3 Group velocity

Group velocity is associated with the propagation velocity of a group of waves of similar frequency. In reference books this concept is always introduced by means of the pool example. A stone dropped in a pool of still water creates an intense local disturbance which does not remain localized, but spread outward over the pool as a train of ripples. In this phenomenon can be observed that, when a group of waves advance into still water, the velocity of the group is less than the velocity of individual waves of which it is composed. The waves appear to originate at the rear of the group, propagate to the front and disappear.

A simple analytical explanation is to consider two propagating harmonic waves of equal amplitude, but slightly different frequency, ω_1 and ω_2 . Such harmonic wave will have the expression of Eq.1.26,

$$y = A \cos(k_1x - \omega_1t) + A \cos(k_2x - \omega_2t) \quad (1.26)$$

where $\omega_1 = k_1c_{p1}$ and $\omega_2 = k_2c_{p2}$. Using trigonometric identities this expres-

sion can be written as Eq.1.27.

$$y = 2A \cos \left[\frac{1}{2}(k_2 - k_1)x - \frac{1}{2}(\omega_2 - \omega_1)t \right] \cos \left[\frac{1}{2}(k_1 + k_2)x - (\omega_1 + \omega_2)t \right] \quad (1.27)$$

Since the frequencies are only slightly different, the wavenumber $k = \omega/c_p$ also will slightly differ, as expressed in Eq.1.28.

$$\omega_2 - \omega_1 = \Delta\omega \quad k_2 - k_1 = \Delta k \quad (1.28)$$

Similarly the average frequency, wavenumber and velocity are defined in Eq.1.29.

$$\omega = \frac{1}{2}(\omega_1 + \omega_2) \quad k = \frac{1}{2}(k_1 + k_2) \quad c_p = \frac{\omega}{k} \quad (1.29)$$

Thus Eq.1.27 can be written as Eq.1.30.

$$y = 2A \underbrace{\cos \left[\frac{1}{2}\Delta kx - \frac{1}{2}\Delta\omega t \right]}_{\text{Low-frequency term}} \cdot \underbrace{\cos [kx - \omega t]}_{\text{High-frequency term}} \quad (1.30)$$

In this equation the cosine term containing the difference terms Δk and $\Delta\omega$ is a low-frequency term, since $\Delta\omega$ is a small number. The propagation velocity of the low-frequency term is expressed in Eq.1.31,

$$c_g = \frac{\Delta\omega}{\Delta k} \quad (1.31)$$

which in the limit becomes Eq.1.32.

$$c_g = \frac{\partial\omega}{\partial k} \quad (1.32)$$

This velocity is called group velocity. On the other hand the cosine term containing the average wavenumber k and frequency ω will be an high-frequency term, propagating at the average velocity c_p . The low-frequency term acts as a modulation on the high-frequency carrier as shown in Fig.1.9. The individual harmonics travel with different phase velocities c_p , but the superimposed packet travels with the group velocity c_g . The velocity of the high-frequency carrier may actually be greater than, equal to, or less than the velocity c_g . The actual relation will depend on the dispersion characteristics of the elastic system. Graphically the various cases can be represented considering Eq.1.32, which states that the group velocity is equal to the local slope of

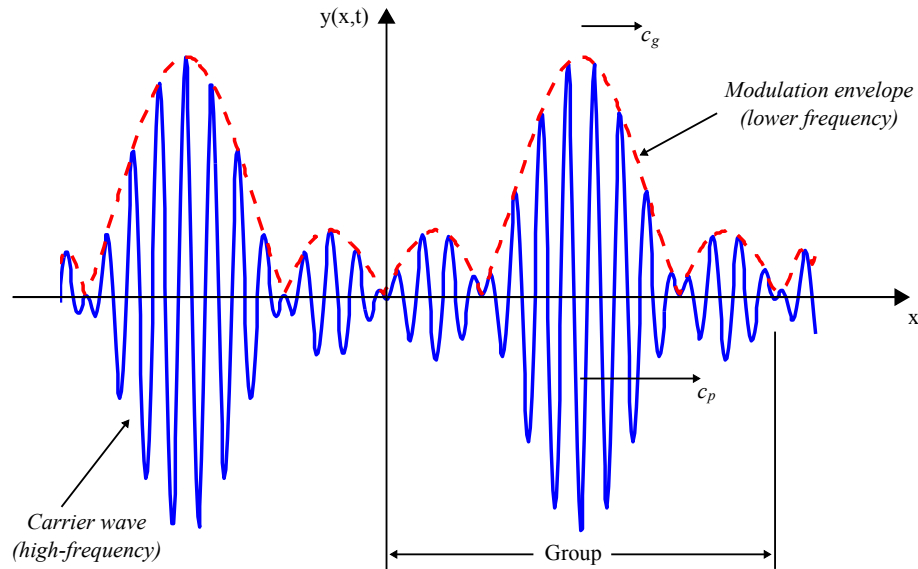


Figure 1.9: Group velocity example

the frequency spectrum curve, as shown in Fig.1.10. Recalling that the slope

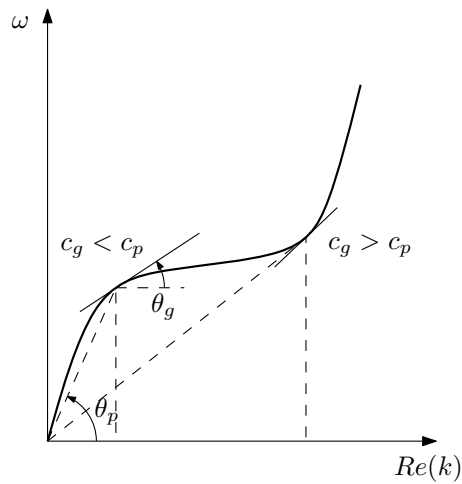


Figure 1.10: Group velocity variation with phase velocity

of a chord to a point is the phase velocity, if that slope is higher than the local slope of the curve ($\theta_p > \theta_g$), then $c_g < c_p$, otherwise if the slope of the chord to a point is lower than the local slope of the curve ($\theta_p < \theta_g$), then $c_g > c_p$.

1.2.4 Wave in plates - Lamb waves

Now a more practical aspect of the wave propagation is presented. First it is necessary to distinguish between bulk waves and guided waves. They are both governed by the same set of partial differential wave equations (reported in [13, 14]), but they differ in the boundary conditions. Bulk waves travel in the bulk of the material, hence away from the boundaries, for this reason mathematically there are no boundary conditions that need to be satisfied by the proposed solution. In contrast, the solution to a guided wave problem must satisfy the governing equation as well as some physical boundary conditions. The introduction of boundary conditions makes the guided waves problem difficult to solve analytically. However some special cases of guided waves problems have been solved and these solutions take the names of the investigator. The Rayleigh waves are free waves on the surface of a semi-infinite solid. Stonely waves are free waves that occur at an interface between two media. Lamb waves are waves of plain strain that occur in a free plate.

Another difference between bulk waves and guided waves is that bulk waves have just two mode of propagation that are the longitudinal mode and the transverse mode, whereas the guided waves have an infinite number of modes. Longitudinal waves, also called volumetric wave, imply no rotations of medium particles, whereas transverse waves, also called rotational waves, do not imply volume change in material. These waves propagate in infinite media at two different speeds, which are c_L for the longitudinal mode and c_T for the transverse mode. The expressions of these velocities are reported in Eq.1.33,

$$c_L = \sqrt{\frac{E(1-\nu)}{\rho(1+\nu)(1-2\nu)}} \quad (1.33a)$$

$$c_t = \sqrt{\frac{E}{2\rho(1+\nu)}} \quad (1.33b)$$

where E is the Young's modulus, ν is the Poisson's ratio and ρ is the density of the material. A graphical representation of the particle motion for the longitudinal and transverse mode is shown in Fig.1.11. The interactions of these two basic modes with the boundaries generate reflections, refractions and mode conversions [13, 14]. The superpositions of all these waves cause the formation of guided wave modes in the plate, which are infinite. The interest in the present work is focused on plates. Thus guided wave in plates are now analyzed, these waves are also known as Lamb waves.

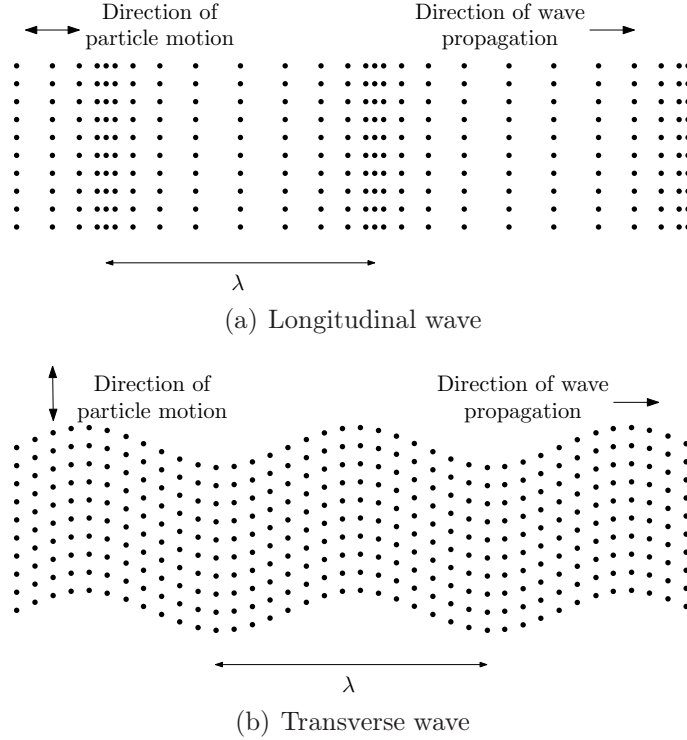


Figure 1.11: Directions of particle motion for the case of harmonic waves in infinite media

Lamb waves, like other elastic waves, can be described in a form of cartesian tensor notation, as expressed in Eq.1.34,

$$\mu u_{i/jj} + (\lambda + \mu) u_{j/ji} + \rho f_i = \rho \ddot{u}_i \quad (1.34)$$

where $i, j = 1, 2, 3$, u_i and f_i are the deformation and the body force in the i direction, respectively. These equations of motions, which contain only the particle displacements, are the governing partial differential equations for displacement. They are defined through the use of Lamé constants λ and μ , which can be expressed in terms of Young's modulus and Poisson's ratio through the relations reported in Eq.1.35.

$$E = \frac{\mu(3\lambda + 2\mu)}{\lambda + \mu} \quad (1.35a)$$

$$\nu = \frac{\lambda}{2(\lambda + \mu)} \quad (1.35b)$$

To well-define the problem of Lamb waves in plates, boundary conditions must be applied at both free surfaces of the plate. On these surfaces the traction must vanish. Moreover, the assumption of plain stress must be done. Under these conditions it is possible to find a solution to Eq.1.34, which describe Lamb waves in an homogeneous plate. To solve this problem the method of the displacements potentials can be used [15]. The solution can be split into two parts with symmetric and anti-symmetric properties. Each part leads to a different Lamb wave mode, one symmetric and one anti-symmetric, as expressed in Eq.1.36,

$$\frac{\tan(qh)}{\tan(ph)} = -\frac{4k^2qp}{(k^2 - q^2)^2} \quad \text{for symmetric modes} \quad (1.36a)$$

$$\frac{\tan(qh)}{\tan(ph)} = -\frac{(k^2 - q^2)^2}{4k^2qp} \quad \text{for anti - symmetric modes} \quad (1.36b)$$

where p and q are defined in Eq.1.37,

$$p^2 = \frac{\omega^2}{c_L^2} - k^2 \quad (1.37a)$$

$$q^2 = \frac{\omega^2}{c_T^2} - k^2 \quad (1.37b)$$

and h , k and ω are the half-thickness of the plate, wavenumber and frequency respectively. The graphical representation of the symmetric and the anti-symmetric modes is shown in Fig.1.12, the arrows represents the displacements of the material. Equations Eq.1.36 can be solved analytically just for very simple cases. At a given frequency, there are an infinite number of wavenumbers, either real or purely imaginary, that can solve Eq.1.36. To each wavenumber corresponds a wave mode, but just the modes deriving from real wavenumber are considered. Hereinafter the symbols S_i and A_i are used to define the symmetric and the anti-symmetric modes, respectively, with the subscript indicating the order of the mode. Equations in Eq.1.36 also indicate that the Lamb waves, regardless of mode, are dispersive, because velocity is dependent on frequency. For this reason dispersion curves can be plotted. This curves represent how the phase velocity $c_p = \omega/k$ or the group velocity vary with the frequency. An example of dispersion curves plotting the phase velocity, as function of the frequency-thickness product, for an aluminum plate is shown in Fig.1.13. In this figure are reported both the symmetric and the anti-symmetric Lamb waves modes up to the second order. It can be noticed that for lower frequencies just two Lamb waves mode

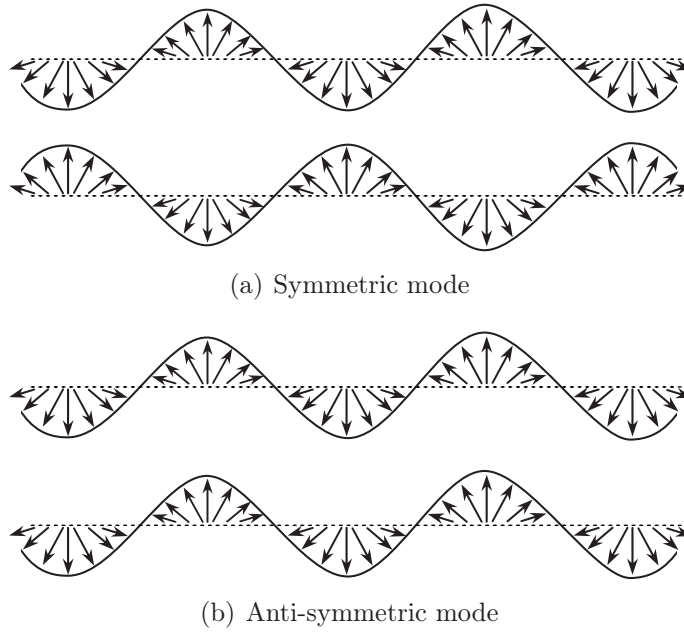


Figure 1.12: Symmetric and anti-symmetric Lamb wave modes

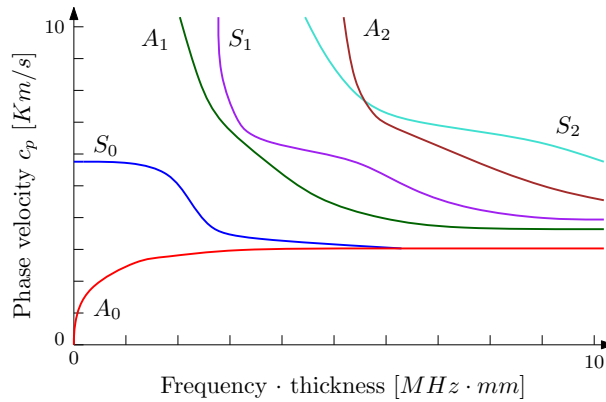


Figure 1.13: Phase velocity dispersion curves for an aluminum plate

are present. This means that the other modes, for those frequencies, have imaginary wavenumbers.

In a plate, in addition to the Lamb waves modes, there also exists a set of wave motions known as shear horizontal (SH) modes. The particle displacements caused by any of these SH modes are in a plane that is parallel to the surface of the plate, as shown in Fig.1.14. In this figure the wave propagates in direction x_1 and the particles displacements are in the direction

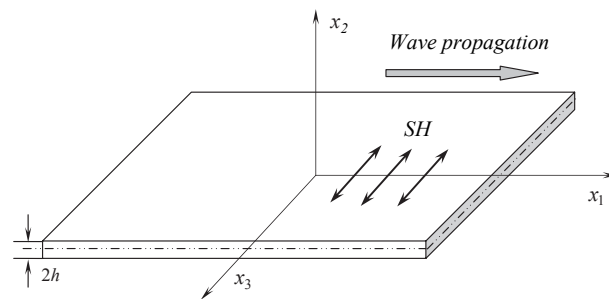


Figure 1.14: SH wave mode propagation

x_3 . Also the SH modes derive from the superpositions of the fundamental bulk waves. However these modes do not have such an important role in SHM applications, so the interest in this work is focus mainly on Lamb waves modes.

1.3 Objective of the present work

Because of the importance of the guided waves in plates for SHM applications and their complex nature, especially in composite laminates, a FE model of this phenomenon can not present flaws. Thus a validation of this modeling technique must be provided in order to guarantee the correct wave propagation in every direction of the plate. The wave should propagates with correct wavenumber and with the correct wavefront, even in composite materials, which could present any orientation of the plies and a strong orthotropic behavior for each ply.

Chapter 2

Finite Element modeling for wave propagation in isotropic and anisotropic plates

The first step in the present work is to create a model using Finite Elements (FE) that can represent how the waves move into a plate. This is not a simple task because the phenomenon involved is very fast, the spatial scale is small and, especially for composite materials, the results in literature are few. For these reasons the first FE model created has the objective to find the sensibility of the results to different kinds of parameters and to set up these parameters. The material adopted for the first model is aluminum, which is isotropic, because it gives simpler results than composite materials and because there are a certain number of references in literature. The second FE model developed represents an anisotropic plate, made of composite laminates. Both plates are modeled by using solid elements and composite plate model employs one solid layer for each ply. The solid composite model is then used as a reference for assessing a new modeling technique, which was developed at Dipartimento di Ingegneria Aerospaziale (DIA) of the Politecnico di Milano, that uses both shell and solid elements to model a composite material. The sequence of lamination, the number of plies, the material adopted for these anisotropic plates have been selected basing on the characteristic of the panels that have been produced at Politecnico in order to carry out experimental measurements. All the numerical analyses are carried out by the explicit finite element software Abaqus/Explicit, whose details are defined in the first section of this chapter.

2.1 Overview of Abaqus/Explicit

The explicit dynamic analysis software Abaqus/Explicit is part of the Abaqus suite of programs. This kind of analysis is computationally efficient for large models with relatively short dynamic response times and for the analysis of extremely discontinuous events or processes. The explicit dynamics procedure performs a large number of small time increments efficiently. An explicit central-difference time integration rule is used [16]. Each increment is relatively inexpensive because there is no need for solving a set of simultaneous equations. The explicit central-difference operator satisfies the dynamic equilibrium equations at the beginning of the increment t . Then the accelerations calculated at time t are used to advance the velocity solution to time $t + \Delta t/2$ (Eq.2.1) and the displacement solution to time $t + \Delta t$ (Eq.2.2).

$$\dot{\mathbf{u}}_{(i+\frac{1}{2})} = \dot{\mathbf{u}}_{(i-\frac{1}{2})} + \frac{\Delta t_{(i+1)} + \Delta t_{(i)}}{2} \ddot{\mathbf{u}}_{(i)} \quad (2.1)$$

$$\mathbf{u}_{(i+1)} = \mathbf{u}_{(i)} + \Delta t_{(i+1)} \dot{\mathbf{u}}_{(i+\frac{1}{2})} \quad (2.2)$$

where $\dot{\mathbf{u}}$ is the velocity and $\ddot{\mathbf{u}}$ is the acceleration. The explicit integration rule is simple but by itself doesn't provide the computational efficiency associated with the explicit dynamics procedure. In fact, the possibility to speed up the solution process is provided by the arrangement of mass and inertia properties of the model into a diagonal mass matrix.

The central difference operator is not self-starting because at $t = 0$ the value of the mean velocity $\dot{\mathbf{u}}_{(-\frac{1}{2})}$ needs to be defined. So the condition Eq.2.3 can be asserted.

$$\dot{\mathbf{u}}_{(+\frac{1}{2})} = \dot{\mathbf{u}}_{(0)} + \frac{\Delta t_{(1)}}{2} \ddot{\mathbf{u}}_{(0)} \quad (2.3)$$

Substituting Eq.2.3 into Eq.2.1 yields the definition of $\dot{\mathbf{u}}_{(-\frac{1}{2})}$ reported in Eq.2.4.

$$\dot{\mathbf{u}}_{(-\frac{1}{2})} = \dot{\mathbf{u}}_{(0)} - \frac{\Delta t_{(0)}}{2} \ddot{\mathbf{u}}_{(0)} \quad (2.4)$$

The central difference operator is conditionally stable, that is the maximum value of the time increment Δt must be limited to assure stability. This limit, for a case without damping is related to the highest eigenvalue in the system, according to Eq.2.5.

$$\Delta t \leq \frac{2}{\omega_{max}} \quad (2.5)$$

If some kind of damping is introduced in the model, the stable time increment

is reduced accordingly to Eq.2.6.

$$\Delta t \leq \frac{2}{\omega_{max}} \left(\sqrt{1 + \xi^2} - \xi \right) \quad (2.6)$$

Abaqus/Explicit estimates the maximum frequency of the entire model and with this information it automatically chooses the right time increment to use in the integration. Actually this estimation is continuously updated. However for some analysis the time increment can be manually inserted. Practical procedures to choose the right value will be described in the next section.

2.2 Model of an isotropic plate

The FE model of a plate is created using Abaqus/CAE (Complete Abaqus Environment), the modeling software in the Abaqus suite of programs. Since the purpose of the present work is the study of the propagation of guided waves, that is the study of the local effects due to material deformation in three dimensions, solid elements are adopted for the model. This choice is preferable to the use of shell elements, which anyhow can not model the symmetric mode, because of the contemporaneous extension or compression of both sides of the plate. Moreover a more detailed propagation of the wave through the thickness could be achieved. The next paragraphs report the parameters adopted for the FE models and how they influence the results.

Orientation: The plate is positioned in the x-z plane, so the y axis is normal to the plate. The origin of the axis is located in one of the vertex of the plate. The displacements along the three axes are reported in Tab.2.1.

	Name
Displacement along x axis	U1
Displacement along y axis	U2
Displacement along z axis	U3

Table 2.1: Displacements along the axes of the model

Element type: The elements adopted to model the plate are the ones called C3D8R by Abaqus (Fig.2.1). This abbreviation denotes a solid (Continuum) element, in 3D space, defined by 8 nodes, with reduced integration.

Actually this is the classical linear brick element, with reduced integration and hourglass control, which is used in explicit dynamic FE computations. Stress or displacement analyses, using linear reduced integration elements,

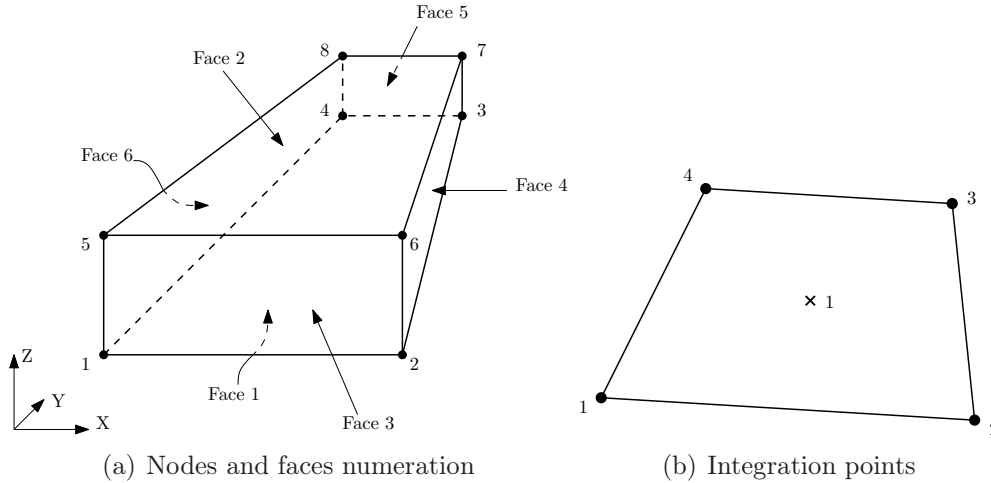


Figure 2.1: Linear brick element with reduced integration and hourglass control (C3D8R)

can lead to hourglass problems. Since the elements have only one integration point it is possible to distort them in such a way that the strains calculated at the integration point are all zero, which in turn leads to uncontrolled distortion of the mesh. To control hourglass in C3D8R elements the artificial stiffness method and the artificial damping method, described in [17], are used. Despite this inconvenient the reduced integration is useful in reducing the computational cost, that could be very high for this kind of problems and prevents the phenomenon of the locking, that affects bending problems, as the one dealing with the propagation of flexural mode A_0 .

The mesh for wave propagation analysis should be the most regular as possible to avoid spurious dispersions and reflections [18]. For this reason the plate is modeled by a structured mesh and, to further increase the regularity, elements square in plan are adopted.

Material: The material used for this first model is aluminum, that is isotropic. This property imply that the guided wave in the plate, which are generated by the excitation of a point of the plate, must propagate with a perfect circular front, because the characteristics of the material are the same in each direction. This phenomenon is a first indicator of the model quality. If the propagating wave, which is represented by the analysis, does not assume a circular shape around the excitation point, that means that

the model must be corrected. The properties of aluminium are reported in Tab.2.2. To insert these data in Abaqus the material ISOTROPIC is used. In

	Units	Value
Young's modulus	[MPa]	72000
Density	[kg/m ³]	2700
Poisson's ratio		0.33

Table 2.2: Properties of aluminum adopted for the isotropic model

this work the consistent system of units adopted for all the models is tons, millimeters, seconds. In this way the force units are newton and stresses are expressed in mega-pascal (MPa).

Internodal distance: Element size has a great importance in wave propagation analysis because it affects the minimum wavelength that can be represented in the analyses. Accordingly, the element size along the direction of propagation, must be small enough to catch the shortest wavelength produced. Moreover the number of nodes per wavelength should be at least 6, to get a good representation of the wave. For a structured mesh the length to be considered is not the distance between two adjacent nodes, but the distance between the opposite nodes (along the diagonal of the brick element, in a FE scheme), so the term internodal distance is used instead of element size. To determinate the maximum internodal distance L_{max} the Eq.2.7 can be used [9].

$$L_{max} < \frac{\lambda_{min}}{\sqrt{2}n_{min}} = \frac{c_{gmin}}{\sqrt{2}n_{min}f} \quad (2.7)$$

The term f is the frequency, the n_{min} is the number of nodes per wavelength, at least 6 and c_{gmin} is the minimum group velocity expected, which actually depends on the frequency. The group velocity dispersion curves of the aluminum can be found in literature as it is reported in Fig.2.2. Researchers in the field of Lamb wave propagation for health monitoring usually consider frequencies of the order of some hundreds kilohertz [2, 9]. In this work a frequency of 200 kHz is used, so the expected c_{gmin} is about 2300 m/s for a plate 1 mm thick. With this value of c_{gmin} the L_{max} , using $n_{min} = 8$, must be shorter than 1.44 mm, that means the longest side of an element, square in plan, must be shorter than 1.02 mm. As a consequence the element adopted in this isotropic model has the dimension of 1 mm in the plane of wave propagation, whereas to define the thickness the aspect ratio must be taken into account.

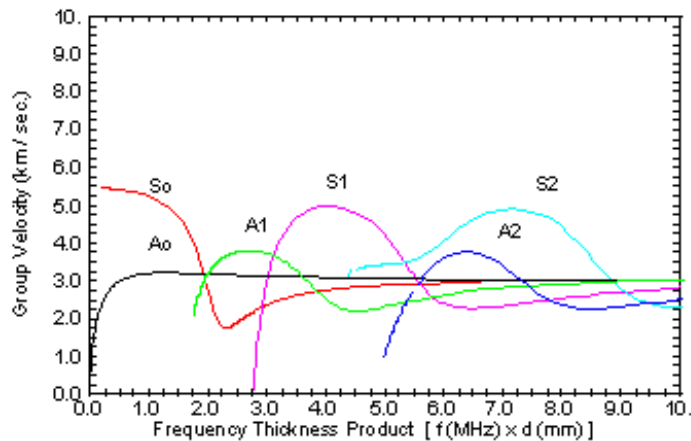


Figure 2.2: Group velocity dispersion curves of Lamb waves in Aluminum

Aspect ratio: A quite detailed mesh in the through-the-thickness direction is required to investigate wave propagation in a plate. This is not only true for composite material, in which each ply can be modeled with a layer of elements, but also for isotropic materials, in order to get more accuracy. However the thickness of the plate can be very small with respect to the other dimensions, so if cubic elements, with an optimal FE performance are used, the dimension of the problem becomes too large and computational cost becomes unacceptable. The problem can be solved using stretched elements, in which the thickness is smaller than the other dimension. The ratio between the longer side of the element and the shortest is referred as aspect ratio (AR), as can be seen in Fig.2.3. For the same number of elements through

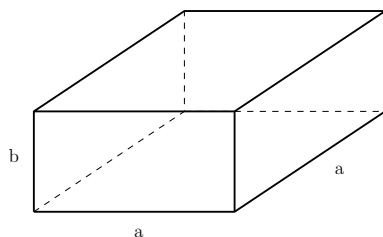


Figure 2.3: The aspect ratio of the element is $AR=a/b$

the thickness, the number of elements in the model is inversely proportional to AR. Accordingly, high AR's imply shorter time for the analysis, but an excessively high AR can produce inaccurate results. The maximum value of AR that can be used safely for a specific model must be determined after

a series of trials. Some preliminary tests lead to accept, for the model of the isotropic plate, an aspect ratio of 3. As said in the previous paragraph, the size of the element in the plane of wave propagation is 1 mm, so an AR of 3 means that the thickness is discretized by 3 elements 0.333 mm thick. Actually, the employment of three solid elements through the plate thickness with a reduced integration scheme is not completely adequate to capture bending behavior of a plate. Nevertheless, the model should be able to capture the essential aspect of propagation and comparison with more refined model will be provided. A table reporting the dimensions of the element adopted to model the isotropic plate is Tab.2.3.

	Units	Value
Width	[mm]	1
Length	[mm]	1
Thick	[mm]	0.333

Table 2.3: Dimensions of the element in the isotropic model

Time step: The central-difference integration scheme is conditionally stable, so the time increments, also called time steps, must be shorter than a determined value in order to get convergence. Abaqus/Explicit automatically calculate the time step, but it is possible to insert its value manually in order to have more control of the analysis. The value of Δt is given by Eq.2.8

$$\Delta t \leq \frac{L_{min}}{C_d} \quad (2.8)$$

where C_d is given by Eq.2.9

$$C_d = \sqrt{\frac{1}{\rho} \frac{E(1-\nu)}{(1+\nu)(1-2\nu)}} \quad (2.9)$$

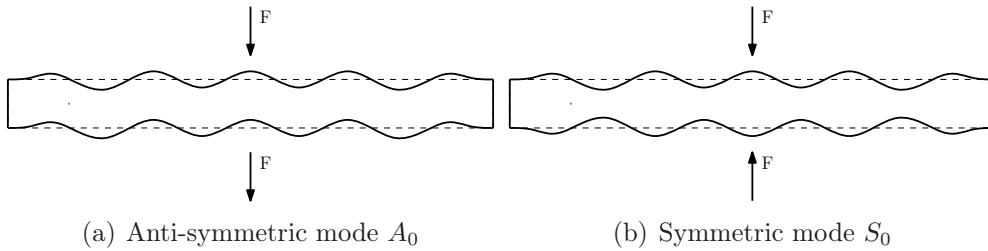
that is the dilatational wave speed, that for aluminum is 6286m/s. The time step adopted for this first model should be shorter than 3.977e-8 seconds, the values adopted are reported in Tab.2.4. The observation time is calculated to allow the slowest wave, that is the anti-symmetric mode A_0 , to reach the boundaries and to be reflected back to the excitation point.

Input: The application of a load normal to the plate can be used to simulate the effect on an excitation, which in structural health monitoring is

	Units	Value
Time step	[s]	3.500e-8
Observation time	[s]	4.000e-5

Table 2.4: Time step and observation time

often accomplished by means of piezoelectric actuators (PZT), even if more accurate models can be found, as the one described in [9]. The load can be applied just on one side of the plate, exciting both the symmetric S_0 and anti-symmetric A_0 modes of Lamb wave. Applying the force on both sides of the plate can be used to produce either pure shear or pure bending, respectively if the forces have the same or different directions. Therefore the symmetric and anti-symmetric modes of Lamb waves can be generated separately, as can be seen in Fig.2.4. Such an approach, based on two separated

**Figure 2.4:** Pure modes by excitation of the plate on both sides

excitation sources, is mainly used in FE models rather than in lab, because of technical difficulties in positioning the two actuators perfectly, in checking that the force generated is the same and in synchronizing them properly. In the model the load is applied in the center of the plate and just on one side. The value of the load has no importance, because the interest is focused on how the Lamb wave propagates rather than the real value of displacement.

Another important parameter is the frequency of excitation, because the behavior of the Lamb wave significantly changes with the frequency. The 5.5 cycles sinusoid signal is modulated by the Hanning window to reduce the leakage, as reported in literature [2,7–9,19]. The excitation signal in time and frequency domain is shown in Fig.2.5. The signal is defined in tabular mode, as a series of 75 coordinates of time and amplitude. The value of the force, assumed to be 10 N, is multiplied by the amplitude to get the input signal. The force is applied normally to the plate and it is distributed over 9 nodes around the point of application to better represent a finite dimension source of excitation, like a PZT and to reduce the local effects of a concentrated

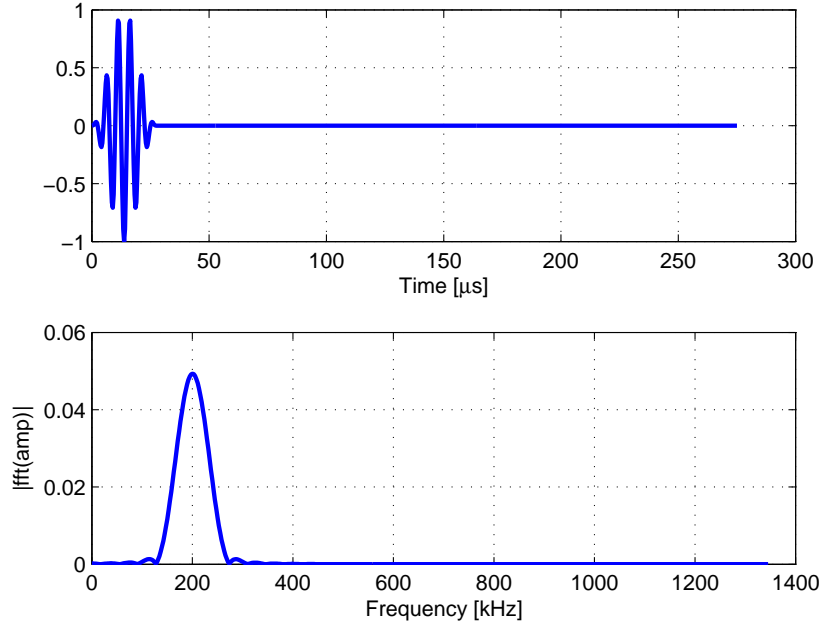


Figure 2.5: Input excitation signal in time and frequency domain, 5.5 cycles at 200kHz

load in a FE model. The characteristics of the input signal are summarized in Tab.2.5.

	Units	Value
Function		Sine
Cycles		5.5
Windowing		Hanning
Frequency	[kHz]	200
Force	[N]	10

Table 2.5: Characteristics of the input signal

Boundary conditions: For a wave propagation analysis the plate is free. There is no constraints of any kind, that because Lamb wave propagates in plate with free boundaries. Also it is worth noting that the free boundary condition is in accordance with the experimental set up of chapter 4.

Output: The information obtained from the analysis of the FE model are the time histories of the displacements of the nodes over the upper and the lower side of the plate. These histories, that will be processed later, are the values that the displacements of the nodes assume during the observation time. Each node of the upper and lower side of the plate can have more time histories, one for each degree of freedom of interest. The degree of freedom used mostly in this work is the out-of-plane displacement U2 because, thanks to the force adopted, the main displacement is in this direction and because both the symmetric and the antisymmetric modes has a component in U2. The time interval used to describe these histories has a different duration with respect the time step required for the analysis. Usually the time interval is chosen in order to get a number of intervals that is a power of two, to improve the efficiency of the Fast Fourier Transform (FFT), that will be used to process the data. Accordingly in this work all the time histories have 512 intervals. Another information that comes from the analysis of the FE model is the so called field output. This output gather the displacements U1, U2 and U3 of all the nodes, to produce a graphical representations of the deformed model at a particular time, or to represent the displacements by colors, or both. The representations of the field output are very useful because they give an idea of how the wave propagates, but they produce a remarkable amount of data. For this reason the field output is taken at no more than 50 intervals during the observation time. The Tab.2.6 reports the characteristics of the output file. Obviously the time histories and the field

	Units	Value
Intervals for time history		512
Information for the time history		U2
Intervals for field output		50
Information for the field output		U1,U2,U3

Table 2.6: Characteristics of the output file

output can be used with other data, as the components of the stress or the strain in the element, the velocities or the accelerations of the nodes, and so on.

Dimension of the plate: The choice of the dimensions of the plate comes after the definition of all the parameters of the FE model. In fact, the model has the purpose to properly describe the propagation of Lamb wave and not to create a model of an existing plate. Accordingly, dimension of the

model must be the largest possible in order to have the wave as developed as possible and to avoid reflection at the boundaries. Moreover a large FE plate has an high spatial resolution in case of a spatial Fourier transform, as the one performed in chapter 3.6. On the other hand the dimensions of the model directly affect the computational cost. Therefore a trade-off between the largest dimension possible and the computational power available is made in order to obtain enough space for the propagation and an analysis time of the order of hours using an average personal computer. With all these premises a plate of the dimensions reported in Tab.2.7 is created. In Fig.2.6

	Units	Value
Plate width	[mm]	72
Plate length	[mm]	96
Plate thick	[mm]	1

Table 2.7: Dimensions of the plate

the dimensions of the plate and the position of the concentrated load are reported. These dimensions, except for the thickness, will be maintained

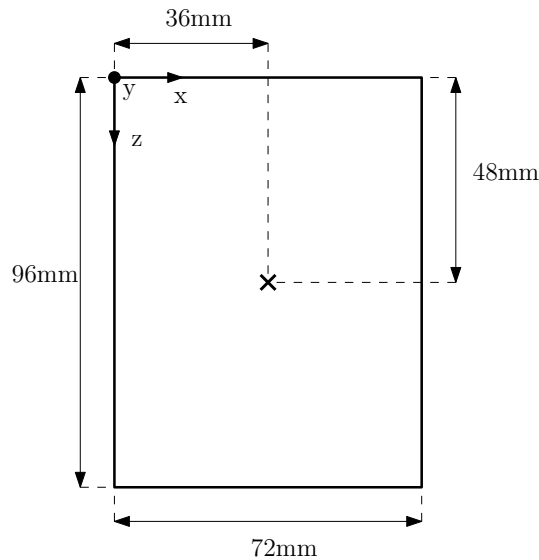


Figure 2.6: Dimensions of the plate and position of the load

also for composite plates models.

Model: The choices of all parameters leads to the FE model that is reported in Fig.2.7. The red dots indicates where the load is applied. The

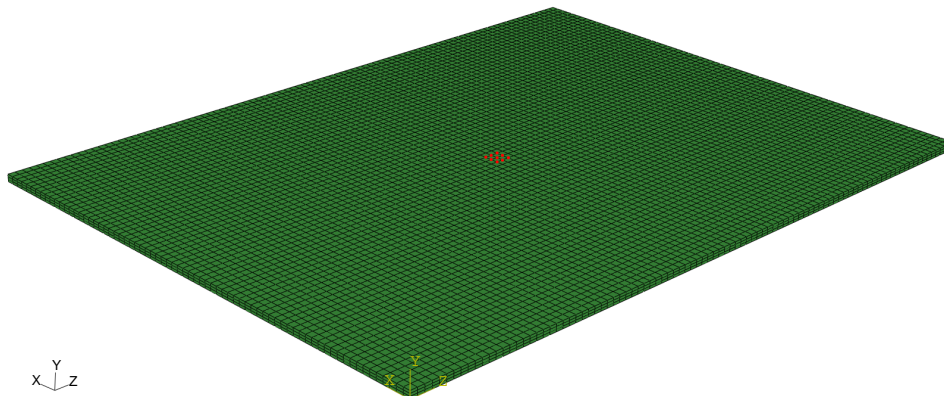


Figure 2.7: Model of the plate

dimension of the finite element analysis for the isotropic plate is reported in Tab.2.8 along with the computational time required. The computational

	Units	Value
El. number		20736
Degrees of freedom		84972
Computational time	[s]	57

Table 2.8: Dimension of the FE problem and computational time for the isotropic plate

time is very short because the isotropic model is simple and just three elements are used to discretize the thickness. This time is much greater for the anisotropic plates, even if the width and the height are the same.

2.3 Wave propagation in an isotropic plate

In this section the output of the finite element model defined previously is examined. Now the attention is on the field output, to have a graphical representation of the out-of-plane displacement U_2 in the whole plate. This component measures more efficiently the anti-symmetric mode A_0 , that has the largest part of its displacement in this direction, whereas the symmetric mode S_0 , that has mainly an in-plane displacement, has a reduced visibility. The expected result is a wave that circularly propagate around the excitation

point, because the isotropic material has the same mechanical properties in all directions. The results in Fig.2.8 are referred to wave propagation in the plate at different times. The wave propagates circularly as expected. The

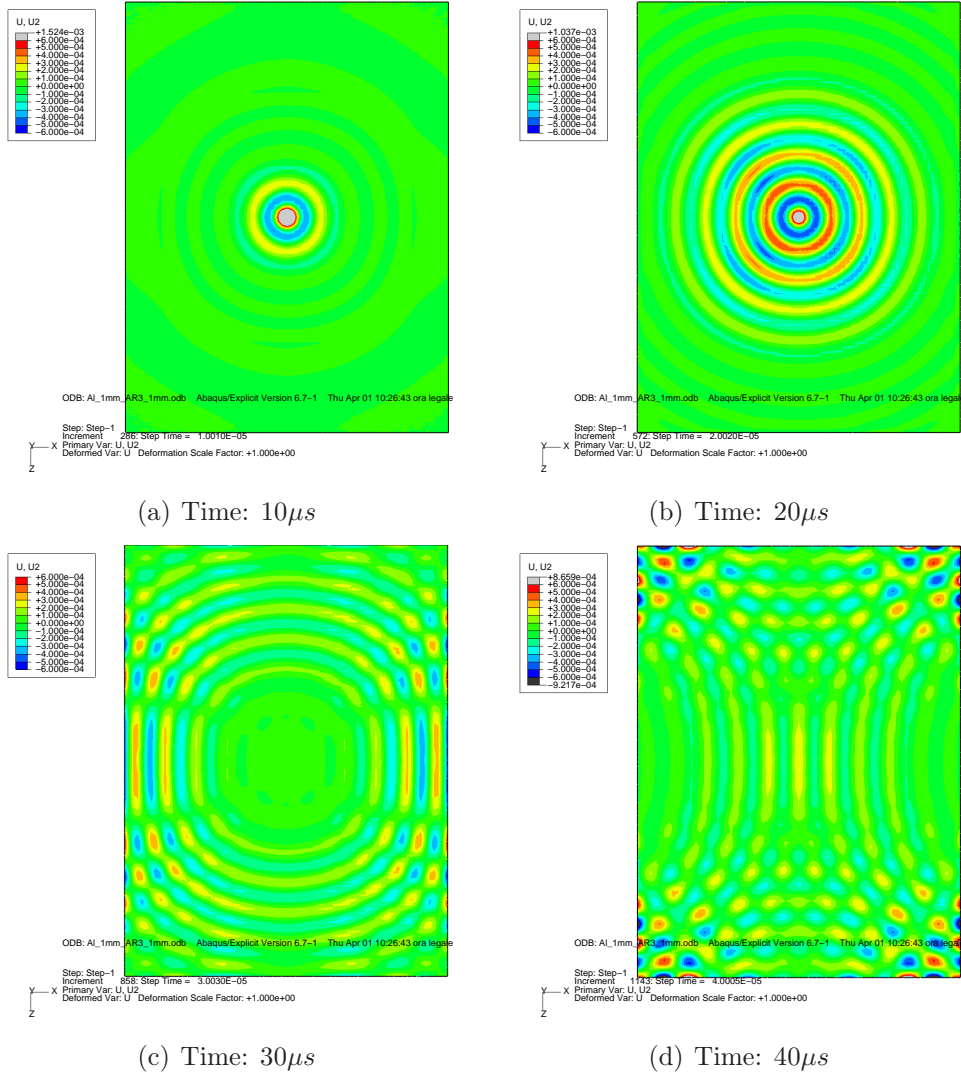


Figure 2.8: Field output of the out-of-plane displacement U_2 for the isotropic plate

only wave visible in these results is the anti-symmetric A_0 , as can be seen looking at the deformed cross-section along the long side of the plate, Fig.2.9. The S_0 waves exist, but their component of displacement in the out-of-plane direction is very low. Moreover, the type of excitation, which employs only a force on one side of the panel, generate A_0 waves with large amplitudes,

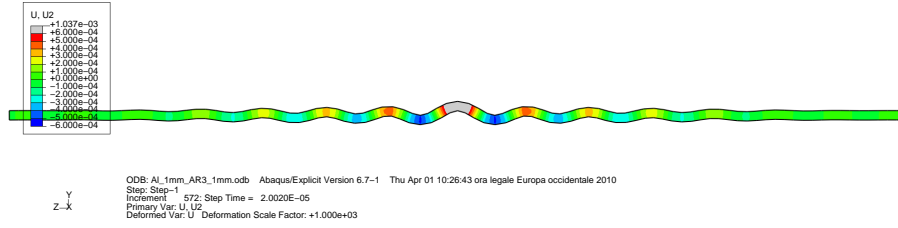


Figure 2.9: Cross-section deformation along the long side of the plate at $20\mu s$

which tend to hide the S_0 content. A confirm of the ability of this model to reproduce also the S_0 mode is given in Sec.2.4, where the excitation is expressly designed to produce symmetric waves.

2.3.1 The aspect ratio behavior

As said previously an high aspect ratio can reduce significantly the number of degree of freedom of a FE problem, reducing also the computational time, but an AR too high produces inaccurate results as the one that is shown in this example. Two plate, of the same size and material defined in the previous section, are discretized with element of AR 3, using four elements in the thickness and a size in plan of 0.75 mm, and AR 6, using eight element in the thickness and the same size in plan. The out-of-plane U2 field output of the two model is reported in Fig.2.10. For AR 6, as

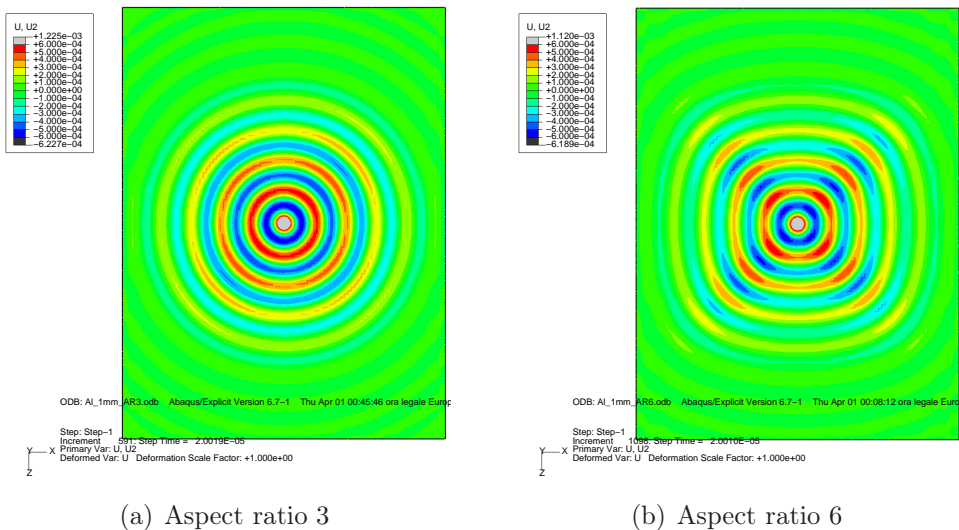


Figure 2.10: Field output of the out-of-plane displacement U2 for isotropic plate at different aspect ratios

can be seen in Fig.2.10(b), even if the size in plan is the same of AR 3 and the number of element through the thickness is the double, the A_0 wave do not propagate circularly, as it ought to be for isotropic materials, but it is stretched along the directions of the diagonals of the elements. This is not a problem of element size, because the maximum internodal distance must be 1.44 mm and in these models it is 1.05 mm, but a problem of element distortion. The element distortion can be accepted until a certain value, its maximum is determined after a series of tries. The presented results indicate that the issues regarding the aspect ratio can be considered more important than the through-the-thickness mesh refinement. A trade-off must be pursued, which can provide an adequate description of through-the-thickness behavior, avoiding the distortion due to aspect ratio and obtaining, at the same time, a reasonable computational time.

2.4 Other application of wave propagation in isotropic plates

The hints given so far for the proper realization of a FE model for an isotropic material, can be used also to create a model to study the scattering of a Lamb wave after its impact with a discontinuity in the material. The waves that are scattered can be of different kind with respect the impacting one, moreover they do not propagate uniformly, but their amplitude change with the direction. The study of scattered waves allows not only to determine the possible presence of a defect in the structure, but also its position, its dimension and eventually its shape. The research about these possibilities is still in progress, however in this work the main objective is to validate FE methods to model the correct propagation of Lamb waves, so the application of the FE described in this section is made just to test if any sort of scattering is reproduced and no validation analyses is done on this argument.

Several articles are available on this argument; the one chosen as reference is [20], which presents an analytical three dimensional theory to describe the scattering of a symmetric Lamb wave S_0 due to a circular partly through-thickness hole in a plate. This theory is based on adimensional measures to define the frequency and the dimensions of the hole, but finite dimensions can be defined starting from the thickness of the plate and the definition of the material. Different results are reported for different nondimensional parameters, related to the frequency of excitation and the depth of the hole, but in this work it is chosen to create only one FE model for a specific combination of the parameters proposed. The characteristics of the chosen model

are reported in Tab.2.9. Accordingly to [20] the scattered waves are both

	Units	Value
Material		Aluminum
Plate thickness	[<i>mm</i>]	1.27
Excitation frequency	[<i>kHz</i>]	316.77
Hole radius	[<i>mm</i>]	5.08
Hole depth	[<i>mm</i>]	0.635

Table 2.9: Characteristics of the model for the scattering analysis

A_0 and S_0 Lamb waves and the shear wave SH_0 . The available theoretical results are the maximum amplitudes of this waves at a defined distance from the hole for every direction.

To get the same kind of results using a FE technique it is necessary to create two models, one with the partial hole and one without. By applying the same excitation to both models and measuring the displacements in the three directions at a series of nodes, at the same distance from the hole and on both the sides of the plate, it is possible to clean the values measured in the damaged plate by subtracting the values measured in the undamaged one. Such a procedure allows the identification of the behavior of the scattered waves. Thanks to the feature of the chosen pre-processing tool for the creation of the model (Abaqus/CAE) it is possible to change just a small part of the model instead than modeling from the beginning another plate. Accordingly the model of the plate is created by inserting a small plate in the main plate, exactly in the center. It is just this small plate that is modeled differently to create the two models required, whereas the other parts of the model are identical. Moreover, to reduce the dimensions of the problem, just half of the plate is modeled, basing on symmetry consideration. A symmetry boundary condition is applied to the nodes on the symmetry plane to impose the constrains: $U1=0$, for the displacements and $UR2=UR3=0$ for the rotations. A sketch of this FE model is represented in Fig.2.11. In order to obtain meaningful results the plate should be large enough to avoid that the waves reflected by the edges could interfere with the scattered waves from the partial hole. Such a requirement actually represents a problem, because a large plate requires a very large number of elements, more than that can be handled with normal PC. For this reason a technique based on a numerical absorbing surface is adopted [21, 22]. This surface is composed of 20 layers of different materials, to whom a damping coefficient is applied, which grows gradually from the inner to the outer layer following a quadratic law, to avoid

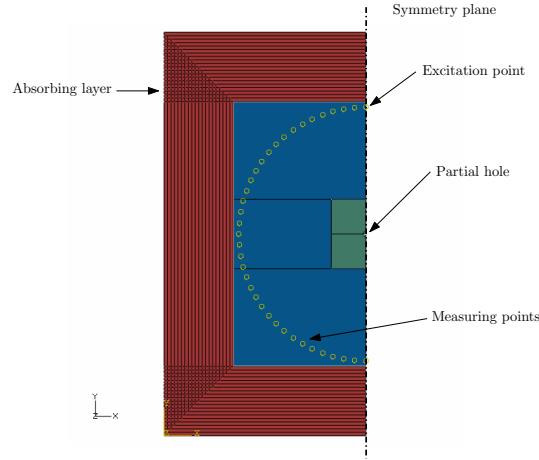


Figure 2.11: Model of the plate for the scattering analysis

any reflection due to the excessive diversity between two adjacent layers. The use of an absorbing surface reduces the number of elements, but also reduces the time step that is used in the explicit analysis. The dependency of stable time step, which has been introduced in section 2.2, on damping coefficient is expressed by Eq.2.10:

$$\Delta t = \frac{1}{\omega_{max}} \left(\sqrt{1 + \xi_{max}^2} - \xi_{max} \right) \quad (2.10)$$

where ω_{max} is the highest frequency of the system, and ξ_{max} is the fraction of critical damping in the mode with the highest frequency. The values of damping coefficients that are assigned to the elements in the absorbing surface are chosen empirically, after a trade-off between the computational time and the effective damping of the reflected signal, which is measured as the ratio between the excitation signal and the reflected signal. In Tab2.10 are reported the tested values. With a damping of $4.5e-7$ s the obtained

Maximum damping [s]	Computational time	Damping ratio
$1.8e-7$	1h	6
$4.5e-7$	2h 10m	30
$9.0e-7$	4h 20m	1000

Table 2.10: Values of computational time and damping ratios for different damping coefficients

results are good, the enhancement of the resulting signal due to doubling the

damping is negligible, so this value is chosen as a good compromise between quality and computational speed. To define the other characteristics of the FE model are taken into account the same considerations of the isotropic model of Sec.2.2. These characteristics are summarized in Tab.2.11.

	Units	Value
Material		Aluminum
Plate height	[<i>mm</i>]	350
Plate width	[<i>mm</i>]	175
Element size	[<i>mm</i>]	$0.75 \times 0.75 \times 0.318$
Aspect ratio		2.36
Elements in thickness		4

Table 2.11: Characteristics of the FE model for the scattering analysis

As already said, measuring the displacement histories in the three directions on some nodes, it is possible to reconstruct the values of the scattered waves, by subtracting the results of the undamaged model to the results of the damaged one. Since the nodes in which the displacements are measured are positioned on a circumference centered in the hole, it is possible to represent the scattered waves using polar plots that reports, for each direction, the maximum amplitude of each waves in that direction. To distinguish the different waves it is necessary to understand which displacement is considered at the node. Accordingly, from the displacements in the three main directions, are computed the displacements along the radius U_r , along the tangent of the circumference U_θ and normal to the plate U_z . The maximum displacement U_r is due to the S_0 wave; the maximum displacements U_θ is due to the SH_0 wave, and the maximum displacement U_z is due to to the A_0 wave. The histories of these displacements, for the node along the 90° direction, are plotted in Fig.2.12(a), whereas in Fig.2.12(b) the Hilbert envelope of those displacement histories is plotted and the maximum values are marked. This envelope enclose the absolute values of the displacements. In signal analysis it shows the modulated signal neglecting the carrier one. These plots confirm the assertion made above about the maximum displacements and the corresponding waves. Indeed the first oscillations that present a maximum peak are the ones of U_r displacement; this means that they belong to the fastest wave, the S_0 type. The second peak is due to the displacement U_θ , which is associated to the SH_0 wave. Finally the last peak, which belongs to the U_z displacement indicates that such displacement are associated to the slowest wave, the A_0 . The observation time for this model should be calculated in order to allow the complete passage of the slowest wave, A_0 , through

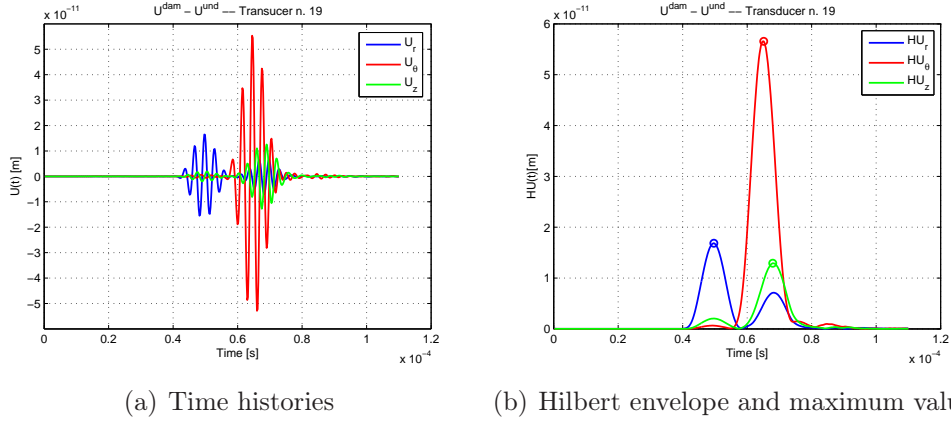


Figure 2.12: Time histories of the displacements along the radius U_r and the tangent U_θ of the circumference of the transducers and perpendicular to the plate U_z

the circumference where measures are taken. These values are reported in Tab.2.12. The results calculated analytically in the reference article are re-

	Units	Value
Radius of the transducers	$[mm]$	110
Observation time	$[s]$	$1.1e-4$
Number of transducers		37

Table 2.12: Position and number of the transducers and observation time

ported in Fig.2.13, the incident wave in these plots arrives from left, that is from the 180° direction. The results computed numerically with the FE model described in this section are presented in Fig.2.14, the values are normalized with respect the maximum value between the three displacements. These two figures show clearly that the FE model adopted can correctly represent the scattered S_0 and SH_0 waves, whereas some problems come from the representation of the A_0 wave, though such problems are attenuated at lower frequencies.

2.5 Model of an anisotropic plate

Solid finite element schemes of composite plates can be created by representing each ply of composite by means of conventional solid elements, stack

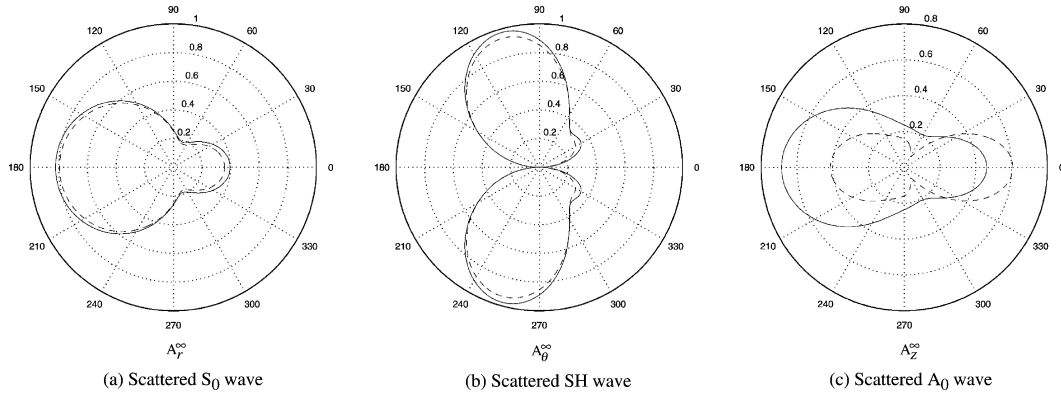


Figure 2.13: Analytical results calculate by Grahn [20] for a partial hole half plate deep

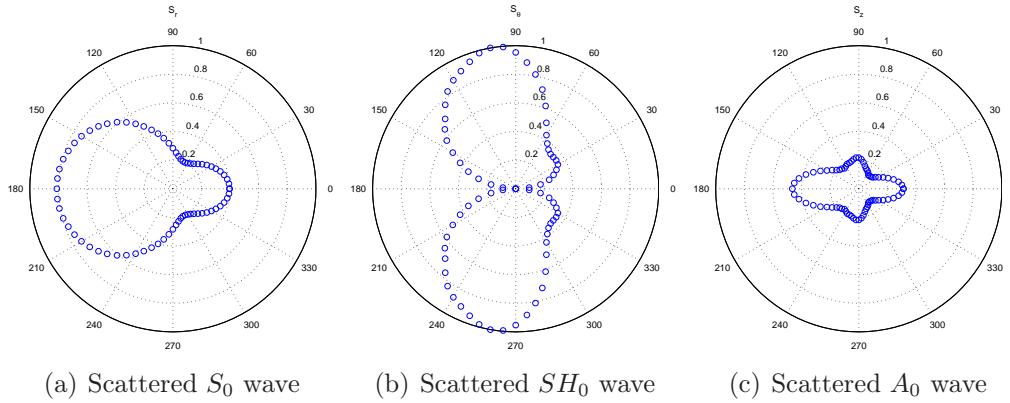


Figure 2.14: Scattering polar plots for a partial hole of 5 mm of diameter, half plate thickness deep and excitation frequency of 316 kHz

all the plies and then merge the coincident nodes. Each ply of composite material is assumed to be an unidirectional laminate, so an orthotropic behavior is assumed. Each layer of solid is characterized by an orientation, which rotates the stiffness properties of the material in the direction consistent with the lamination sequence. In this section the anisotropic plates analyzed in this work are described and the characteristics that the standard FE model must have to reproduce correctly the wave propagation are presented.

Material: The material adopted for the plies are unidirectional laminae made of carbon and glass fibers both in epoxy resin. Each lamina has an orthotropic behavior whose characteristics are reported in Tab.2.13 for the carbon fiber [7] and in Tab.2.14 for the glass fiber (data from DIA). The

	Units	Value
Name		T700/SE84HT
E_{11}	[MPa]	131100
E_{22}, E_{33}	[MPa]	8000
G_{12}, G_{13}	[MPa]	4230
G_{23}	[MPa]	3077
ν_{12}, ν_{13}		0.337
ν_{23}		0.3
Density	[kg/m ³]	1560
Thickness	[mm]	0.144

Table 2.13: Characteristics of the carbon fiber lamina

	Units	Value
Name		S2/CYCOM5216
E_{11}	[MPa]	45670
E_{22}, E_{33}	[MPa]	13600
G_{12}	[MPa]	5700
G_{12}	[MPa]	4000
G_{23}	[MPa]	3000
ν_{12}, ν_{13}		0.257
ν_{23}		0.3
Density	[kg/m ³]	1650
Thickness	[mm]	0.23

Table 2.14: Characteristics of the glass fiber lamina

subscript 11 is referred to a quantity along the direction of the fiber, the subscript 22 to a quantity directed normal to 11, but in the same plane of the lamina and the subscript 33 to a quantity normal to the plane of the lamina.

Lamination sequence: The 0° direction of the laminate is assumed to be along the longest side of the plate. The lamination sequence chosen for the carbon fiber plate is $[0^\circ, 45^\circ, 90^\circ, -45^\circ]_{2s}$, which corresponds to 16 plies symmetrically distributed. The lamination sequences used for the fiberglass plates are $[0^\circ_8]$ and $[0^\circ_2, 90^\circ_2]_s$, both made of 8 plies. These three plates are chosen as they are representative of reference sequences employed in composite manufacturing. The first sequence is quasi-isotropic, due to the uniform

distribution of reinforcement fibers in four directions ($0^\circ, 45^\circ, 90^\circ, -45^\circ$), the second presents a strong discontinuity, because it has the maximum angle possible between two adjacent plies, that is 90° and the last one is unidirectional, thus presents an orthotropic behavior. Calling these plates respectively Plate1, Plate2 and Plate3, Tab.2.15 resumes their characteristics.

		Units	Value
Plate1	Material		T700/SE84HT
	Sequence		$[0^\circ, 45^\circ, 90^\circ, -45^\circ]_{2s}$
	Number of plies		16
	Total thickness	$[mm]$	2.3
Plate2	Material		S2/CYCOM5216
	Sequence		$[0_2^\circ, 90_2^\circ]_s$
	Number of plies		8
	Total thickness	$[mm]$	1.84
Plate3	Material		S2/CYCOM5216
	Sequence		$[0_8^\circ]$
	Number of plies		8
	Total thickness	$[mm]$	1.84

Table 2.15: Summary of the anisotropic plates analyzed in this work

FE model: The FE model is similar to the one used for the isotropic plate: the orientation is the same, the elements are still C3D8R, the boundary conditions are the same, as well as the dimensions of the plate, the input signal and the output requests. The only differences are the material adopted and the through-the-thickness refinement.

In fact, to describe the orthotropic behavior of the single ply, the orthotropic elastic material model, that is available in Abaqus, requires the Young's modulus in the three directions, the three shear moduli and the three Poisson's moduli. This material is defined once, then, for each ply, an orientation is given to define the stiffness matrix of the elements of the layer. The adopted internodal distance is calculated by means of Eq.2.7. Accordingly to the values that can be found in literature [?, 23] the minimum group velocity in the carbon fiber plate is set at 1600 m/s and the one in the fiberglass plate at 1400 m/s. Eq.2.7 calculates that the longest side of an element, it must be 0.94 mm and 0.82 mm, in the carbon fiber and in the glass fiber respectively. These results are obtained for a number of nodes

per wavelength of 6, which is the minimum value to get accurate results. Thus the dimension in plan adopted for the anisotropic plate elements is 0.75 mm, whereas the thickness is the one of the ply. A smaller dimension of the elements would increase excessively the size of the problem.

The aspect ratios that result from these dimensions are AR 5 for the carbon fiber plate an AR 3 for the fiberglass plates. With respect to the isotropic plate, a conceptual visualization of the propagation front is not immediate, so that no reference solution exists to evaluate the correctness of the model. Accordingly AR is kept the lowest level, which is compatible with the, available computational power.

The maximum time steps are calculated using Eq.2.8, for the carbon fiber plate is 1.27e-8 s whereas for the fiberglass plates is 3.964e-8 s, which is similar to the time step of the isotropic plate. This is due to the fact that the ratio of the Young's modulus to the density for the aluminum and the fiberglass is almost the same, whereas for the carbon fiber is more than three times.

All these characteristics can be reported, for the sake of simplicity, in two tables. Tab.2.16 gathers the data common in the three anisotropic plates and Tab.2.17 the data specific of each plate.

	Units	Value
Plate width	[<i>mm</i>]	72
Plate length	[<i>mm</i>]	96
Elements type		C3D8R
Excitation freq.	[<i>kHz</i>]	200
Cycles		5.5

Table 2.16: Common characteristics of the anisotropic plates

2.5.1 Wave propagation in quasi-isotropic carbon laminate

The results that are obtained by applying the previously described technique will be reported considering the first plate (quasi-isotropic carbon laminate). Such analyses will represent a reference for the validation of an alternative modeling technique, which will be employed for all plates and will be described in the next section. As it can be seen in Fig.2.15 the anti-symmetric A_0 wave travels at a slower speed with respect the wave in aluminum, and the shape of the wavefront is not circular, but slightly stretched along a direction

		Units	Value
Plate1	El. size	$[mm]$	$0.75 \times 0.75 \times 0.144$
	Aspect ratio		5
	Time step	$[s]$	1.2e-8
	El. number		196608
Plate2-3	El. size	$[mm]$	$0.75 \times 0.75 \times 0.23$
	Aspect ratio		3
	Time step	$[s]$	3.5e-8
	El. number		98304

Table 2.17: Specific characteristics of the anisotropic plates

that form a small angle with the direction of z axis. The results that are obtained with different aspect ratio show that the distortion of the wavefront can be indeed attributed to material orthotropy, rather than to numerical effects, as the ones discussed in sub-section 2.3.1.

2.6 Alternative modeling technique

At the Dipartimento di Ingegneria Aerospaziale (DIA) of the Politecnico di Milano a modeling technique has been developed and assessed for modeling damage in the interlaminar layers of composite by means of FE explicit computations. Such technique has been developed to study the onset and the development of delamination both under static or impact loads. This technique differs from the approaches that are based on the use of cohesive elements, because creates less expensive models and does not use penalty stiffness or others non-physical parameters. The technique, which is extensively explained in [24], is briefly reviewed in the following sub-section.

2.6.1 Alternative hybrid 2D/3D modeling technique

The approach that is followed to model composite is a modification of the cohesive approaches, which are nowadays employed to model delamination in composites [16]. The final objective is providing the possibility to represent in detail the morphology of interlaminar damage in the simulation of guided Lamb propagation. Although the present work will only try to validate the technique for a material without damage, it will be explained how the approach will be able to model a pattern of interlaminar cracks in the laminate.

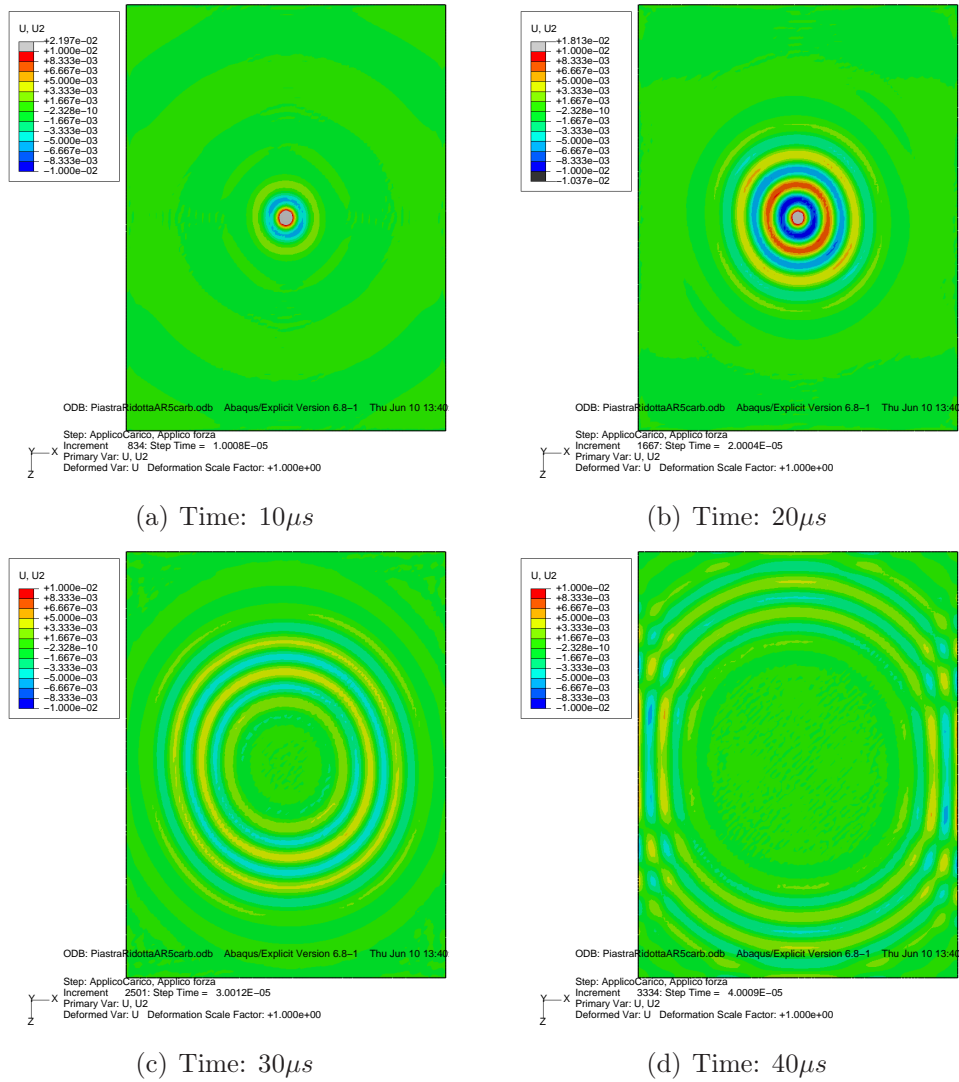


Figure 2.15: Field output of the out-of-plane displacement U_2 for Plate1, modeled with the standard technique

Future works will investigate the possibilities and the limits offered by the techniques.

In the proposed approach composites are represented as a collection of sub-laminates that are modeled by bi-dimensional elements connected by means of solid interlaminar elements. Such a modeling technique is based on the different structural roles that are played by in-plane and out-of-plane stress components in a composite laminate, which can be highlighted by considering some simplifying assumptions.

For the laminate sketched in Fig.2.16 it is assumed that its axes also represent the principal bending directions and that only the shear force V_x and the bending moment M_{xx} act on the laminate without a gradient in the y direction. The general indefinite equilibrium equations in the x direction

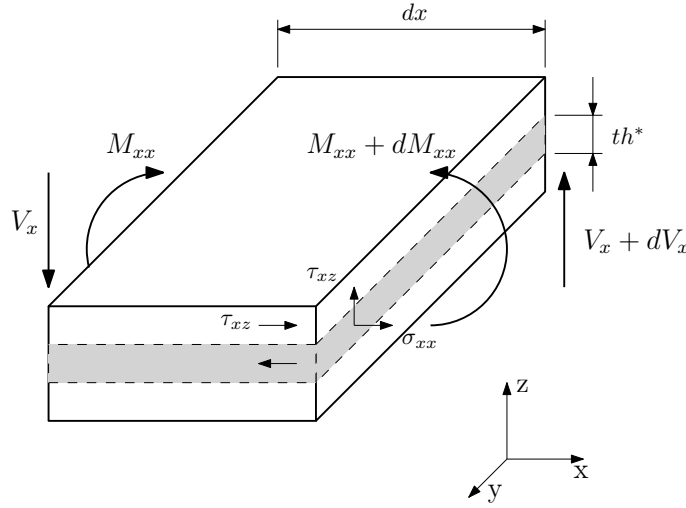


Figure 2.16: Forces and stresses that act on the composite laminate and on the sub-laminate in bending

is given by Eq.2.11

$$\frac{\partial \sigma_{xx}}{\partial x} + \frac{\partial \tau_{yx}}{\partial y} + \frac{\partial \tau_{zx}}{\partial z} = 0$$

$$\frac{\partial \sigma_{xx}}{\partial x} = -div \boldsymbol{\tau} \quad (2.11)$$

The symmetry of the stress tensor implies that the shear components in Eq.2.11 also act in the plane normal to the x axis. So the shear vector in Eq.2.12 can be considered.

$$\boldsymbol{\tau} = \tau_{xy} \mathbf{j} + \tau_{xz} \mathbf{k} \quad (2.12)$$

Now the cross-section area of the considered sub-laminate, which has a width of Δy , can be defined as $th^* \Delta y = A^*$; its boundary is Γ^* and its normal \mathbf{n}_{Γ^*} . The upper and lower surfaces of the sub-laminate are represented by interlaminar layers at z and $z+dz$. In the x direction, the equilibrium of a sub-laminate element with a length dx must take into account the axial flows, N_{xx}^* and $N_{xx}^* + dN_{xx}^*$, which represent the integral of σ_{xx} over the thickness th^* at x and $x+dx$, respectively. Variations of N_{xx}^* turn out to be equilibrated by

the resultant flow of the shear stress that acts in the interlaminar layers that bound the sub-laminate: $\tau_{zx}(z)$ and $\tau_{zx}(z + dz)$. The equilibrium equation of such a sub-laminate element can be obtained by integrating Eq.2.11 over A^* . Applying the Green theorem at Eq.2.11 the integration of the shear vector divergence can be expressed as the flux of $\boldsymbol{\tau}$ across the boundary Γ^* , as in Eq.

$$\begin{aligned} \int_{A^*} \text{div}\boldsymbol{\tau} dA^* &= \frac{\partial}{\partial x} \int_{th^*} \sigma_{xx} dA^* = \frac{\partial}{\partial x} \sigma_{xx} dth^* \Delta y \\ \frac{1}{\Delta y} \int_{\Gamma^*} \boldsymbol{\tau} \cdot \mathbf{n}_{\Gamma^*} d\Gamma^* &= -\frac{\partial N_{xx}^*}{\partial x} \end{aligned} \quad (2.13)$$

The left-hand term of Eq.2.13 represent the flow per unit width of the shear vector $\boldsymbol{\tau}$ across the boundary Γ^* which is defined in Eq.2.14.

$$\phi^* = \frac{1}{\Delta y} \int_{\Gamma^*} \boldsymbol{\tau} \cdot \mathbf{n}_{\Gamma^*} d\Gamma^* \quad (2.14)$$

The flow across Γ^* is composed of two terms that correspond to the flow per unit width across the boundary at z and at $z+dz$, respectively.

Eq.2.13 formalizes the translational equilibrium of a generic sub-laminate during the bending of a composite laminate. The variations of the in-plane stress component resultants, which are the membrane forces that are carried by the plies, are equilibrated by the flows of the out-of-plane shear components that are transmitted through the interfaces with the adjacent sub-laminates. Both in-plane as well as out-of-plane stress components generally vary over the cross-section of the laminate but a structural scheme that is based on their mean values can be considered to approximately represent the laminate. As far as the in-plane stress components are considered, the mean value over A^* , that is N_{xx}^*/th^* , can be taken into account, so that the sub-laminate cross-section can be considered to be lumped at the sub-laminate neutral plane, which, in symmetric sub-laminates, coincide with the geometric mid-planes. Hence, the in-plane response of the sub-laminate turns out to be represented by a bi-dimensional structural element. To approximately model the interaction between the sub-laminates, only the mean value of out-of-plane shear components between the mid-planes of two adjacent sub-laminates can be considered. Such a value represents an approximation of the stress state at the interface that is idealized by the interlaminar layers and will be carried by a connection that only has an out-of-plane response between the sub-laminate mid-planes. According to the proposed scheme, the laminate is modeled by the superimposition of bi-dimensional and connection

elements that interact at the neutral planes of the sub-laminates. Such elements can be interpreted as different material phases that carry in-plane and out-of-plane stress components, respectively. The simplified scheme is shown in Fig.2.17. This discussion can be repeated for equilibrium in y direction,

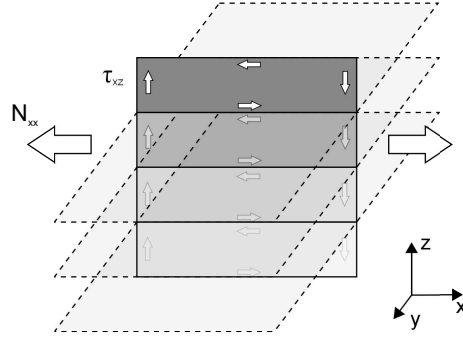


Figure 2.17: Scheme of the composite laminate in the alternative modeling technique

so the connection between the bi-dimensional structural elements transmit both $\tau_{zx} = \tau_{xz}$ as well the $\tau_{zy} = \tau_{yz}$ stress components.

A finite element scheme that is suitable to represent the proposed idealization can adopt bi-dimensional elements to represent the in-plane response of sub-laminates, whereas the connection between sub-laminates can be modeled by elements that have a null in-plane response. The average deformation in the connection element can be linked to the relative displacement between two adjacent sub-laminates, as represented in Fig.2.18. The vector of such a

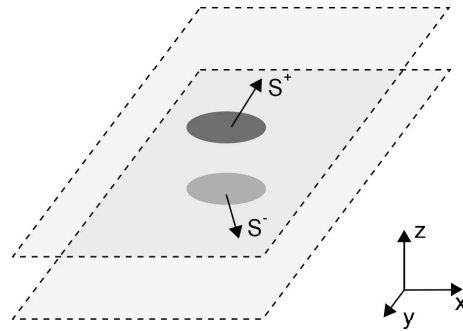


Figure 2.18: Displacements between two adjacent sub-laminates

displacement is defined in Eq.2.15.

$$\Delta = \begin{Bmatrix} \Delta_I \\ \Delta_{II} \\ \Delta_{III} \end{Bmatrix} = \begin{Bmatrix} S_z^+ - S_z^- \\ S_x^+ - S_x^- \\ S_y^+ - S_y^- \end{Bmatrix} \quad (2.15)$$

Within the small strain assumption, the vector Δ can be linked to the average value of the out-of-plane strains that act in the material volume between the sub-laminates expressed in Eq.2.16, where t_k is the distance between the neutral planes.

$$\begin{aligned}\epsilon &= \epsilon_{zz} \ \epsilon_{xz} \ \epsilon_{yz} \\ \epsilon &= \Delta/t_k\end{aligned}\tag{2.16}$$

If a linear 8 nodes solid element, with a reduced integration scheme, is adopted as a connection element between the two bi-dimensional elements, the out-of-plane strain components at its single integration point matches the average strain state that is represented in Eq.2.16. The Abaqus C3D8R represents an adequate choice for the connection element. However, just an out-of-plane response must be included in its constitutive behavior. Moreover, a material orientation has to be attributed to the solid elements so that the local z axis turns out to be normal to the connected sub-laminates. As a consequence of Eq.2.16, the elastic response for such elements can be directly identified by considering the physical out-of-plane stiffness of the material. Eq.2.17 presents a general form of the constitutive behavior that must be employed for solid connection elements.

$$\begin{Bmatrix} \sigma_{zz} \\ \tau_{xz} \\ \tau_{yz} \end{Bmatrix} = \begin{bmatrix} E_{zz} & 0 & 0 \\ 0 & G_{xz} & 0 \\ 0 & 0 & G_{yz} \end{bmatrix} (1-d) \begin{Bmatrix} \epsilon_{zz} \\ \gamma_{xz} \\ \gamma_{yz} \end{Bmatrix}\tag{2.17}$$

In this form is included a scalar damage variable to model the onset and propagation of interlaminar damage by degrading the capability to transmit out-of-plane stress components between the connected sub-laminates. The stress state in linear membrane and solid elements with a reduced integration scheme is constant throughout the elements, so that the equilibrium at each node of the scheme can be easily formalized by considering the sketch in Fig.2.19. The shear stress that acts on the cross-section, which passes through the considered node, can be evaluated as the mean value between the values before and after the node. It can be observed that the variation of $\tau_{xz} = \tau_{zx}$ along the x direction is actually possible only if an external transverse shear force acts on the node. The nodal equilibrium in x direction

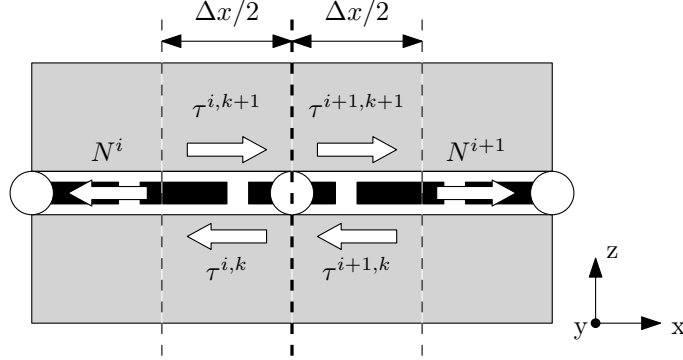


Figure 2.19: Detail of a FE scheme for the alternative modeling technique

for the proposed scheme is expressed in Eq.2.18.

$$\begin{aligned} (\tau_{xz}^{i,k+1} + \tau_{xz}^{i+1,k+1}) \frac{\Delta x}{2} - (\tau_{xz}^{i,k} + \tau_{xz}^{i+1,k}) \frac{\Delta x}{2} &= -(N_{xx}^{i+1} - N_{xx}^i) \\ \bar{\tau}_{xz}^{k+1} - \bar{\tau}_{xz}^k &= \frac{\Delta N_{xx}}{\Delta x} \end{aligned} \quad (2.18)$$

Eq.2.18 is the discrete counterpart of Eq.2.13 since the left-hand term represents the flux per unit width ϕ^* , across a boundary that includes the total area, A^* , of the sub-laminate, which has been lumped at the neutral plane by means of the bi-dimensional element. Hence, the proposed scheme allows the translational equilibrium of the sub-laminates to be fulfilled. A continuum damage mechanics approach that is applied to the constitutive response of a connection element can be employed to model interlaminar damage. The modeling technique does not introduce free surfaces that do not exist at the beginning of the computation and does not require elements that have infinitesimal or zero-thickness. As a consequence, all of the material characteristics can be directly determined on the basis of physical considerations. Moreover, to model N interlaminar layers, only $N+1$ nodes are required, meanwhile other techniques, that are based on separated connection elements, require $2(N+1)$ nodes.

Element type: This technique adopts bi-dimensional elements to carry the in-plane stress and connection element to carry out-of-plane stress. The firsts are modeled using the Abaqus S4R shell element, but also membrane elements can be used, whose thickness is the one of the ply. The solids, as already said, are modeled using C3D8R solid elements with reduced integration rule. The cut out view of the 16 plies Plate1 model in Fig.2.20 shows the disposition of the elements. As it can be observed the number of solid

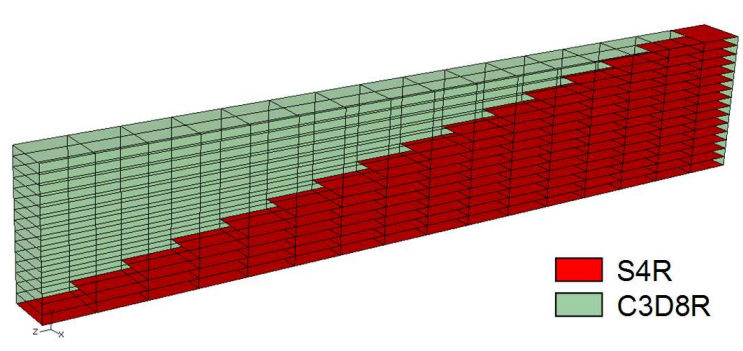


Figure 2.20: Cut out view of Plate1 modeled according to alternative technique

elements through the thickness is 15 because these elements are just the connections between the sub-laminates, whose cross-section can be considered lumped at its mid-plane (which coincide with the neutral plane because the sub-laminate is symmetric), as sketched in Fig.2.21.

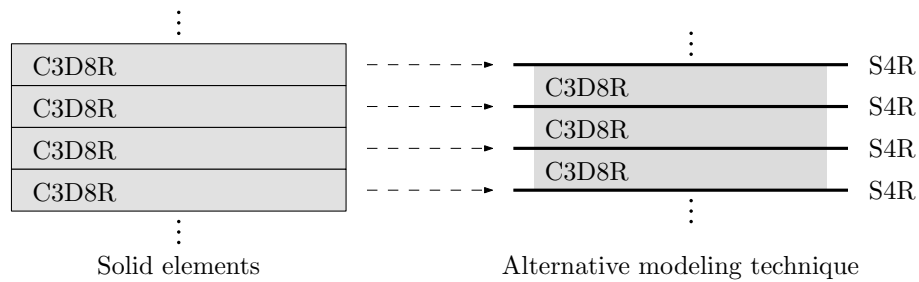


Figure 2.21: Cross-section of the standard and the alternative FE technique to model composites

Material: Each ply is made of orthotropic material, in standard modeling technique is represented by solid elements whose Abaqus material type is `ENGINEERING CONSTANTS`, that requires the nine components of Young's moduli, shear moduli and Poisson's moduli. In the alternative modeling technique the characteristics of the material, reported in Tab.2.13 and Tab.2.14, are introduced for bi-dimensional elements. Therefore the material model adopted to describe their behavior is a bi-dimensional model (`LAMINA` type in Abaqus), which requires just the two in-plane components of Young's modulus, the Poisson's modulus ν_{12} and the three shear moduli of the material. Actually, G_{13} and G_{23} are also required to define the transverse shear behavior for the shells. The benchmark reported in [24] shows that the responses are very similar if shell or membrane elements are adopted. Shell elements

are preferred as they substantially eliminates the risk of hourglass in the computation. Then each lamina is rotated accordingly with the material orientation of the plies.

In the alternative modeling technique the connection elements between the laminae are solids, whose constitutive law has just the out-of-plane response. Moreover a damage can be assigned to this elements by degrading the capability to transmit out-of-plane stresses, as expressed in Eq.2.17, but the axial stiffness E_{zz} is never modified in the case of compressive values of ϵ_{zz} , which model the contact between adjacent sub-laminates, even when the interlaminar layer is completely damaged. This behavior is obtained through a VUMAT subroutine, written in FORTRAN, whose inputs are the components of the stiffness tensor, but only D_{3333} , D_{2323} and D_{1313} have non-zero values and the initial damage, that in this work is always considered zero. This user-defined material is assigned to C3D8R elements. In Tab.2.18 are summarized the characteristics for each type of element.

		Units	Value
S4R	Young's moduli	[MPa]	E_{11}, E_{22}
	Shear moduli	[MPa]	G_{12}, G_{13}, G_{23}
	Poisson's moduli		ν_{12}
C3D8R	Young's moduli	[MPa]	E_{33}
	Shear moduli	[MPa]	G_{13}, G_{23}
	Poisson's moduli		ν_{12}

Table 2.18: Material characteristics for each type of element in the alternative modeling technique

Another important parameter is the density that is attributed to the elements. The two phases, that are modeled by the bi-dimensional and connection elements, are actually superimposed in the FE scheme because they exist in the same volume. Abaqus/Explicit code lump masses and inertia properties at nodes, to obtain a diagonal mass matrix and to simplify the numerical procedure at each integration step. Therefore only the total mass that is attributed to each node of the FE scheme matters. As a consequence, the mass can be freely distributed among bi-dimensional and connection elements. Distribution can be chosen by considering the stiffness of the elements to maximize the stable time step that is required by the computation. Such a choice leads to most of the mass being attributed to the connection element, 9/10, the remaining 1/10 to the bi-dimensional elements, the values are reported in Tab.2.19.

		Units	Value
Plate1	Density C3D8R	$[kg/m^3]$	1404
	Density S4R	$[kg/m^3]$	156
Plate2-3	Density C3D8R	$[kg/m^3]$	1485
	Density S4R	$[kg/m^3]$	165

Table 2.19: Densities adopted for the alternative modeling technique

FE model: The parameters of the FE model using the alternative modeling technique are the same of the anisotropic plate modeled in the standard way: same dimension of the plate, same AR, same time steps, same excitation signal and same request for the output. The dimensions of the solid elements are the same too. The dimensions of the bi-dimensional elements, that have the nodes co-located with the ones of C3D8R, are reported in Tab.2.20 and are the same for all the plates considered. The dimensions of the FE models

	Units	Value
Width	$[mm]$	0.75
Length	$[mm]$	0.75

Table 2.20: Dimensions of the bi-dimensional element in the alternative modeling technique

of the three plates and the computational times are reported in Tab.2.21. These data concern to models that use membrane elements M3D4R, as it

	Plate1	Plate2	Plate3
El. number	380928	184320	184320
Degrees of freedom	600624	300312	300312
Computational time	1h 27m	15m	15m

Table 2.21: Dimensions of the FE problem and computational times for the plates modeled with the alternative technique

can be noticed by the number of degree of freedom that is almost double with respect to the number of elements. The long computational time for Plate1 is due to the very short time step.

2.6.2 Validation of the alternative modeling technique

This technique has been tested to verify the correct representation of the basic behavior of composite laminates in [25]. In that article a carbon fabric plate has been clamped at the one end and loaded at the opposite end by a transverse shear load. A reference model was created by using only standard Mindlin shell elements. The technique has then been assessed by comparing the results of the reference model with the ones of models including an increasing number of interlaminar layers and adopting different types of bi-dimensional elements (shells S4R and membrane M3D4R), whereas the interlaminar layers have always been modeled with C3D8R elements. Two types of analyses have been carried out with two different time histories of the applied load: a triangular impulse with a duration of 1 ms and an amplitude of 50 N (case A) and a terminated ramp, raising from 0 to 50 N in 5 ms (case B). The numerical time histories of the free end displacement are given in Fig.2.22. It can be observed that the differences between the bending re-

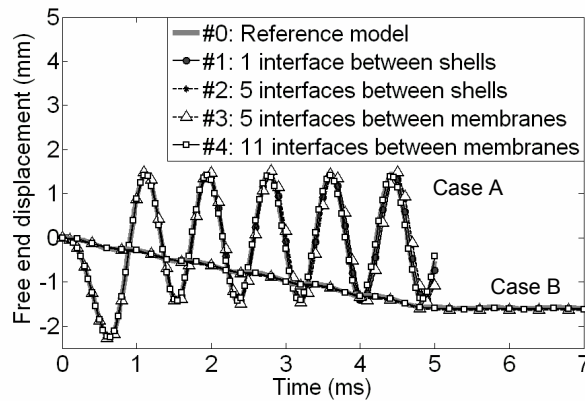


Figure 2.22: Free end displacements of the validation model for different refinements levels

sponses of the models are absolutely negligible. Hence, the obtained results indicate that the application of the technique does not modify the bending stiffness of a laminate.

In the work reported in [26] a plate, made of carbon fiber unidirectional laminae, has been modeled with the alternative technique to verify the correctness of the elastic response. The model is made of 24 shell connected by 23 interface elements C3D8R. The plate has been analyzed in a three-point-bending condition and the validation has been based on the confrontation of the force-displacement curves with the one of a reference model. Such a reference model has been modeled with just C3D8R elements, one layer for

each ply. The load has been applied at the center of the plate, by means of a rigid cylinder, which has been set in contact with the laminate surface. Two other cylinders have been used to model the lateral supports. Although an explicit computation has been performed, velocity conditions has been applied with a very smooth time history, in order to avoid the excitation of the free vibration of the plate and to mimic a quasi-static test. The force-displacement curves are reported in Fig.2.23. Force represents the reaction

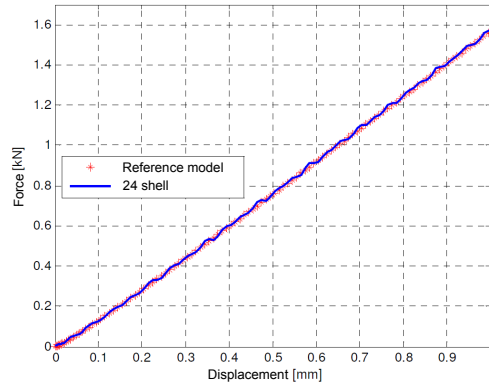


Figure 2.23: Force-displacement curves for the reference and alternative models

at central cylinder, which has been assigned the velocity boundary condition. The validation activity which has been carried out in [26] also included the comparison of the values of various stress components for each lamina. The most significant results are reported in Fig.2.24, Fig.2.25 and Fig.2.26.

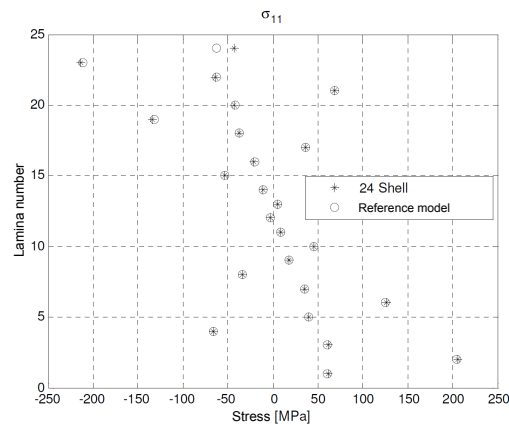


Figure 2.24: Stress component σ_{11} for the reference and alternative models

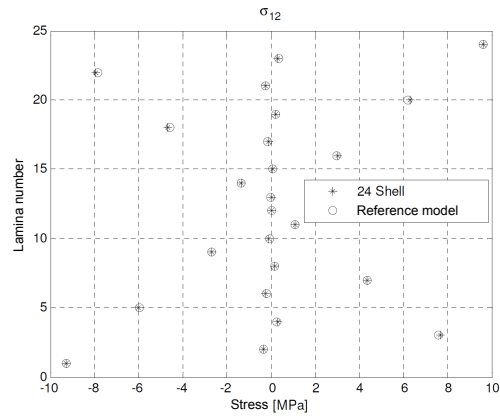


Figure 2.25: Stress component σ_{12} for the reference and alternative models

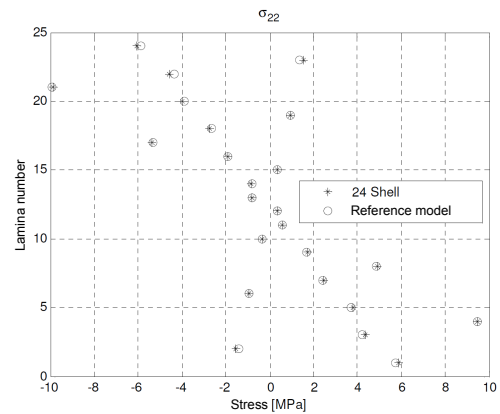


Figure 2.26: Stress component σ_{22} for the reference and alternative models

So far the validations proposed for the alternative modeling technique are limited to almost-static and dynamic analyses in a relatively low-velocity transient. The dynamics involved in the present work are much faster than the one used for the validation, for this reason a confrontation between the standard and the alternative model of Plate1 is considered in sub-section [2.7.1](#).

2.6.3 Motivation for the use of the alternative modeling technique

As already said the alternative modeling technique, has been developed at the DIA to investigate upon the onset and the propagation of interlaminar failures due to static or impact loads. The good results obtained in

determining the correct load for the onset of a crack and the correct pattern of damage development in originally undamaged plates make this approach quite interesting. In particular, damage onset and propagation has been captured without any a-priori assumption on the location of possible delamination. Since a future development of the analyses done with this technique is expected, it can be interesting to use the resulting FE models to study how the guided waves behave in presence of damage to design the best structural health monitoring system. The future scenario can be the following: the design of a SHM system to minimize the maintenance cost and to reduce the safety factors in design and, at the same time, the possibility to analyze the risks of failure of critical component of a composite structure that is heavily loaded or that can be impacted. The numerical non-linear analyses could predict the extent of a damage due to a low energy impact or could evaluate the severity of the damage conditions by means of an estimation of residual load carrying capability. Subsequently, a series of wave propagation analyses could be performed considering the previously analyzed damage scenarios. Such wave propagation analyses, which are the object of the present work, could be employed to study what is the behavior of the waves with the presence of a delamination in order to design the best configuration of a SHM system. Several parameters of the SHM system could be assessed in order to find the best excitation signal, the best position of actuators and sensors in order to get a system that can identify the presence of damage, its position and potentially its entity.

2.7 Wave propagation in anisotropic plates

In this section the results of wave propagation analyses are reported. Analyses are performed using the alternative modeling technique to develop the FE models of the three composite plates defined in section 2.5. The reported results are the field output representation of the out-of-plane displacements U_2 in four time instants, to represent the shape of the wavefront and its evolution. The visualized wave is the one corresponding to the anti-symmetric mode A_0 . The alternative modeling technique can not be represents correctly the symmetric mode S_0 because such representation requires capturing the expansion/contraction effects which are due to the presence of Poisson moduli ν_{13} , ν_{31} , ν_{23} and ν_{32} , which link the in-plane displacements with the out-of-plane ones. The connection elements have only the shear moduli G_{13} and G_{23} and the Young's modulus in the direction normal to the plate E_{33} that can transmit only an anti-symmetric out-of-plane displacement. Applying a force normal to the plate it can be observed a compression

or extension of the thickness, due to E_{33} , but this phenomenon is not coupled with the in-plane extension or compression of the laminae. Such coupling is fundamental to correctly reproduce the symmetric mode S_0 .

The results for Plate1 are displayed in Fig.2.27. As can be seen the results

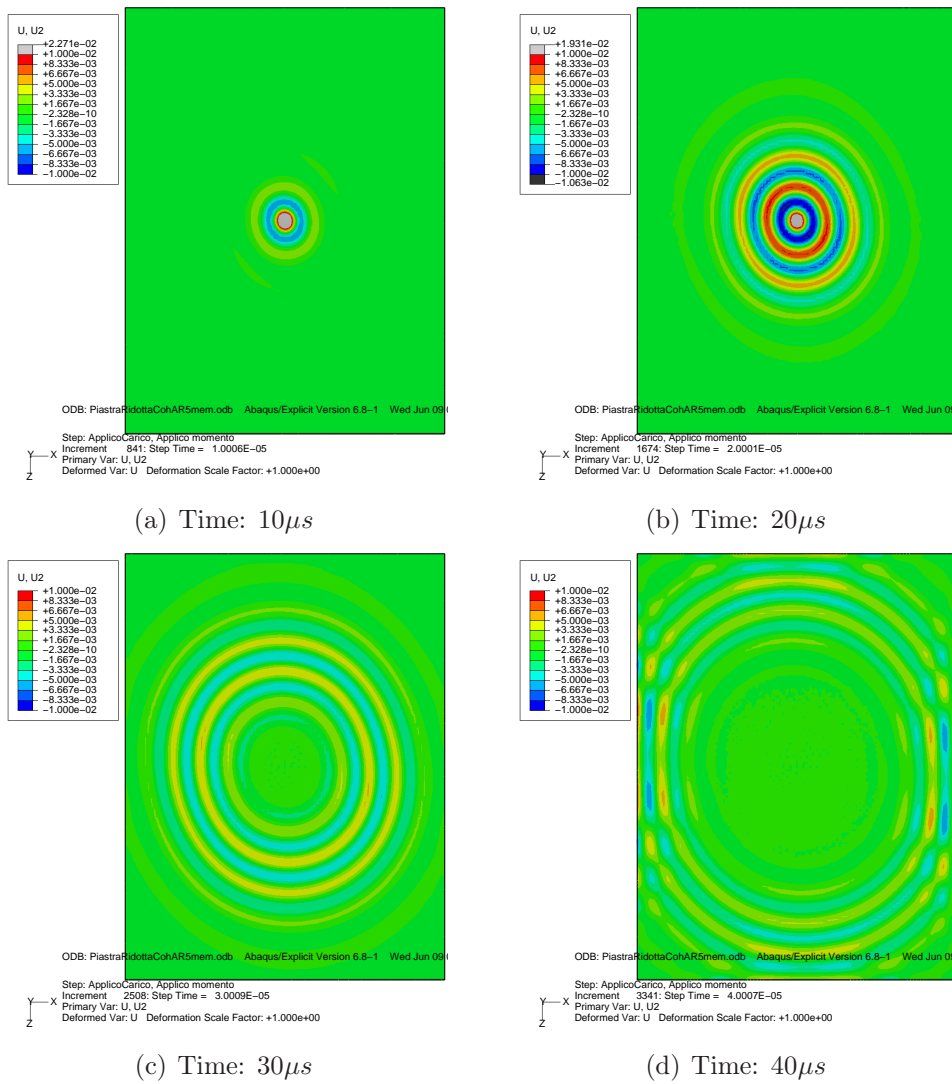


Figure 2.27: Field output of the out-of-plane displacement U_2 for Plate1, modeled with the alternative technique

are similar to those of the same plate modeled with the standard technique in Fig.2.15, but a more specific confrontation is done in sub-section 2.7.1.

The results for Plate2 are reported in Fig.2.28. In this case the shape of the wavefront is slightly stretched along the 0° direction. This is not due to

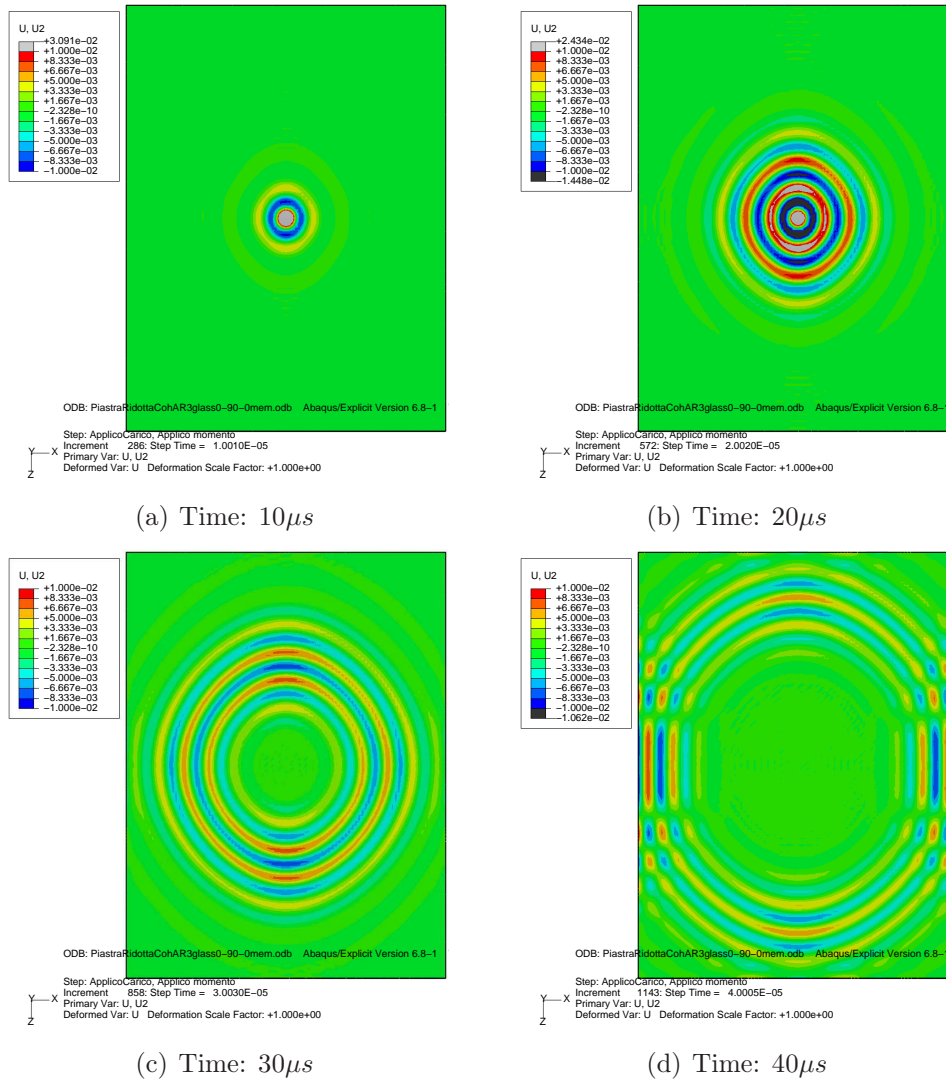


Figure 2.28: Field output of the out-of-plane displacement U2 for Plate2, modeled with the alternative technique

the wrong value of aspect ratio, but to the 0° plies on the upper and lower surfaces of the plate. Since the wave generated by the actuator are mainly flexural waves, the most stressed plies are the external ones that can impose their behavior to the whole plate. The higher value of stiffness along the 0° direction leads to an higher speed of the wave along that direction.

This effect is even more visible in Plate3, the unidirectional plate, in Fig.2.29. The stretching of the wave front is higher than in Plate2 because the mechanism of the wave is always bending, but in this case all the plies

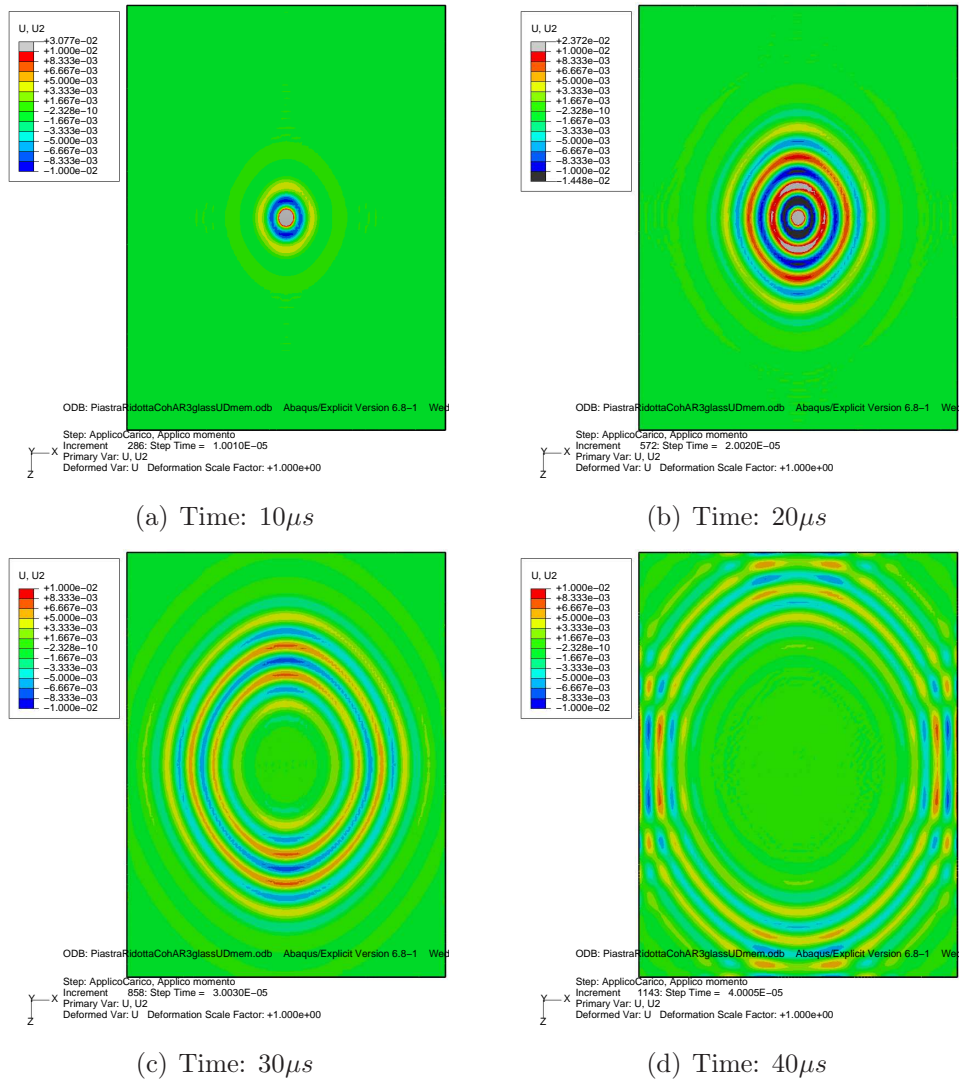


Figure 2.29: Field output of the out-of-plane displacement U_2 for Plate3, modeled with the alternative technique

are oriented along the 0° direction.

2.7.1 Confrontation of standard and alternative technique

As said in sub-section 2.6.2 the alternative modeling technique of composite materials has been validated for almost-static and slow-dynamic excitations. Now a confrontation of the results is proposed between the standard

and the alternative modeling technique of Plate1. The shape of the wavefront, the velocity of the wave, the out-of-plane displacement and the stress histories in the same point are evaluated and compared. The point in which the measurements are taken is at a distance of 6 mm from the excitation point, as it can be seen in Fig.2.30. This point is coincident with a node,

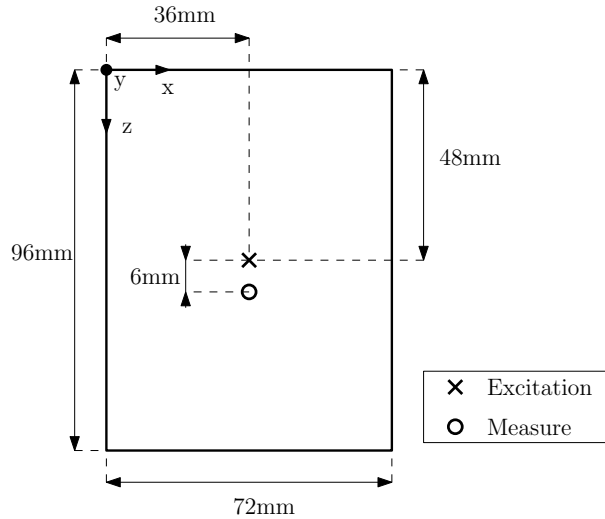


Figure 2.30: Position of the measure point in the plate

on the upper surface of the plate. The U2 displacement time histories are referred to such surface node. The stress histories come from the column of elements that have as nodes the ones coincident with the point just defined.

The shape of the wavefront at $20\mu s$ are compared in Fig.2.31, considering the out-of-plane displacements U2. The wavefront in the two models is the same, which is a little stretched along a small angle, but the alternative technique gives a more uniform wave in all directions. Hence, the alternative modeling technique seems obtaining a lower numerical dissipation of the wave content.

The velocity of the wave can be already deduced by Fig.2.31, in fact the dimension of the two wavefronts are virtually the same, but a more precise analysis is offered by the out-of-plane displacement histories, in Fig.2.32, taken from the upper node of the plate, at the position that has been previously described. Fig.2.32 shows an almost perfect correlation during the excitation phase and the identical prediction for the traveling time of the wave before reflection. This correlation becomes less evident after the arriving of the reflected wave. Moreover the alternative technique presents a smoother curve, whereas the curve of the standard model is noisy. Such a noise is likely to be produced by the symmetric mode S_0 , which is less evident,

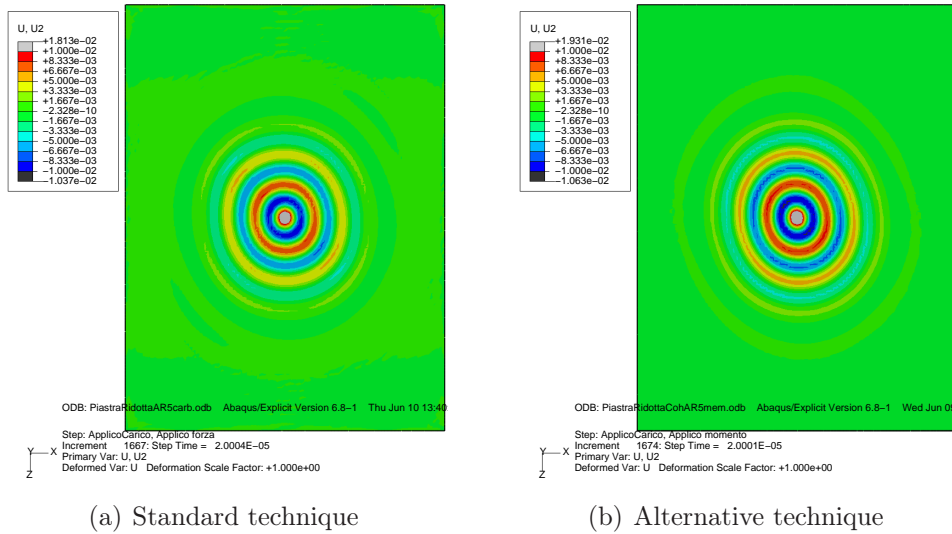


Figure 2.31: Confrontation of the field output of the out-of-plane displacement U_2 for Plate1 at $20\mu s$ for the standard and alternative modeling technique

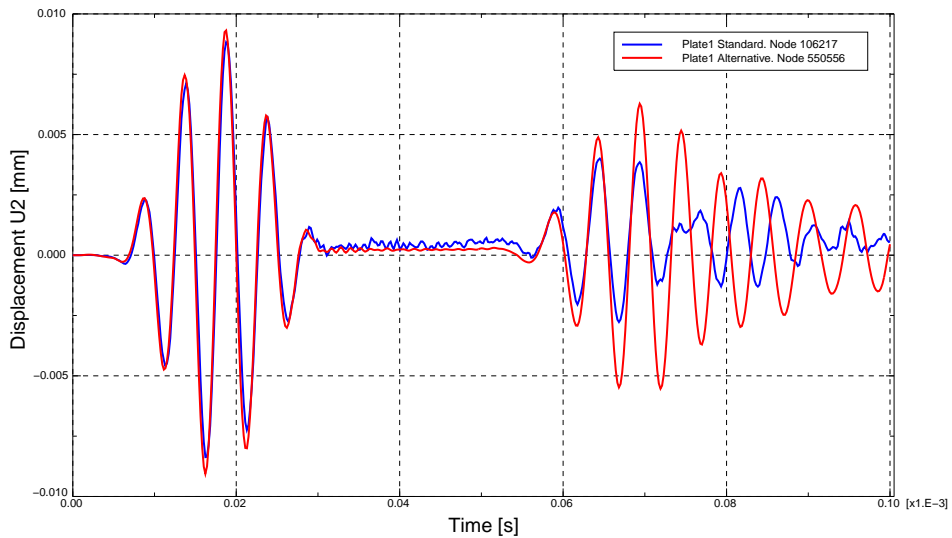


Figure 2.32: Out-of-plane U_2 displacement histories for standard and alternative technique

but is faster than A_0 , and it is reflected numerous times by the boundaries during the simulation time.

The stresses in the elements are calculated in the integration points. Accordingly the stresses in the C3D8R element of the standard model can be

confronted with the stresses of the S4R of the alternative model because their integration points are in the same position, as shown in Fig.2.33. This

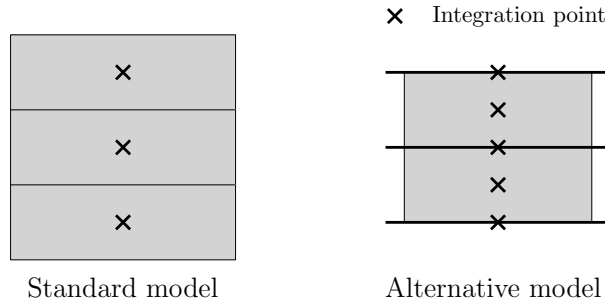


Figure 2.33: Integration points for the standard and alternative technique

confrontation can only be done for the in-plane components of the stress, because the bi-dimensional elements do not have out-of-plane stress components. The σ_{11} histories of the element on the lower surface of the plate is reported in Fig.2.34. The correlation of the two models is perfect until the

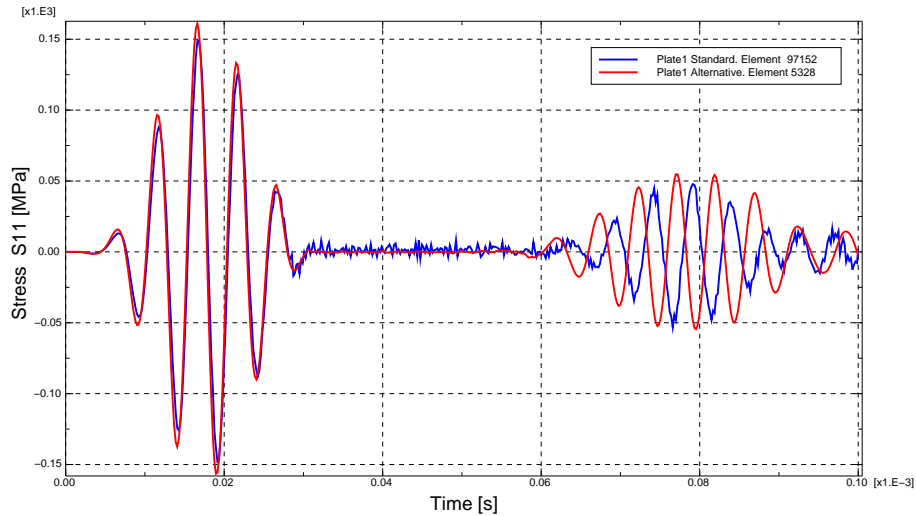


Figure 2.34: σ_{11} stress histories for standard and alternative technique. Lower element

arrival of the reflected wave. The alternative technique is not affected by noise. The histories of σ_{22} component, for the lower element, are represented in Fig.2.35. In this case the correlation is good, until reflection, but the values of the standard model appear more affected by noise than in the previous cases, because the value of the stress is almost of the same order of the level

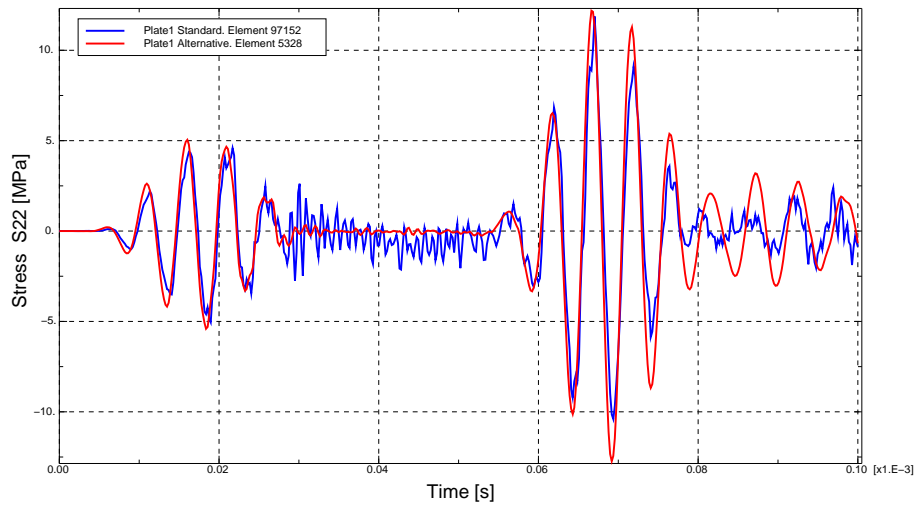


Figure 2.35: σ_{22} stress histories for standard and alternative technique. Lower element

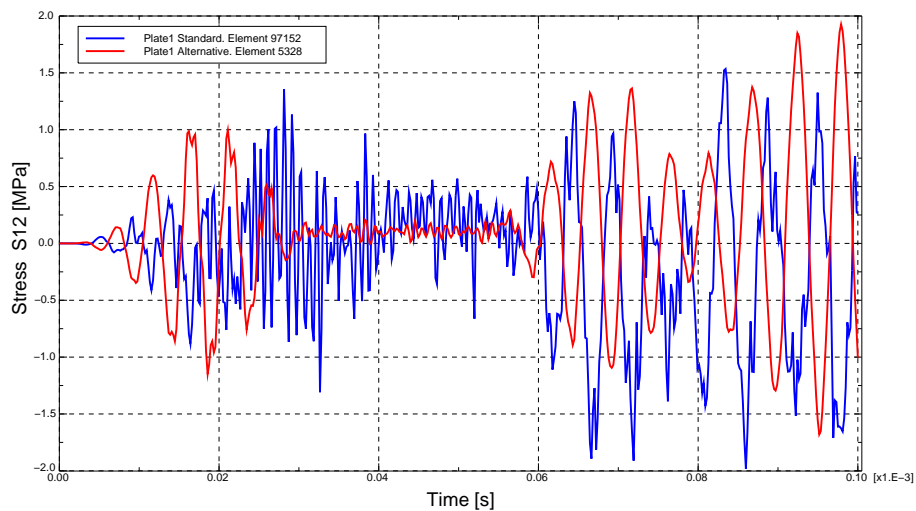


Figure 2.36: σ_{12} stress histories for standard and alternative technique. Lower element

of noise. The shear stress σ_{12} of the lower element is presented in Fig.2.36. In this case the correlation is totally lost because the noise of the measure for the standard model is greater than the its value, even the alternative technique presents noise. But this lack of correlation is not a problem because the values involved are 1/100 the values of σ_{11} .

The confrontation of the two technique shows clearly that the alternative

technique to model composite material achieves the same results of the model done with standard solid elements as far as the effect of A_0 waves are concerned. The main drawback of this approach is the impossibility to represent the symmetric mode S_0 because of the particular characterization of the connection elements.

2.8 The need for model validation

A confrontation between the two modeling technique does not guarantee that the results obtained are physically correct. Although for the isotropic plate some information, namely the velocity and the propagation of the waves, can be achieved from literature, the variability of composite properties and the dependency on the particular material and lamination sequence makes more complicate a validation of the results through literature data. In fact there is no certainty that the FE model represents the correct wavelengths, velocities and shapes of wavefront. A possible strategy for validation can initially rely on a completely different analysis approach. Finally an experimental analysis of the plates can give the true characteristics of the wave propagating in composite plates. The comparison between different numerical techniques and the experiments can provide a reliable validation of the data. The alternative technique to model wave propagation is proposed in chapter 3, whereas the experimental analyses are reported in chapter 4.

Chapter 3

Semi-Analytical Finite Element for the dispersion analysis of composite plates

The need for model validation leads to the application of another approach to model the wave propagation. This approach is the Semi-Analytical Finite Element (SAFE) method, which is also referred to as spectral or waveguide finite element method, which has emerged for modeling the guided wave propagation in 1973 [27]. This method has been progressively improved during the years, as in its first form was able to model just the propagative modes (real wavenumber). Then the method was extended [28] to calculate non-propagating mode, also called evanescent modes (complex wavenumber). These modes do not transport any energy along the structure, but are important from a theoretical viewpoint to satisfy the boundary conditions. More recently, SAFE methods were applied to thin-walled waveguides [29], railroad tracks [30] and wedges [31]. Anisotropic materials were also investigated by means of this method [32–34]. Latest works about SAFE extend the method to account for material damping [35]. In this study, starting from the articles of Lanza di Scalea and Datta [33, 36] a SAFE method is developed to model wave propagation in a infinitely wide laminated plate, though the formulation is applicable to arbitrary cross-section. The original work from [33, 36] has been implemented in a Matlab script in order to obtain the wavenumbers in the wave propagation in composite plate at different excitation frequencies. The first sections describes the original method, the basic aspects of Matlab implementation and the results obtained by applying the numerical tool to the considered composite plates. Finally a confrontation between the FE results and the SAFE results is proposed.

3.1 Overview

A multilayered infinite plate with time-harmonic motion is considered. The plate consists in N parallel, homogeneous or orthotropic layers which are perfectly bonded together. A global rectangular coordinate system (X, Y, Z) is adopted, such that X and Y axes lie in the midplane of the plate and Z axis is parallel to the thickness direction of the plate (see Fig.3.1(a)). The SAFE approach for the extraction of dispersive solutions, uses a finite element discretization of the cross-section of the waveguide, which is considered immersed in vacuum. The displacements along the wave propagation direction are described analytically as harmonic exponential functions. The wave propagates with wavenumber k and frequency ω . The harmonic displacement, stress and strain field components at each point of the waveguide are expressed by Eq.3.1.

$$\mathbf{u} = [u \quad v \quad w]^T \quad (3.1a)$$

$$\boldsymbol{\sigma} = [\sigma_x \quad \sigma_y \quad \sigma_z \quad \sigma_{yz} \quad \sigma_{xz} \quad \sigma_{xy}]^T \quad (3.1b)$$

$$\boldsymbol{\epsilon} = [\epsilon_x \quad \epsilon_y \quad \epsilon_z \quad \epsilon_{yz} \quad \epsilon_{xz} \quad \epsilon_{xy}]^T \quad (3.1c)$$

The constitutive relations at a point are given by Eq.3.2

$$\boldsymbol{\sigma} = \mathbf{C}\boldsymbol{\epsilon} \quad (3.2)$$

where \mathbf{C} is the stiffness matrix of the material. For a wave propagating along a direction oriented at any angle θ with respect to the fiber direction, the SAFE model simply requires the rotation of the stiffness matrix of each lamina through Eq.3.3

$$\mathbf{C}_\theta = \mathbf{R}_1 \mathbf{C} \mathbf{R}_2^{-1} \quad (3.3)$$

where \mathbf{C} is the stiffness matrix in the lamina principal directions and \mathbf{R}_1 and \mathbf{R}_2 are the rotation matrices, which are reported in Eq.3.4 and Eq.3.5.

$$\mathbf{R}_1 = \begin{bmatrix} m^2 & n^2 & 0 & 0 & 0 & 2mn \\ n^2 & m^2 & 0 & 0 & 0 & -2mn \\ 0 & 0 & 1 & 0 & 0 & 0 \\ 0 & 0 & 0 & m & -n & 0 \\ 0 & 0 & 0 & n & m & 0 \\ -mn & mn & 0 & 0 & 0 & m^2 - n^2 \end{bmatrix} \quad (3.4)$$

$$\mathbf{R}_2 = \begin{bmatrix} m^2 & n^2 & 0 & 0 & 0 & mn \\ n^2 & m^2 & 0 & 0 & 0 & -mn \\ 0 & 0 & 1 & 0 & 0 & 0 \\ 0 & 0 & 0 & m & -n & 0 \\ 0 & 0 & 0 & n & m & 0 \\ -2mn & 2mn & 0 & 0 & 0 & m^2 - n^2 \end{bmatrix} \quad (3.5)$$

Equations of motion for the cross-section in [36] are formulated by inserting the kinetic and potential energies into Hamilton's equation. The conservative form of Hamilton's principle is used because, in this work, dissipation is not taken into account. The variation of the Hamiltonian of the waveguide, which vanish at all material points, is Eq.3.6,

$$\delta H = \int_{t_1}^{t_2} \delta(\Phi - K) dt = 0 \quad (3.6)$$

where Φ is the strain energy given by Eq.3.7

$$\Phi = \frac{1}{2} \int_V \boldsymbol{\epsilon}^T \mathbf{C} \boldsymbol{\epsilon} dV \quad (3.7)$$

and K is the kinetic energy given by Eq.3.8,

$$K = \frac{1}{2} \int_V \dot{\mathbf{u}}^T \rho \dot{\mathbf{u}} dV \quad (3.8)$$

where ρ is the material density. By taking the variation of the Hamiltonian and integrating by parts the kinetic energy, equation Eq.3.6 can be written as Eq.3.9.

$$\int_{t_1}^{t_2} \left[\int_V \delta \boldsymbol{\epsilon}^T \mathbf{C} \boldsymbol{\epsilon} dV + \int_V \delta \mathbf{u} \rho \ddot{\mathbf{u}} dV \right] dt = 0 \quad (3.9)$$

3.2 Cross-sectional discretization

The waveguide cross sectional domain Ω can be represented by a system of finite elements with domain Ω_e . Mono- or bi-dimensional elements can be used with this SAFE method, but in this work a mono-dimensional discretization of the cross-section is adopted because the waveguide is an infinitely wide plate. To discretize Ω a Matlab routine is created to divide the thickness of the plate into a number of elements, as can be seen in Fig.3.1(a). The adopted element has three nodes and its degree of freedom are represented in Fig.3.1(b). The local coordinate system axes (x,y,z) are parallel to the global coordinate axes. Each ply is modeled by two elements. Actually a

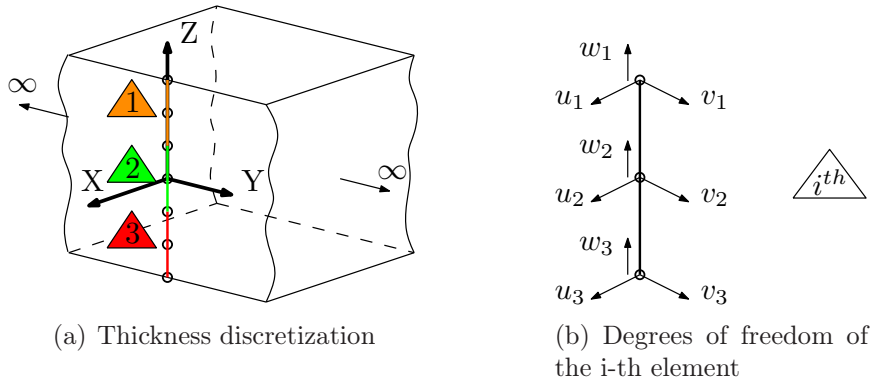


Figure 3.1: SAFE discretization of an infinitely wide plate using mono-dimensional three-node elements. In the triangle there is the ID of the element

two-element discretization can be considered adequate for a whole isotropic plate, because such a refinement corresponds to 5 nodes through the thickness, which can quite adequately represent the first mode shapes. If more precision, or higher modes, are needed, it is enough to increase the number of plies per layer, by assigning the same property and the same orientation.

3.3 Modeling and shape functions

The cross-section is modeled by a finite element discretization, by using a given set of shape functions. As the elements adopted have three nodes, the isoparametric shape functions are quadratic and are represented in Fig.3.2. The expressions of these function are reported in Eq.3.10,

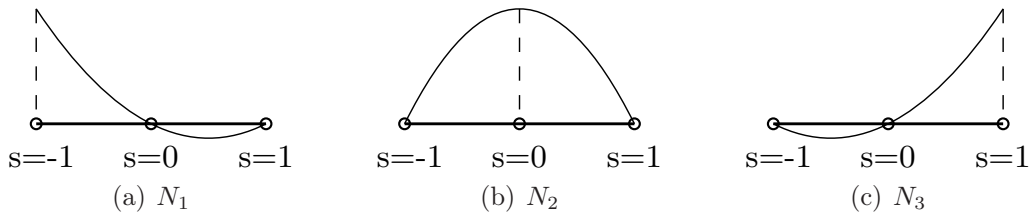


Figure 3.2: Shape function for the quadratic mono-dimensional elements.

$$N_1 = \frac{1}{2}(1 - s) - \frac{1}{2}(1 - s^2) \quad (3.10a)$$

$$N_2 = 1 - s^2 \quad (3.10b)$$

$$N_3 = \frac{1}{2}(1 + s) - \frac{1}{2}(1 - s^2) \quad (3.10c)$$

where s is the adimensional coordinate. If these functions are organized into vector as in Eq.3.11,

$$\mathbf{N} = [N_1 \quad N_2 \quad N_3]^T \quad (3.11)$$

then the matrices, which are reported in Eq.3.12 can be defined.

$$\mathbf{E}_1 = \begin{bmatrix} \mathbf{N} & \cdot & \cdot \\ \cdot & \cdot & \cdot \\ \cdot & \cdot & \cdot \\ \cdot & \cdot & \cdot \\ \cdot & \cdot & \mathbf{N} \\ \cdot & \mathbf{N} & \cdot \end{bmatrix} \quad \mathbf{E}_2 = \begin{bmatrix} \cdot & \cdot & \cdot \\ \cdot & \mathbf{N} & \cdot \\ \cdot & \cdot & \cdot \\ \cdot & \cdot & \mathbf{N} \\ \cdot & \cdot & \cdot \\ \mathbf{N} & \cdot & \cdot \end{bmatrix} \quad (3.12)$$

$$\mathbf{E}_3 = \begin{bmatrix} \cdot & \cdot & \cdot \\ \cdot & \cdot & \cdot \\ \cdot & \cdot & \mathbf{N}/z \\ \cdot & \mathbf{N}/z & \cdot \\ \mathbf{N}/z & \cdot & \cdot \\ \cdot & \cdot & \cdot \end{bmatrix} \quad \mathbf{N}_n = \begin{bmatrix} \mathbf{N} & \cdot & \cdot \\ \cdot & \mathbf{N} & \cdot \\ \cdot & \cdot & \mathbf{N} \end{bmatrix}$$

The displacement at a point within an element is given by Eq.3.13,

$$\mathbf{u}(x, y, z, t) = \mathbf{N}(z)\mathbf{u}_e(x, y, t) \quad (3.13)$$

where \mathbf{u}_e is a column vector (Eq.3.14) containing the displacements at the three nodes of the element.

$$\mathbf{u}_e = [u_1 \quad u_2 \quad u_3 \quad v_1 \quad v_2 \quad v_3 \quad w_1 \quad w_2 \quad w_3]^T \quad (3.14)$$

The strain tensor in the element can be represented as function of nodal displacements as in Eq.3.15.

$$\boldsymbol{\epsilon}^{(e)} = \mathbf{E}_1\mathbf{u}_{e/x} + \mathbf{E}_2\mathbf{u}_{e/y} + \mathbf{E}_3\mathbf{u}_e \quad (3.15)$$

Now substituting Eq.3.14 and Eq.3.15 into the variational form, which is

represented in Eq.3.9, yields to the Eq.3.16,

$$\begin{aligned}
 \int_{t_1}^{t_2} \left[\int_y \int_x \left(+ \delta \mathbf{u}_{e/x}^T \mathbf{k}_{11}^{(e)} \mathbf{u}_{e/x} + \delta \mathbf{u}_{e/x}^T \mathbf{k}_{12}^{(e)} \mathbf{u}_{e/y} + \delta \mathbf{u}_{e/x}^T \mathbf{k}_{13}^{(e)} \mathbf{u}_e \right. \right. \\
 + \delta \mathbf{u}_{e/y}^T \mathbf{k}_{21}^{(e)} \mathbf{u}_{e/x} + \delta \mathbf{u}_{e/y}^T \mathbf{k}_{22}^{(e)} \mathbf{u}_{e/y} + \delta \mathbf{u}_{e/y}^T \mathbf{k}_{23}^{(e)} \mathbf{u}_e \\
 + \delta \mathbf{u}_e^T \mathbf{k}_{31}^{(e)} \mathbf{u}_{e/x} + \delta \mathbf{u}_e^T \mathbf{k}_{32}^{(e)} \mathbf{u}_{e/y} + \delta \mathbf{u}_e^T \mathbf{k}_{33}^{(e)} \mathbf{u}_e \\
 \left. \left. + \delta \mathbf{u}_e^T \mathbf{m}^{(e)} \ddot{\mathbf{u}}_e \right) dx dy \right] dt = 0
 \end{aligned} \tag{3.16}$$

where the mass and stiffness matrices are reported in Eq.3.17.

$$\begin{aligned}
 \mathbf{k}_{11}^{(e)} &= \int_{-h}^h \mathbf{E}_1^T \mathbf{C} \mathbf{E}_1 dz & \mathbf{k}_{22}^{(e)} &= \int_{-h}^h \mathbf{E}_2^T \mathbf{C} \mathbf{E}_2 dz \\
 \mathbf{k}_{33}^{(e)} &= \int_{-h}^h \mathbf{E}_3^T \mathbf{C} \mathbf{E}_3 dz & \mathbf{k}_{12}^{(e)} &= \mathbf{k}_{21}^{(e)T} = \int_{-h}^h \mathbf{E}_1^T \mathbf{C} \mathbf{E}_2 dz \\
 \mathbf{k}_{13}^{(e)} &= \mathbf{k}_{31}^{(e)T} = \int_{-h}^h \mathbf{E}_1^T \mathbf{C} \mathbf{E}_3 dz & \mathbf{k}_{23}^{(e)} &= \mathbf{k}_{32}^{(e)T} = \int_{-h}^h \mathbf{E}_2^T \mathbf{C} \mathbf{E}_3 dz \\
 \mathbf{m}^{(e)} &= \int_{-h}^h \rho \mathbf{N}_n^T \mathbf{N} dz
 \end{aligned} \tag{3.17}$$

For the following passages is advisable to use a displacements vector of the form Eq.3.18.

$$\mathbf{u}_e = [u_1 \quad v_1 \quad w_1 \quad u_2 \quad v_2 \quad w_2 \quad u_3 \quad v_3 \quad w_3]^T \tag{3.18}$$

Indicating by n_{el} the total number of cross-sectional elements, a standard fi-

nite elements assembling procedures can be employed, as expressed in Eq.3.19,

$$\begin{aligned}
 \mathbf{K}_{11} &= \bigcup_{e=1}^{n_{el}} \mathbf{k}_{11}^{(e)} & \mathbf{K}_{12} &= \bigcup_{e=1}^{n_{el}} \mathbf{k}_{12}^{(e)} & \mathbf{K}_{13} &= \bigcup_{e=1}^{n_{el}} \mathbf{k}_{13}^{(e)} \\
 \mathbf{K}_{21} &= \bigcup_{e=1}^{n_{el}} \mathbf{k}_{21}^{(e)} & \mathbf{K}_{22} &= \bigcup_{e=1}^{n_{el}} \mathbf{k}_{22}^{(e)} & \mathbf{K}_{23} &= \bigcup_{e=1}^{n_{el}} \mathbf{k}_{23}^{(e)} \\
 \mathbf{K}_{31} &= \bigcup_{e=1}^{n_{el}} \mathbf{k}_{31}^{(e)} & \mathbf{K}_{32} &= \bigcup_{e=1}^{n_{el}} \mathbf{k}_{32}^{(e)} & \mathbf{K}_{33} &= \bigcup_{e=1}^{n_{el}} \mathbf{k}_{33}^{(e)} \\
 \mathbf{M} &= \bigcup_{e=1}^{n_{el}} \mathbf{m}^{(e)} & \mathbf{U} &= \bigcup_{e=1}^{n_{el}} \mathbf{u}_e
 \end{aligned} \tag{3.19}$$

where \mathbf{U} is the column vector of assembled nodal displacements \mathbf{u}_e . The resulting equations of motion with global matrices, due to the arbitrariness of $\delta\mathbf{U}$ is the Eq.3.20.

$$\begin{aligned}
 &\mathbf{K}_{11}\mathbf{U}_{/XX} + \mathbf{K}_{22}\mathbf{U}_{/YY} + (\mathbf{K}_{12} + \mathbf{K}_{21})\mathbf{U}_{/XY} + (\mathbf{K}_{13} - \mathbf{K}_{31})\mathbf{U}_{/X} \\
 &+ (\mathbf{K}_{23} - \mathbf{K}_{32})\mathbf{U}_{/Y} + \mathbf{K}_{33}\mathbf{U} - \mathbf{M}\ddot{\mathbf{U}} = 0
 \end{aligned} \tag{3.20}$$

For a wave propagating in the X-Y plane is more comfortable working with the Fourier transform (Eq.3.21) of the displacements vector $\mathbf{U}(X, Y, t)$,

$$\hat{\mathbf{U}}(k_x, k_y, \omega) = \int_{-\infty}^{\infty} \int_{-\infty}^{\infty} \int_{-\infty}^{\infty} \mathbf{U}(X, Y, t) e^{i(k_x X + k_y Y - \omega t)} dX dY dt \tag{3.21}$$

where k_x and k_y are the wavenumbers in the X and Y directions respectively and ω represent the circular frequency. Applying the Fourier transform Eq.3.21 to Eq.3.20 leads to the Eq.3.22.

$$\begin{aligned}
 &\left[k_x^2 \mathbf{K}_{11} + k_y^2 \mathbf{K}_{22} + k_x k_y (\mathbf{K}_{12} + \mathbf{K}_{21}) + i k_x (\mathbf{K}_{13} - \mathbf{K}_{31}) \right. \\
 &\left. + i k_y (\mathbf{K}_{23} - \mathbf{K}_{32}) + \mathbf{K}_{33} - \omega^2 \mathbf{M} \right] \hat{\mathbf{U}} = 0
 \end{aligned} \tag{3.22}$$

For a wave propagating in an arbitrary direction in the X-Y plane, which is characterized by an angle θ with the X axis, the relation expressed in Eq.3.23

can be considered,

$$k_x = k \cos \theta \quad (3.23a)$$

$$k_y = k \sin \theta \quad (3.23b)$$

where k is the wavenumber in the direction of the propagating wave. The Eq.3.23 leads to the Eq.3.24

$$\mathbf{K}_1 = \mathbf{K}_{11} \cos^2 \theta + \mathbf{K}_{22} \sin^2 \theta + (\mathbf{K}_{12} + \mathbf{K}_{21}) \cos \theta \sin \theta \quad (3.24a)$$

$$\mathbf{K}_2 = (\mathbf{K}_{13} - \mathbf{K}_{31}) \cos \theta + (\mathbf{K}_{23} - \mathbf{K}_{32}) \sin \theta \quad (3.24b)$$

$$\mathbf{K}_3 = \mathbf{K}_{33} \quad (3.24c)$$

The stiffness matrices \mathbf{K}_1 and \mathbf{K}_3 are symmetric, while matrix \mathbf{K}_2 is skew symmetric. The mass matrix \mathbf{M} is real, symmetric and positive definite. Matrix \mathbf{K}_1 models the out-of-plane deformation behavior, whereas matrix \mathbf{K}_3 is related to the planar deformations, so it describes the generalized plane strain behavior or cross-sectional warpage. Finally, using the relations Eq.3.24, the Eq.3.22 can be rewritten as Eq.3.25

$$\left[k^2 \mathbf{K}_1 + ik \mathbf{K}_2 + \mathbf{K}_3 - \omega^2 \mathbf{M} \right] \hat{\mathbf{U}} = 0 \quad (3.25)$$

Solving the Eq.3.25 will determinate the dispersion relation for guided waves in infinite plates.

3.4 Solution

To eliminate the imaginary unit in Eq.3.25 a transformation \mathbf{T} is introduced. The elements of \mathbf{T} corresponding to the displacements along X and Y directions are equal to 1, while those along Z direction are equal to the imaginary unit, as it can be seen in Eq.3.26.

$$\mathbf{T} = \begin{bmatrix} 1 & & & & & & \\ & 1 & & & & & \\ & & i & & & & \\ & & & \ddots & & & \\ & & & & 1 & & \\ & & & & & 1 & \\ & & & & & & i \end{bmatrix} \quad (3.26)$$

This matrix has the properties reported in Eq.3.27,

$$\mathbf{T}^T = \mathbf{T}^* \quad (3.27a)$$

$$\mathbf{T}^* \mathbf{T} = \mathbf{T} \mathbf{T}^* = \mathbf{I} \quad (3.27b)$$

where \mathbf{T}^* is the complex conjugate of \mathbf{T} . If the terms of Eq.3.25 are pre-multiplied by \mathbf{T}^T and post-multiplied by \mathbf{T} , the matrices \mathbf{K}_1 , \mathbf{K}_3 and \mathbf{M} will not be altered (Eq.3.28) since they do not mix displacements along Z with displacements along X or Y .

$$\mathbf{T}^T \mathbf{K}_1 \mathbf{T} = \mathbf{K}_1 \quad \mathbf{T}^T \mathbf{K}_3 \mathbf{T} = \mathbf{K}_3 \quad \mathbf{T}^T \mathbf{M} \mathbf{T} = \mathbf{M} \quad (3.28)$$

The matrix \mathbf{K}_2 , instead, mixes the displacements along Z with the ones along X and Y but it does not mix the displacements along X and Y with each other, so it follows the Eq.3.29,

$$\mathbf{T}^T \mathbf{K}_2 \mathbf{T} = -i \hat{\mathbf{K}}_2 \quad (3.29)$$

where $\hat{\mathbf{K}}_2$ is a symmetric matrix. The final form of the eigenvalue problem is the Eq.3.30.

$$\left[k^2 \mathbf{K}_1 + k \hat{\mathbf{K}}_2 + \mathbf{K}_3 - \omega^2 \mathbf{M} \right] \hat{\mathbf{U}} = 0 \quad (3.30)$$

Nontrivial solutions can be found by solving a twin-parameters generalized eigenproblem in k and ω . The frequency ω is a real and positive quantity, whereas the wavenumber k can be real or complex and can have either positive and negative signs. For lossless materials, as the ones investigated in this work, the stiffness matrix \mathbf{C} is real, so the use of the operator \mathbf{T} simplifies Eq.3.30 to a real and symmetric system. Thus, by assigning real values to k , the Eq.3.30 can be solved as a standard eigenvalue problem in $\omega(k)$ and the solutions for this case correspond to propagative waves. So if the dimension of the problem is n_{DOF} , for each wavenumber k_i there are n_{DOF} propagating modes (k_i, ω_i) and n_{DOF} $\hat{\mathbf{U}}_i$ cross-sectional mode shape, which are also called wavestructure.

The resolution of the Eq.3.30 for a given frequency ω is necessary for the study of the full complex spectrum for both propagative and evanescent modes, but in this work it is used for computing the polar plot of the wavenumber, which is the representation of how the wave propagates along the different directions of a composite plate. To obtain the unknown wavenumbers $k(\omega)$ the Eq.3.30 must be solved as a second-order polynomial eigenvalue problem. A classical technique to solve this kind of problems consists of recasting the Eq.3.30 to a first-order eigensystem by doubling its size

as in Eq.3.31,

$$[\mathbf{A} - k\mathbf{B}]\mathbf{Q} = 0 \quad (3.31)$$

where the matrices A , B and the vector Q are defined in Eq.3.32.

$$\mathbf{A} = \begin{bmatrix} 0 & \mathbf{K}_3 - \omega^2\mathbf{M} \\ \mathbf{K}_3 - \omega^2\mathbf{M} & \hat{\mathbf{K}}_2 \end{bmatrix}, \quad \mathbf{B} = \begin{bmatrix} \mathbf{K}_3 - \omega^2\mathbf{M} & 0 \\ 0 & -\mathbf{K}_1 \end{bmatrix}, \quad (3.32a)$$

$$\mathbf{Q} = \begin{Bmatrix} \hat{\mathbf{U}} \\ k\hat{\mathbf{U}} \end{Bmatrix} \quad (3.32b)$$

\mathbf{A} and \mathbf{B} are real symmetric matrices. Solving the Eq.3.31 at each frequency ω , $2n_{DOF}$ eigenvalues k_i and $2n_{DOF}$ eigenvectors are obtained. In this work the wavenumbers of interest are those with just the real part, that occur as pairs of real numbers ($\pm k_{Re}$), representing the propagative waves in the $\pm X$ directions. The phase velocity can then be evaluated by $c_{ph} = \omega/k_{Re}$.

Recently it has been proposed a technique [37] for computing the group velocity $c_g = \partial\omega/\partial k$ for undamped waveguides, which is worth of noting. The conventional approach uses the differences of the values for adjacent points of the same mode, so that the accuracy of the c_g is sensitive to that of the (k, ω) solutions. Moreover, the tracking of the modes is not straightforward when one mode approaches another. The method that is proposed in [37] adopted calculates the c_g directly at each (k, ω) solution point without any contribution from adjacent points. The procedure starts by evaluating the derivative of Eq.3.30 with respect to the wavenumber, as it can be seen in Eq.3.33,

$$\frac{\partial}{\partial k} \left([\mathbf{K}(k) - \omega^2\mathbf{M}] \hat{\mathbf{U}}_R \right) = 0 \quad (3.33)$$

where $\mathbf{K}(k)$ is given by Eq.3.34

$$\mathbf{K}(k) = k^2\mathbf{K}_1 + k\hat{\mathbf{K}}_2 + \mathbf{K}_3 \quad (3.34)$$

and the $\hat{\mathbf{U}}_R$ represents the right eigenvector. Pre-multiplying the Eq.3.33 by the transpose of the left eigenvector $\hat{\mathbf{U}}_L$ gives the Eq.3.35

$$\hat{\mathbf{U}}_L^T \left[\frac{\partial}{\partial k} \mathbf{K}(k) - 2\omega \frac{\partial \omega}{\partial k} \mathbf{M} \right] \hat{\mathbf{U}}_R = 0 \quad (3.35)$$

Since $\partial\omega/\partial k$ is a scalar, the group velocity is given by Eq.3.36.

$$c_g = \frac{\partial \omega}{\partial k} = \frac{\hat{\mathbf{U}}_L (\mathbf{K}_2 + 2k\mathbf{K}_1) \hat{\mathbf{U}}_R}{2\omega \hat{\mathbf{U}}_L^T \mathbf{M} \hat{\mathbf{U}}_R} \quad (3.36)$$

With this relation the group velocity can be evaluated for each individual solution (k, ω) of the dispersion relations at a time independently of any adjacent solution. The group velocity definition is not possible in damped waveguides because the wavenumbers become complex and the differentiation $c_g = \partial\omega/\partial k$ is no longer possible. In such a case the energy velocity V_e is used, but this property is not taken into account in this work.

3.5 Implementation and examples

A MATLAB code is developed to apply the SAFE method to plates made with both isotropic and orthotropic layers. Each plate consists of N layers, stacked along the Z direction and for each layer information are provided about its thickness, orientation and characteristics of the material. The thickness of the plate is calculated by summing the thicknesses of all layers. For isotropic plates even a single layer, with the thickness of the whole plate, can be used, but, in order to increase the definition in modeling the mode shapes, the plate can be divided in more layers with the same orientation, thickness and material. The orientation of the layers is only important for orthotropic materials. The orientation is given as an angle θ between the orientation of the fibres of that layer and the X direction. The characteristics of the material are given as Young's moduli E_x, E_y, E_z , shear moduli G_{xy}, G_{xz}, G_{yz} and Poisson's ratios $\nu_{xy}, \nu_{xz}, \nu_{yz}$. The Poisson's ratios are related by the Eq.3.37.

$$\frac{\nu_{ij}}{E_i} = \frac{\nu_{ji}}{E_j} \quad (3.37)$$

The stiffness matrix of the element is given by Eq.3.38,

$$C = \begin{bmatrix} \frac{1-\nu_{yz}\nu_{zy}}{E_y E_z \Delta} & \frac{\nu_{yx}+\nu_{zx}\nu_{yz}}{E_y E_z \Delta} & \frac{\nu_{zx}+\nu_{yx}\nu_{zy}}{E_y E_z \Delta} & 0 & 0 & 0 \\ \frac{\nu_{xy}+\nu_{xz}\nu_{zy}}{E_x E_z \Delta} & \frac{1-\nu_{zx}\nu_{xz}}{E_x E_z \Delta} & \frac{\nu_{zy}+\nu_{zx}\nu_{xy}}{E_x E_z \Delta} & 0 & 0 & 0 \\ \frac{\nu_{xz}+\nu_{xy}\nu_{yz}}{E_x E_y \Delta} & \frac{\nu_{yz}+\nu_{xz}\nu_{yx}}{E_x E_y \Delta} & \frac{1-\nu_{xy}\nu_{yx}}{E_x E_y \Delta} & 0 & 0 & 0 \\ 0 & 0 & 0 & 2G_{yz} & 0 & 0 \\ 0 & 0 & 0 & 0 & 2G_{xz} & 0 \\ 0 & 0 & 0 & 0 & 0 & 2G_{xy} \end{bmatrix} \quad (3.38)$$

where Δ is given by Eq.3.39.

$$\Delta = \frac{1 - \nu_{xy}\nu_{yx} - \nu_{yz}\nu_{zy} - \nu_{zx}\nu_{xz} - 2\nu_{xy}\nu_{yz}\nu_{zx}}{E_x E_y E_z} \quad (3.39)$$

For each orthotropic layer, with an orientation different from 0° , the stiffness matrix \mathbf{C} must be rotated through the Eq.3.3.

Now the dispersion curves are presented and the polar plots for the same plates are analyzed using the finite element method. For each plate the course of the wavenumber, phase velocity and group velocity versus the frequency are reported. Moreover, a polar plot is produced, which represents the wavenumber and the phase velocity of the wave for different orientation of propagation.

Isotropic aluminum plate The dispersion curves for the aluminum plate, whose finite element model has been presented in section 2.3, are reported in Fig.3.3. As expected for an isotropic material the wave propagates in all directions in the same way, as it can be seen looking at the polar plots in Fig.3.3(f) and Fig.3.3(e). These plots are perfectly circular, that means that the wavenumber, and consequently the phase velocity, of the propagating wave is the same for each direction θ .

Unidirectional fiber glass plate In composite plates the waves propagate with different wavenumber, phase and group velocity for each direction θ . The wavenumber and phase velocity dispersion curves of the unidirectional $[0^\circ]$ fiber glass plate are presented in Fig.3.4 for three different values of θ (0° , 45° , 90°). For a given frequency the polar plot shows better how the wave number and the phase velocity change with the angle θ . In these plots for each angle θ there are three points representing the wavenumbers, in Fig.3.5(a), or the phase velocities, in Fig.3.5(b), of the symmetric S_0 , antisymmetric A_0 and the shear SH_0 modes. For each lamination sequence, which includes material, orientation and thickness of the plies in the plates, there exist just one polar plot for a given frequency. The polar plot univocally characterize the plate. Looking at Fig.3.5(b) it can be noted that the phase velocity of both A_0 and S_0 Lamb waves is the highest along $\theta = 0^\circ$ direction, which is the direction of the plate fiber, whereas along the $\theta = 90^\circ$ direction the speed is the lowest. This is an expected result because along the fiber the stiffness of the plate is higher, as well the velocity of the wave. The shear mode SH_0 presents a different behavior, it has the same minimum velocity for $\theta = 0^\circ$ and $\theta = 90^\circ$, whereas the highest one is around $\theta = 60^\circ$. The group velocity also change with θ (Fig.3.6), but the polar plot of this quantity is not considered.

$[0_2^\circ 90_2^\circ]_s$ **fiber glass plate** The wavenumber, phase and group velocity dispersion curves for the $[0_2^\circ 90_2^\circ]_s$ fiber glass plate are reported in Fig.3.7

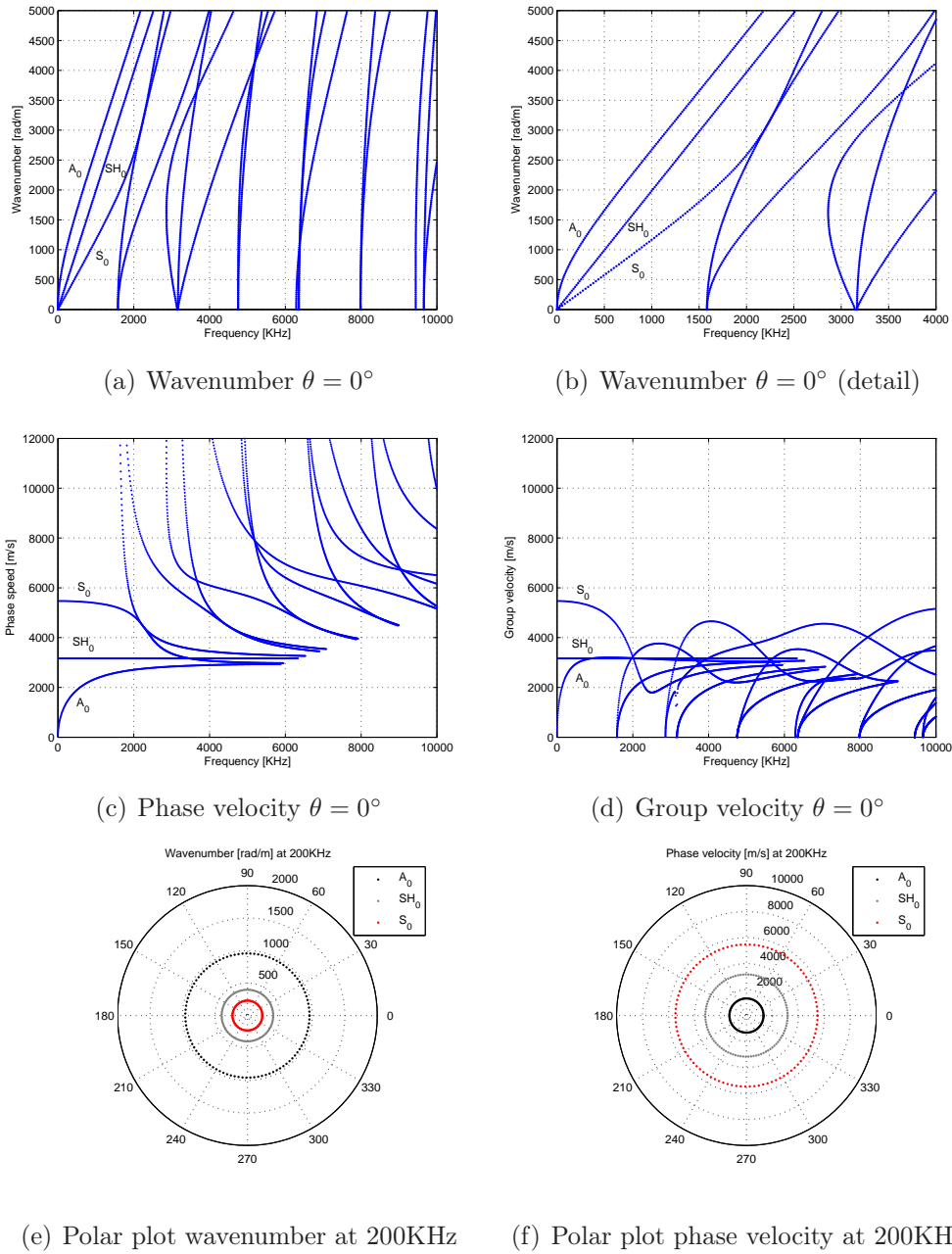
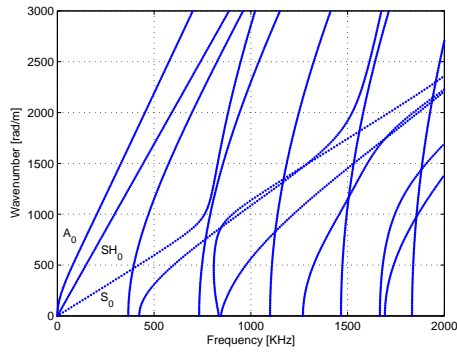
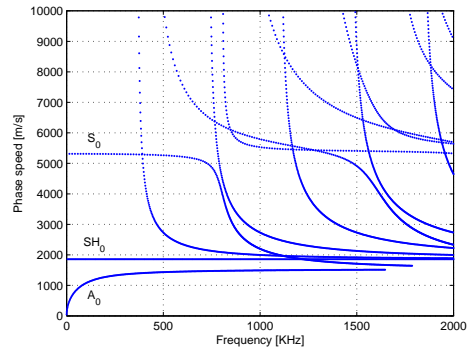


Figure 3.3: Wavenumber, phase and group velocity dispersion curves of the isotropic, 1mm thick, aluminum plate

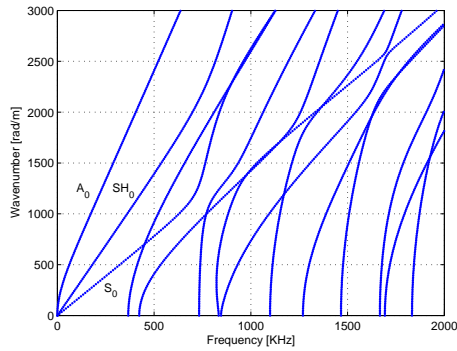
only for $\theta = 0^\circ$, because the interest in this work is mainly focused on the polar plots. The Polar plots, which univocally characterize the considered laminate, are reported in Fig.3.8. The polar plot of the phase velocity in



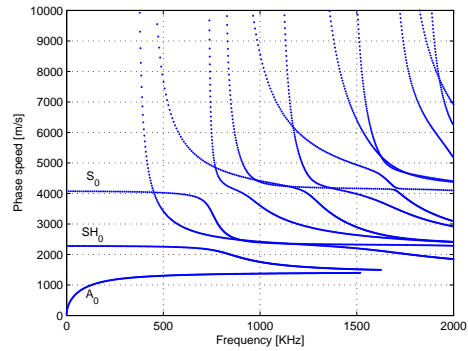
(a) Wavenumber $\theta = 0^\circ$



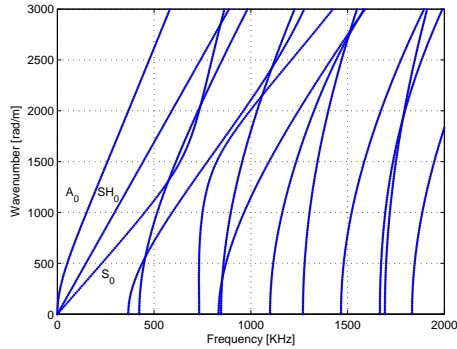
(b) Phase velocity $\theta = 0^\circ$



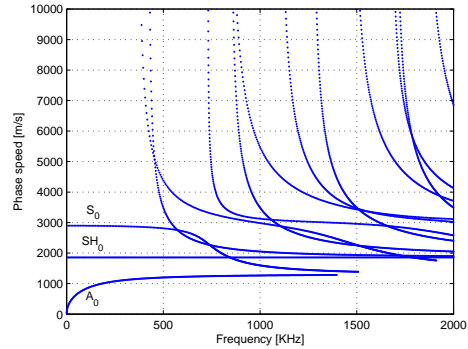
(c) Wavenumber $\theta = 45^\circ$



(d) Phase velocity $\theta = 45^\circ$



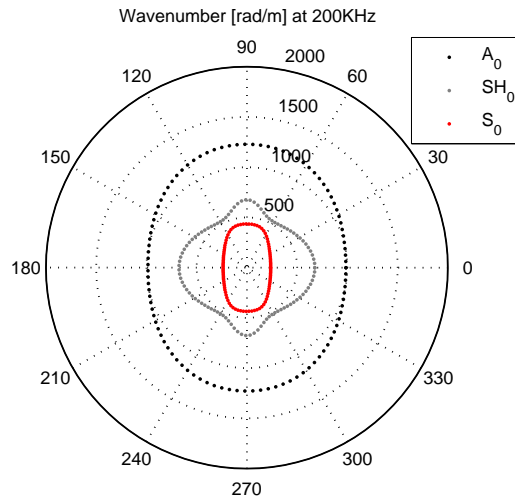
(e) Wavenumber $\theta = 90^\circ$



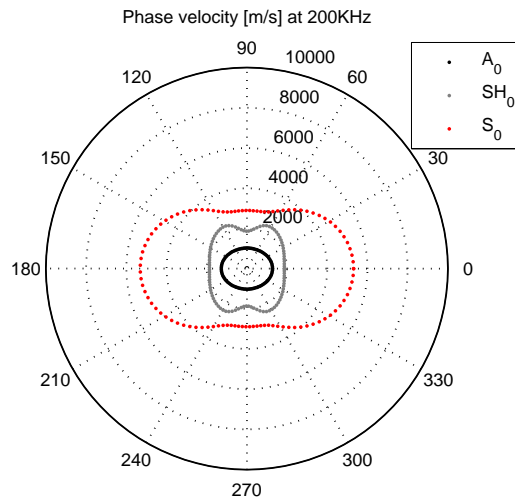
(f) Phase velocity $\theta = 90^\circ$

Figure 3.4: Wavenumber and phase velocity dispersion curves of the unidirectional $[0_8]$ fibre glass plate at different angle θ

Fig.3.8(b) shows that the the symmetric mode S_0 has almost the same velocity for each direction with maximum both at $\theta = 0^\circ$ and $\theta = 90^\circ$ and minimum at $\theta = 45^\circ$. This behavior can be explained by the use of an equal



(a) Polar plot wavenumber at 200KHz



(b) Polar plot phase velocity at 200KHz

Figure 3.5: Wavenumber and phase velocity polar plots of the unidirectional $[0^\circ]$ fiber glass plate

number of plies at 0° and 90° orientation and by considering the mode of propagation, that involves mostly the in-plane displacements along the wave propagation direction. Since along the directions of the fibers the stiffness is higher, the phase velocity of the S_0 mode is higher too and since the cross-

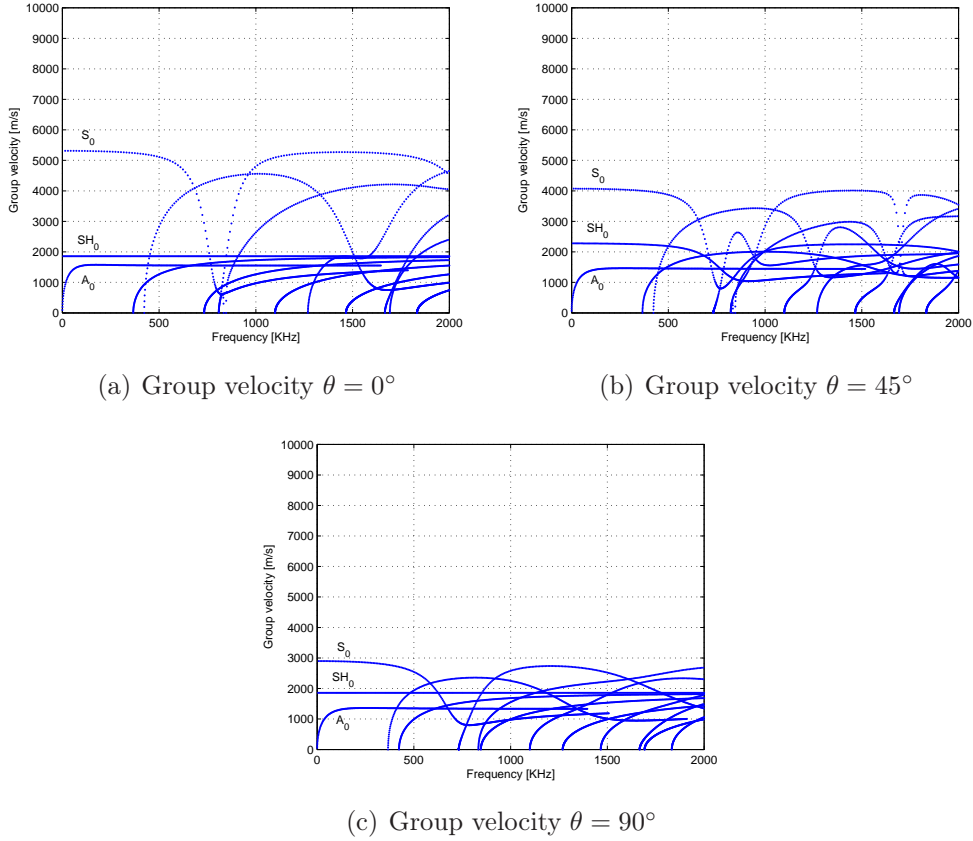


Figure 3.6: Group velocity dispersion curves of the unidirectional $[0_8]$ fiber glass plate at different angle θ

section area is half covered by $\theta = 0^\circ$ fibers and half by $\theta = 90^\circ$ fibers, the phase velocity along those directions is the same. On the other hand the polar plot of the phase velocity of the antisymmetric mode A_0 presents an elliptical shape with a maximum along $\theta = 0^\circ$, even though the difference with the minimum velocity is not as relevant as the one in the unidirectional case. This is due to the fact that the A_0 mode is flexural and the external fibers of the plate are oriented along the 0° direction, so their flexural stiffness is higher than the one along the 90° direction and the wave propagates faster along $\theta = 0^\circ$. Finally the shear mode SH_0 presents peaks of velocity for $\theta = 45^\circ$.

Quasi-isotropic carbon fiber plate The wavenumber, phase and group velocity dispersion curves for the $[0^\circ 45^\circ 90^\circ -45^\circ]_2s$ carbon fiber plate are reported in Fig.3.9 for just $\theta = 0^\circ$. The wavenumber and phase velocity polar

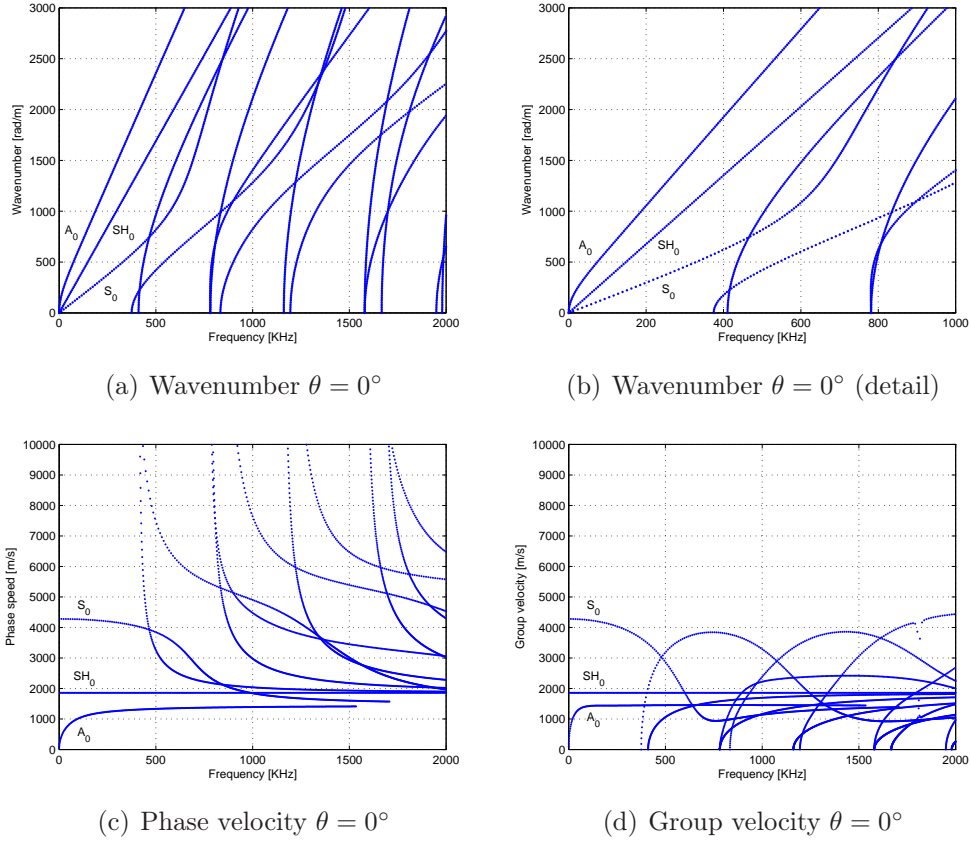
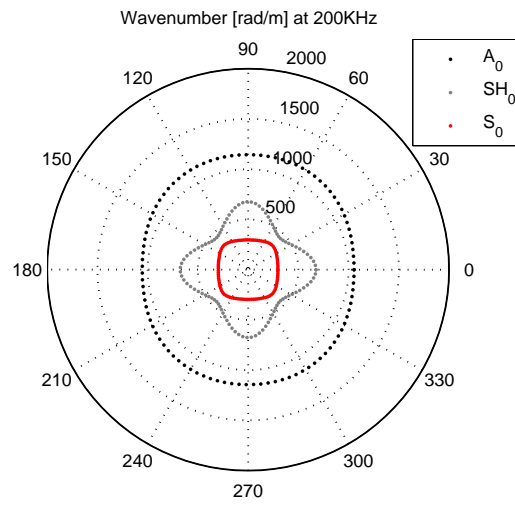
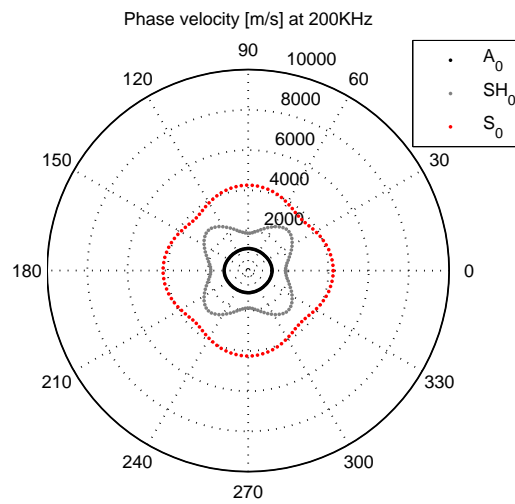


Figure 3.7: Wavenumber, phase and group velocity dispersion curves of the $[0_2^o 90_2^o]_s$ fiber glass plate

plots, reported in Fig.3.10, are almost circular indicating that both the Lamb waves A_0 and S_0 and the shear wave SH_0 have almost the same behavior for all the directions. The quasi-isotropic sequence provides identical membranal stiffness in all the directions. Anyway, flexural stiffness are not identical, because they depend on the position of the layers through the thickness. Propagation directions of A_0 waves are influenced more by the orientation of the external layers than by the internal ones. This behavior is emphasized by the number of plies, sixteen, that is double with respect to the other two composite plates. In the wavenumber polar plot of Fig.3.10(a) the A_0 mode is the one that changes more with the angle of propagation, even though the variation in wavenumber is minimal. The shapes that depicts is a sort of ellipse with the major axis aligned along the direction at about -60° . Consequently this mode, on the phase velocity polar plot Fig.3.10(b), has the major axis along the 30° direction, even if is not visible as in the wavenumber



(a) Polar plot wavenumber at 200KHz



(b) Polar plot phase velocity at 200KHz

Figure 3.8: Wavenumber and phase velocity polar plots of the $[0_2^o 90_2^o]_s$ fiber glass plate

polar plot.

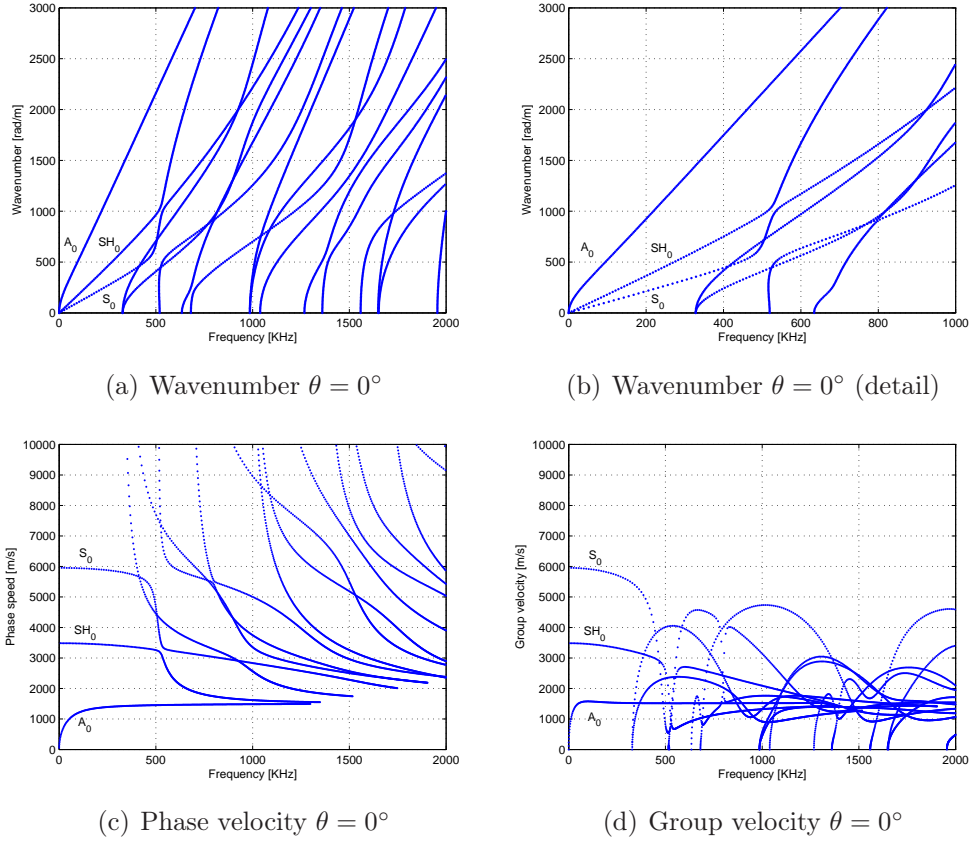
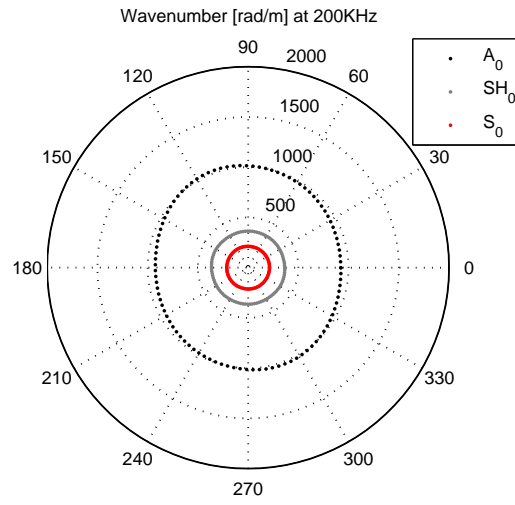


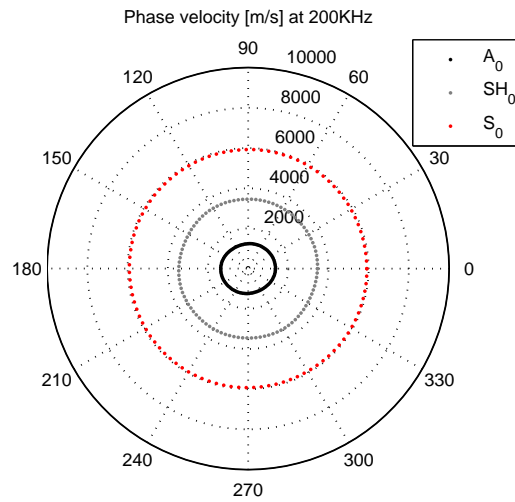
Figure 3.9: Wavenumber, phase and group velocity dispersion curves of the $[0^\circ 45^\circ 90^\circ - 45^\circ]_2s$ carbon fiber plate

3.6 Validation through spatial Fourier Analysis

There is now the need for a comparison between the results achieved by the FE analyses and the ones obtained from the SAFE approach. The FE method returns the displacements of the model nodes for each time step, whereas the SAFE method returns, among others quantities, the wavenumbers of the Lamb waves for each direction of propagation. For this reason it is required a technique to pass from one kind of data to the other. This is possible thanks to the Fourier transform that allows a transformation from the space domain to the wavenumber domain. Usually Fourier transform is used to pass from the time domain to the frequency domain, but it can be used in space as well. If displacement histories of more than one point are considered it is possible to extract, from those signals, the frequency content and the wavenumber content which is the spatial frequency, i.e. the number



(a) Polar plot wavenumber at 200KHz



(b) Polar plot phase velocity at 200KHz

Figure 3.10: Wavenumber and phase velocity polar plots of the $[0^\circ 45^\circ 90^\circ - 45^\circ]_2s$ carbon fiber plate

of waves in the unit length. In this section it is explained how the Fourier transform (FT) is used to generate homogeneous data to compare the two techniques and then a confrontation between the SAFE approach and the FE one is presented.

3.6.1 Fourier transform

The purpose of this sub-section is not the rigorous mathematical explanation of the Fourier transform, that can be found in every analysis book [38], but the practical use of this tool to achieve the desired results. The expression of the FT in its most general form is Eq.3.40,

$$F(\xi) = \int_{-\infty}^{+\infty} f(x)e^{-j2\pi\xi x} dx \quad (3.40)$$

where x is the independent variable and ξ is the transform variable. However working with discrete signal, i.e. a sampled continuous signal of finite duration, requires the use of the Discrete Fourier Transform (DFT), which is described by Eq.3.41.

$$F(p) = \sum_{n=0}^{N-1} f(n)e^{-j\frac{2\pi}{N}pn} \quad (3.41)$$

By applying DFT algorithm, a sequence of N real numbers n is transformed into a sequence of N complex numbers p . The relation between the DFT and the FT is that the Fourier coefficients $F(p)$ are samples of $F(\xi)$ as expressed by Eq.3.42

$$F(p) = F(\xi) \Big|_{\xi=p/N} \quad p = 0, 1, \dots, N - 1 \quad (3.42)$$

All the DFTs of this work are computed using the Fast Fourier Transform (FFT) algorithm of MATLAB [39].

Practically the FT returns the values of the periodic contents of the input, that is how much content for every single periodicity is present in the signal. The single periodicity could be a frequency or a wavenumber, which is a spatial frequency. When the independent variable x of Eq.3.40 represents the time (in seconds), the transform variable ξ represents the frequency (in hertz). The displacement history of a node (underlined in Fig.3.11) of the aluminum plate FE model of Chap.2, which is represented in Fig.3.12(a), is used as an example. The FFT algorithm of the displacement signals returns the frequency content of Fig.3.12(b). In this figure it is evident the prevalence, in the analyzed signal, of the frequencies around the excitation frequency of 200 kHz, even though a reflection against the edge occurred. The frequencies that compose the abscissae axis are all multiples of the fun-

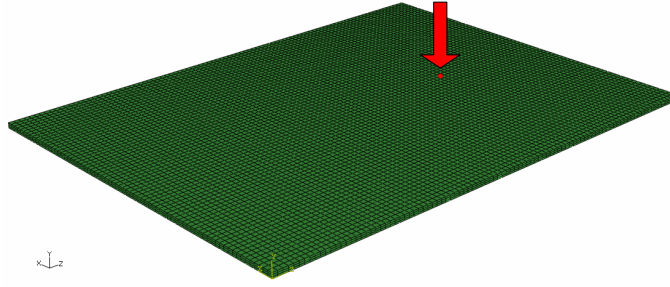


Figure 3.11: Node at coordinated $x=36$ mm, $z=24$ mm on the top surface

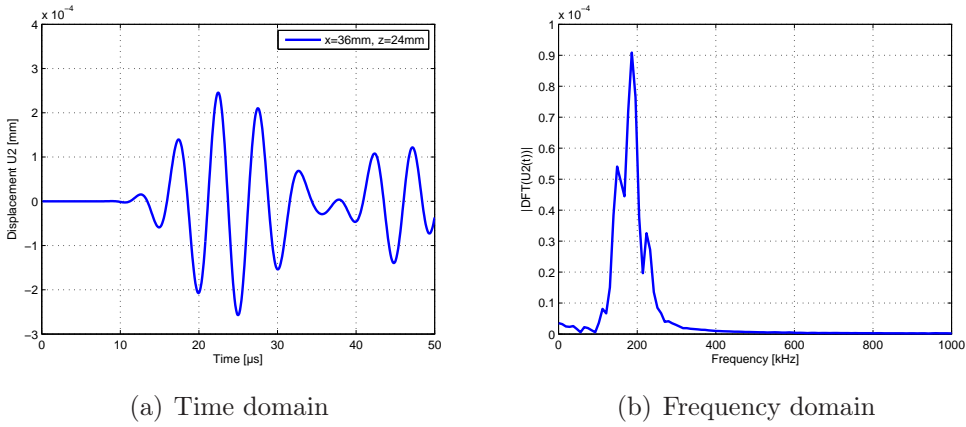


Figure 3.12: Displacement history of a node and its frequency content for the FE model of the aluminum plate

damental frequency that is defined as Eq.3.43,

$$f_0 = \frac{1}{T_f - T_i} \quad (3.43)$$

where T_i is the initial time of the history and T_f is the final time. For such a reason the longer is the observation interval, the higher is the resolution of the frequency domain. The maximum frequency that can be represented is given by Eq.3.44,

$$f_{max} = \frac{1}{T_s} \quad (3.44)$$

where T_s is the sampling time, that is the time between one measurement of displacement and the other. However the highest useful frequency is $1/2 f_{max}$ because of the Nyquist-Shannon sampling theorem that states that a signal can be totally reconstructed only if its highest frequency is at least 2 times

lower than the maximum frequency. So the shorter is the sampling time, the higher is the maximum frequency that can be observed. In this work attention is given mostly to the resolution instead than maximum frequency, because the frequency content is known and it is about the one of the excitation, whereas it is more interesting how this frequency content is distributed. Increase frequency resolution is possible using the zero-padding technique, which consist in adding zeros at the end of the history. Accordingly, by doubling the observation time, the resolution is doubled. This technique does not add any information to the signal, but increase the resolution giving smoother curves. Finally it should be remembered that the FFT algorithm obtains the best computational performance when the number of samples is a power of 2, but MATLAB FFT algorithm works even if the number of sample is prime, though using more CPU time. The number of time samples for all the analyses of this work is 512, as reported in Chap.2.

The FT can be used also considering the position as independent variable x of Eq.3.40. The application of FT algorithm gives, in such a case, the transform variable ξ , which is the wavenumber content of that displacements for that instant. For example the displacements of the nodes along the 0° line (z coordinate) of the aluminum plate FE model, Fig.3.13, can be considered at a given instant. Such instant is fixed at half the observation time, $25 \mu s$. The displacements of the nodes at $25 \mu s$ are reported in Fig.3.14(a). The FT

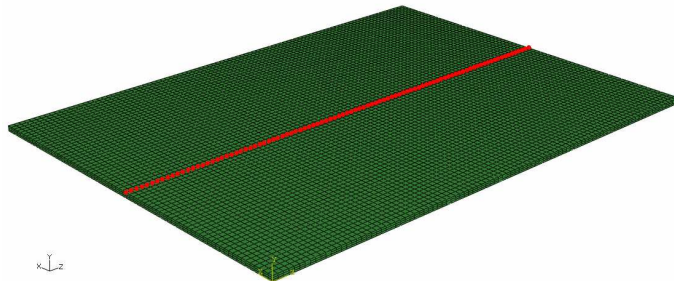


Figure 3.13: Line of nodes along the 0° direction on the top surface of the FE model

values, which are indeed the contents in wavenumber of the displacements along the line, are reported in Fig.3.14(b). In this figure a peak around 1000 rad/m that is almost the value for an A_0 Lamb wave for the aluminum plate at 200 kHz, as it can be seen in Fig.3.3(b). This means that, at a given instant of time along a line of the plate, the wave, which has been generated by excitation, has the correct wave number, which correspond to the one of an anti-symmetrical Lamb wave. The same considerations that have been made for the frequency resolution and maximum frequency are valid also for

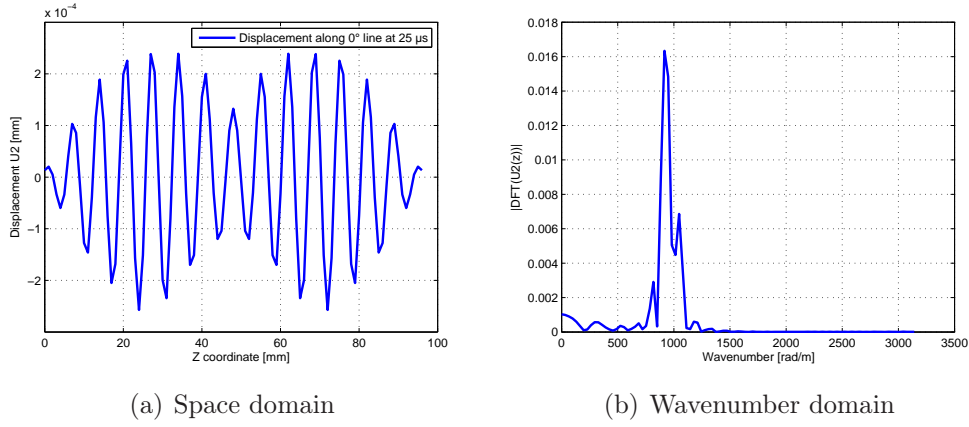


Figure 3.14: Displacement along the 0° line and its wavenumber content for the FE model of the aluminum plate

wavenumber resolution, which has the expression reported in Eq.3.45

$$w_0 = \frac{1}{z_f - z_i} \quad (3.45)$$

and maximum wavenumber which is given by Eq.3.46.

$$w_{max} = \frac{1}{z_s} \quad (3.46)$$

Eq.3.45 and Eq.3.46 mean that the bigger is the plate, the higher is the wavenumber resolution, and the higher is the number of point in which the displacement is recorded, the higher is the wavenumber that can be measured. The zero-padding technique can also be used in this case to increase the wavenumber resolution, by adding zeros at the coordinate vector, as though the plate was larger than it really is. Once more, this technique gives smoother results, but does not increase the level of information.

Now the concept of the FT can be extended to more than one dimension. In fact, the presented approach to extract the wavenumber content is valid just for one line of points and for a specific time, but the interest in this work is to find the wavenumber content for every directions and for a specific frequency.

3.6.2 Two and three dimensional Fourier transform of numerical data

To obtain more useful results from the displacements histories of the FE model, the use of the FT must be extended to more than one dimension. If the input is a function of two variables $f(t, z)$, e.g. time and coordinates of the nodes along one line, the expression for the DFT should be given by Eq.3.47

$$W(\omega, k_z) = \sum_{t=1}^N \sum_{z=1}^M w(t, z) e^{-j(\omega t + k_z z)} \quad (3.47)$$

where $\omega = 1, 2, \dots, N$ and $k_z = 1, 2, \dots, M$. Considering the displacements time histories of a line of nodes, as the ones that have been underlined in Fig.3.13, and organizing the data in a matrix that has, as columns, the displacement history of a single node of the line, it is possible to compute a bi-dimensional DFT on that matrix. Such bi-dimensional transformation is obtained by simply computing a DFT along the rows and then a DFT along the columns of the resulting matrix. The final result is a matrix that contains the complex values of the bi-dimensional FT, the fourier coefficients. Their absolute values can be plotted in a bi-dimensional graph, that has frequencies on abscissae axis and wavenumbers on ordinates axis. The values of the corresponding coefficients can be represented by isolines, which can be colored proportionally to their level (red: high, blue:low). The higher is the value, the more is the content, in the analyzed signal, of that combination of frequency and wavenumber. The plot that is obtained for the FE analyses of the aluminium plate, which is described in section 2.2 is reported in Fig.3.15. As it can be seen, there is a peak in the plot for the frequencies around the excitation one and for the wavenumbers corresponding to an anti-symmetric Lamb wave A_0 for an excitation at the same frequency. This peak means that the wave that has been generated on the FE plate behaves as a Lamb wave, at least along the 0° line. The value of the peak has no importance because it is related to the amplitude of the wave. The significant information lies in the position of the peak in the frequency-wavenumber plot.

The same consideration about maximum frequency/wavenumber and frequency/wavenumber resolution can be done for the mono or bi-dimensional FT.

The zero-padding technique can be used for the bi-dimensional FT as well. Actually, it is necessary to pad two times with zeros the matrix that has as columns the time histories of the line nodes: the first along the rows, and, when the first DFT has been done, a second time along the columns. If the number of rows and columns is doubled (2X) the resolution is doubled,

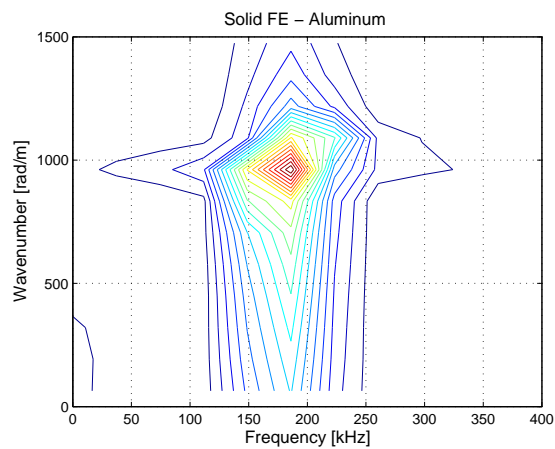


Figure 3.15: Frequency-wavenumber plot for FE model of aluminum plate along 0° line

if is quadrupled (4X) the resolution is four times higher. An example of this improvement can be seen in Fig.3.16. The enhancement with respect to the

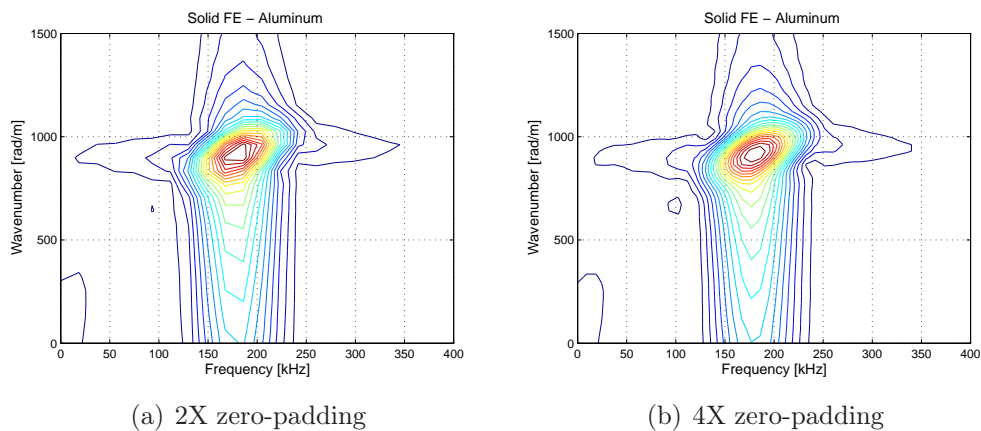


Figure 3.16: Frequency-wavenumber plots for FE model of aluminum plate along 0° line at different zero-padding expansions

plot with no zero-padding of Fig.3.15 is evident, though the enhancement between the 2X and 4X zero-padding is less evident. For this reason all the frequency-wavenumber plots in this work are made using a 2X zero-padding to improve the resolution, thus avoiding an excessive computational cost.

Now the FT can be extended once more to obtain the wavenumber content in every direction. When this result is achieved, considerations can be made on the reliability of FE to model Lamb waves. The application of a three

dimensional FT (two times in space and one in time), using the DFT of Eq.3.48,

$$W(\omega, k_x, k_z) = \sum_{t=1}^N \sum_{x=1}^M \sum_{z=1}^P w(t, x, z) e^{-j(\omega t + k_x x + k_z z)} \quad (3.48)$$

requires the organization of the data in a particular structure. The displacement histories of all the nodes on the top surface of the FE model, which are highlighted in Fig.3.17, are organized in a sort of three dimensional ma-

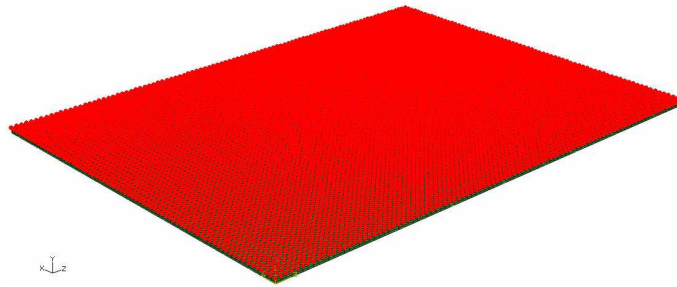


Figure 3.17: Nodes on the top surface of the FE model

trix. Matrix width is the number of nodes along the x axis, whereas matrix height is the number of nodes along the z axis. The depth is the number of time samples as represented in Fig.3.18. For each instant there is a bi-

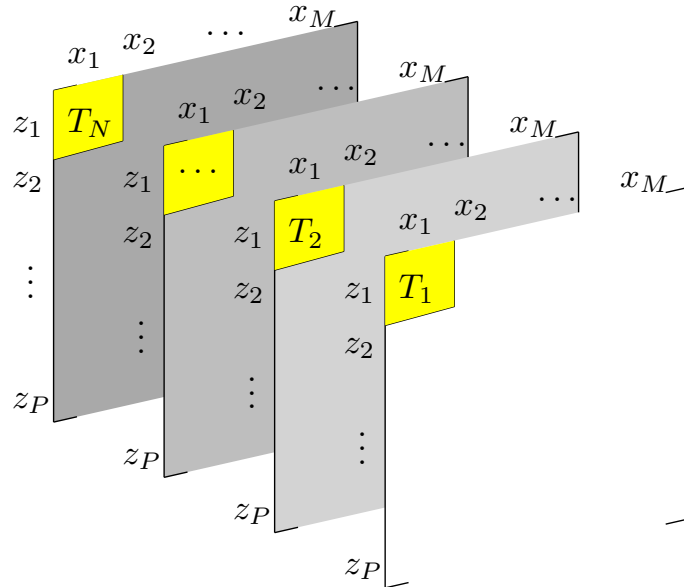


Figure 3.18: Organization of the data in the three dimensional structure dimensional matrix that has as many elements as the the number of nodes on

the top surface. The coordinates of an element in the matrix correspond to the coordinate of a node in the FE model, so that each element of the matrix represent the displacement of that node at that time. The computation of the three dimensional DFT of Eq.3.48 requires the computation of the DFT along the first dimension of the 3D structure (the rows). Once that the first DFT has been performed, a second DFT algorithm is applied considering the second spatial direction, which is represented by the columns of the 3D structure. After the two spatial DFT, an array of matrices with the wavenumber content at the different instants is obtained. A final time DFT is applied along the array direction, to get the frequency content of such wavenumbers. The result is a 3D structure with the same dimensions of the starting one, if no zero-padding has been applied, whose elements are the Fourier coefficients that carry the information about the wavenumber content of the wave, for each direction of propagation and for each frequency. The absolute values of those coefficients can be represented, for a particular frequency, in a bi-dimensional plot that has as axes the wavenumbers in the two directions, k_x and k_z . Each absolute value of the Fourier coefficients represents the content at one particular wavenumber along the x axis, along the z axis and at one particular frequency. The obtained data structure is represented in Fig.3.19. The presence of negative wavenumbers and frequencies is due to the use of

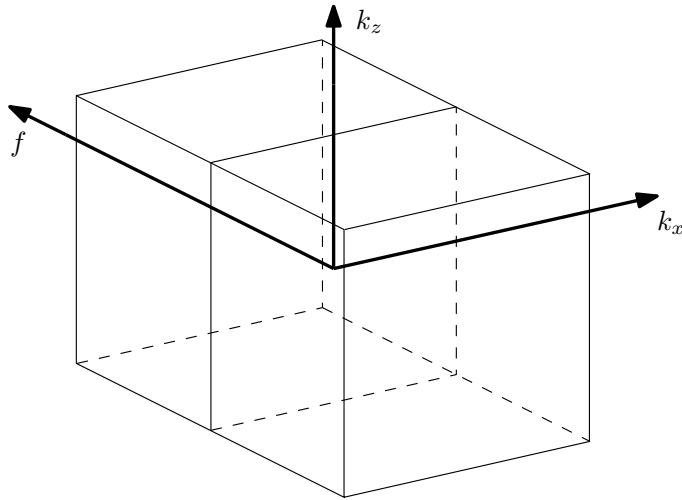


Figure 3.19: Distribution of the Fourier coefficients in the resulting 3D structure

the FT. The negative wavenumbers have been considered, because they represent waves that propagate in the opposite direction of the axes and because they allow to get more significant plots. Negatives frequencies have not been considered because they have no physical meaning. The bi-dimensional plot representing the absolute values of the Fourier coefficients for the aluminum

plate at the nearest frequency to the excitation one of 200 kHz, is reported in Fig.3.20(a). The zero-padding technique can be applied also to this 3D

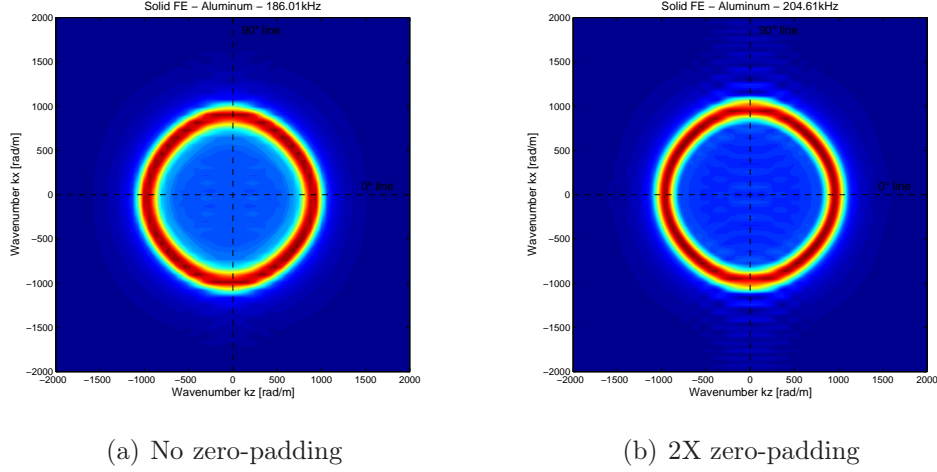


Figure 3.20: Bi-dimensional wavenumber plots at a given frequency for FE model of aluminum plate at different zero-padding expansions

structure, as it has been done in Fig.3.20(b) where the dimensions of the 3D structure has been doubled. It can be observed that the improvement in the visualization is not very significant. The plots of Fig.3.20 show clearly that the wave generated in the aluminum plate has a wavenumbers content k_x and k_z that lies on a circle for a frequency near the excitation one, as expected for an isotropic material.

3.6.3 Comparison of numerical and Semi-Analytical Finite Elements predictions for isotropic

Now the results obtained from the Fourier analysis of the FE model must be compared with the results obtained with the SAFE approach. The frequency-wavenumber plots along the 0° line, and the bi-dimensional wavenumber plots, at the nearest frequency to the excitation one, are reported for each FE models. The first plot shows how the content of the wave changes with the frequency. Moreover it can be checked if the entire peak lies on the wavenumber-frequency curve that is achieved with the SAFE method. A good correspondence of the peak position means that FE method reproduce correctly the wavenumbers of the wave over an interval of frequencies, at least along one direction. The second plot shows, for a given frequency reported on its title, the wavenumber content for each directions.

In Fig.3.21, the results of the DFT application is reported for the aluminum plate model that has been described in Chap.2. A zero-padding technique has been used, by doubling the number of samples. The results of SAFE calculations are also reported. Such results are represented by the curves drawn through dashed lines. As it can be seen the overlapping of the

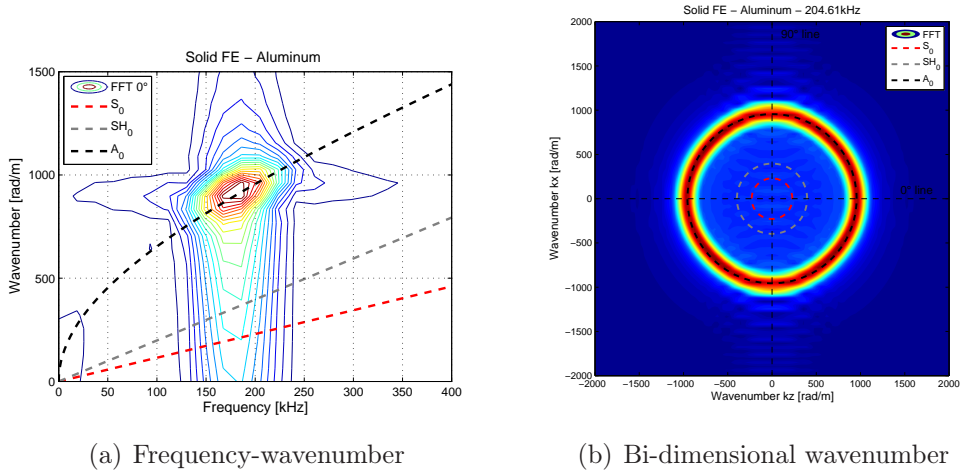


Figure 3.21: Frequency-wavenumber along 0° line and bi-dimensional wavenumber plot for the FE model of aluminum plate

FE plots and the SAFE curves is almost perfect for the A_0 Lamb waves. In Fig.3.21(a) the curve of the A_0 mode of Lamb wave overlap perfectly over the peak that shows the frequency-wavenumber content of the generated wave for the frequencies around the excitation one. This means that the FE model reproduces the correct combination of frequency-wavenumber for all the frequency content of the excitation signal, that is not just a single frequency because of the finite duration of the impulse. In Fig.3.21(b) the circular shape obtained was expected because in an isotropic material the wave propagates in every directions with the same characteristics. Also in this case the curve obtained from the SAFE approach overlaps perfectly over the circular peak of the plot, confirming the reliability of the FE model. In both the plot of Fig.3.21 the curves produced by the SAFE approach for the SH_0 and the S_0 waves are drawn, but there are no peaks under these curves in FE results. One of the main reason for this discrepancy is that the displacement considered (U_2) is the out-of-plane one and these waves have a displacement that is mainly in-plane, so they can not be identified.

3.6.4 Comparison of numerical and Semi-Analytical Finite Elements predictions for composites

In this section the plots of the composite plates modeled through the alternative modeling technique described in Chap.2 are presented. It is recalled that this technique consists in the use of both solid and membrane or shell elements to model the composites and that these elements have different structural roles. The solids take care of the out-of-plane stresses and the membranes/shells take care of the in-plane stresses.

For Plate1, which is the 16 plies carbon fiber plate with orientation $[0^\circ, 45^\circ, 90^\circ, -45^\circ]_{2s}$, the results are represented in Fig.3.22. The resolution is doubled by using zero-padding technique. The overlapping of both the plots

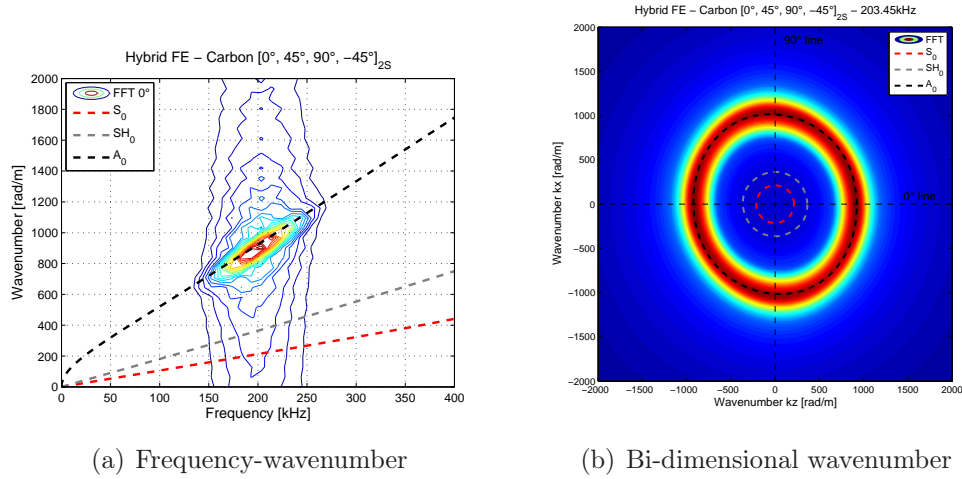


Figure 3.22: Frequency-wavenumber along 0° line and bi-dimensional wavenumber plot for the FE model (alternative technique) of Plate1

with the curves obtained by SAFE approach is perfect also in this non trivial case. Indeed each ply of the composite material has an orthotropic behavior; furthermore the combination of numerous plies with different orientations does not allow to determinate a priori shape of the propagating wave, a numerical analysis must be performed. The frequency-wavenumber result for Plate1 of Fig.3.22(a) is similar to the one of aluminum plate, but here the peak is more defined and the wavenumbers values of A_0 are lower. These facts means that the waves have a smaller range of wavenumbers and longer wavelengths. The bi-dimensional wavenumber plot of Fig.3.22(b) shows that the waves do not propagate according to a circular front, because the locus of peaks is not perfectly circular, but is slightly stretched along a direction of about 100° (calculated starting from the positive axis of k_z), as predicted

by the SAFE approach.

The results for Plate2, which is the 8 plies fiber glass plate with orientation $[0_2^{\circ}, 90_2^{\circ}]_s$, are reported in Fig.3.23. The resolution is doubled by using

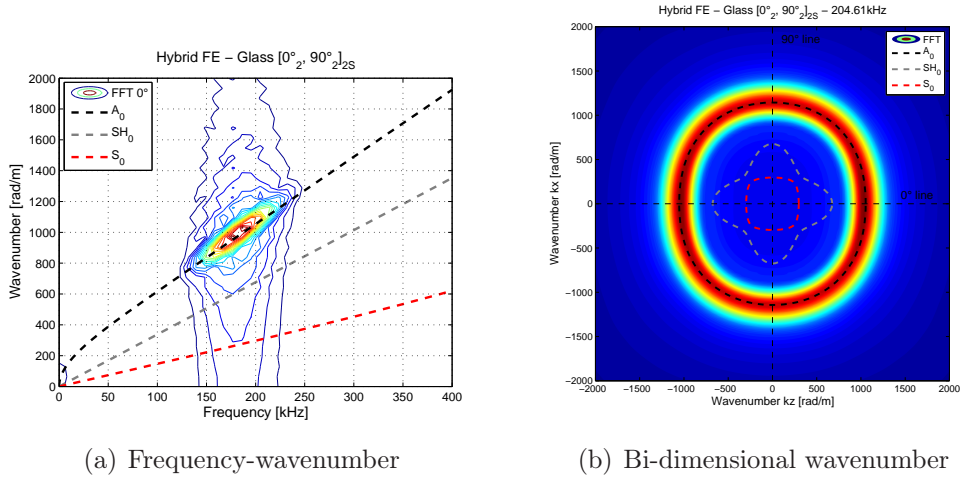


Figure 3.23: Frequency-wavenumber along 0° line and bi-dimensional wavenumber plot for the FE model (alternative technique) of Plate2

the zero-padding technique. In this case the frequency-wavenumber plot of Fig.3.23(a) is very similar to the one of Plate1, except for the wavenumber values that here are higher. The bi-dimensional wavenumber plot of Fig.3.23(b) presents a locus of the peaks for the A_0 wave that is completely different with respect the one of Plate1, because the particular orientation of the plies produces a wave that travels considerably faster along the z axis. As a consequence, the wavenumber k_z is lower because the wavelength is higher in that direction. This behavior is predicted correctly by both the FE model and the SAFE approach, so the overlapping of the two methods is perfect.

The results for Plate3, which is the 8 plies unidirectional fiber glass plate with orientation along the 0° line, are reported in Fig.3.24. Also in this case, the resolution is doubled by using the zero-padding technique. In Fig.3.24(b) the behavior already presented in Plate2 is even more evident, because all the plies are aligned along the same direction. The wave that propagates along that direction is as fast as in Plate2, but the wave that travels in the perpendicular direction is much slower. Consequently the wavenumber is much higher and the stretching of the peak locus is more evident. The wavenumber-frequency plot of Fig.3.24(a) is very similar to the one of Plate2, because these plots are both taken along the 0° line and the behavior of the waves along that direction does not change considerably for the two cases.

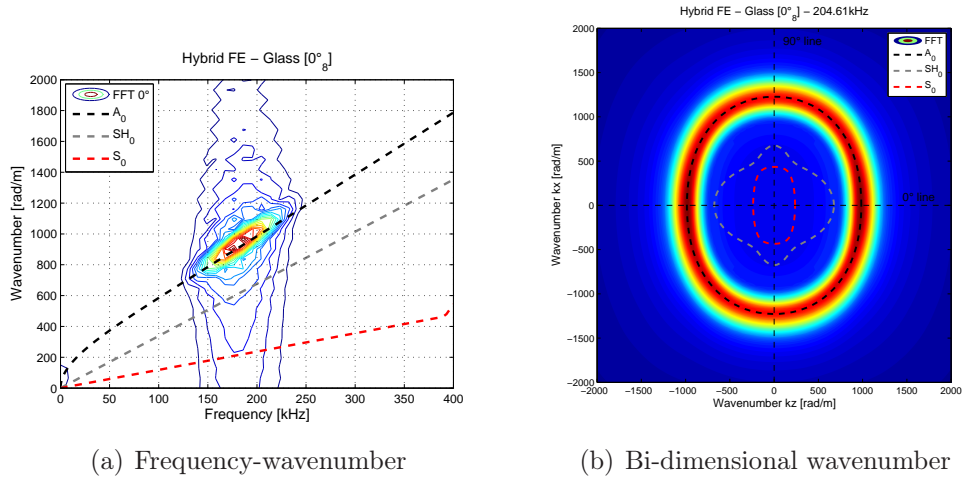


Figure 3.24: Frequency-wavenumber along 0° line and bi-dimensional wavenumber plot for the FE model (alternative technique) of Plate3

In all these three cases just the anti-symmetric Lamb wave A_0 can be detected, because the alternative modeling technique has solid elements that do not allow the modeling of S_0 or SH_0 that because they do not have the Poisson's modulus that connect the stretching along the direction perpendicular to the plate and the ones in the plane. So when one of these solid elements is stressed in y direction it does not create any displacements in both x or z direction. For this reason no peaks are present under the S_0 or SH_0 curve generated from the SAFE approach.

Chapter 4

Experimental analysis

Experimental analysis is a necessary step in this work, because no specific data can be gathered from literature about the particular composites adopted. Moreover few comparison exist between numerical data, which are obtained by solid models of composite plates and experimental analysis about wave propagation in composites. For these reasons the numerical data obtained, both from FE analysis and SAFE approach, must be validated through comparison with the data acquired from the real composite plates that have been manufactured using the same materials that have been considered for the development of numerical and semi-analytical models. In this chapter it is described how the experimental tests are performed, what instruments are used and how they work. The obtained results are presented as well as the processing of data, which is carried out by means of the same technique adopted in chapter 3. Finally the comparison of the results is proposed.

4.1 Experimental setup

Waves in thin plates require specific measurement instruments which reduce to the minimum the intrusiveness, because these waves are very susceptible at every changes in mass or stiffness distribution. For this reason, vibrations can not be measured with an accelerometer mounted on a plate, because, though small, the sensor has a mass, which can alter the mass distribution of a thin plate and it also has a finite dimension and stiffness, which can alter the stiffness of the plate near the sensor. Moreover, to get the displacements in enough points, in order to apply the technique based on the Fourier analysis, which has been presented in the previous chapter, the number of sensor should be unfeasible. Finally, the bandwidth of classical

accelerometer does not exceed few kHz, whereas in this work almost one MHz is required. The instrument that can solve all these problems is the Laser Doppler Vibrometer (LDV), a very expensive and precise tool which uses a laser beam to gather the information about the analyzed object. The experimental tests have been performed at Daniel Guggenheim School of Aerospace Engineering at Georgia Institute of Technology in Atlanta, Georgia, where a scanning vibrometer Polytec PSV-400 is available.

The experimental setup consists of the following parts:

- The scanning vibrometer Polytec PSV-400, positioned at about 4 meters away from the specimen;
- The specimen, that is the composite plate clamped on a table;
- The piezoelectric disk actuator, mounted on the rear of the plate to generate the proper excitation wave;
- The function generator, to control the piezoelectric actuator;
- The vibrometer controller and the data management system, to control the vibrometer and store the data.

The graphical representation of the experimental setup is in Fig.4.1. Now a

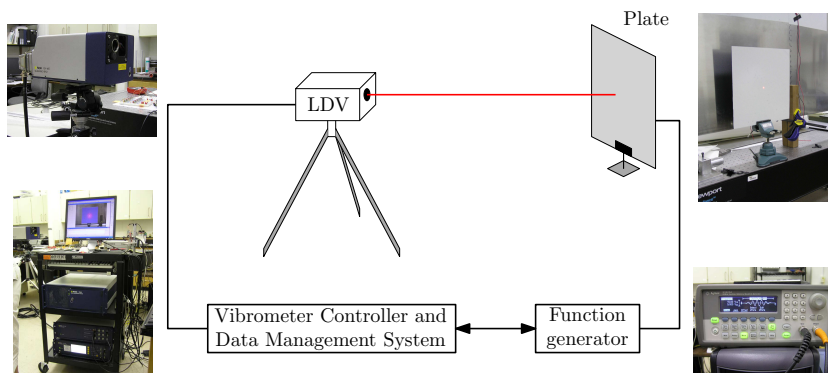


Figure 4.1: Experimental setup

description of each component is provided.

In order to measure the displacements of the plate without disturbing the dynamics of the phenomenon, a non-contact technique is required, as the one that is allowed by as the laser doppler vibrometry adopted by the Polytec PSV-400 system. This technique consists in comparing two laser beams, i.e. an internal reference beam and a test beam reflected by the sample. The comparison is made using a laser interferometer that measures the difference

in frequency between the two beams by superimposing them. A schematic representation of the LDV is reported in Fig.4.2. The internal laser pro-

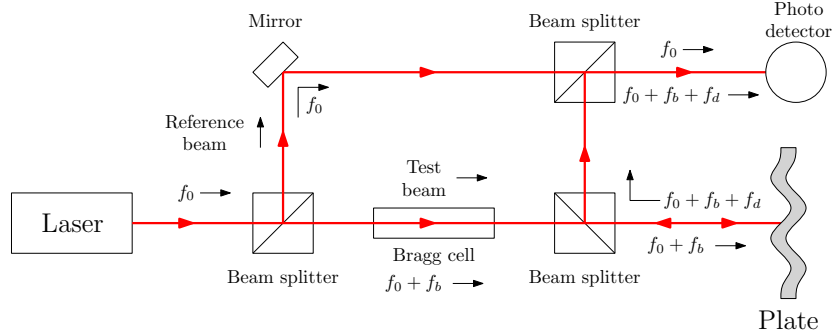


Figure 4.2: Schematic representation of the Laser Doppler Vibrometer

duces a coherent beam of light at frequency f_0 . This beam is splitted into two by a partial reflective mirror. These two beams are the reference beam and the test beam. The reference beam goes directly to the photo detector, whereas the test beam passes through a Bragg cell which adds a frequency shift f_b . The Bragg cell is an acousto-optic modulator which uses sound waves in a transparent medium, like quartz or glass, to generate a shift in the frequencies of light passing through it. Thanks to the exploitation of the fact that sound waves traveling into transparent material can locally change its index of refraction, they can be thought as periodic planes of expansion and compression acting as a diffraction grating for the incoming beam. The properties of the light exiting from the Bragg cell can be controlled in frequency, because the beam is scattered by moving planes. Thus the frequency is shifted by multiple amount of the sound wave frequency in the cell, Eq.4.1

$$f_{exit} = f_0 + m f_S \quad (4.1)$$

where $m = \dots, -2, -1, 0, 1, 2, \dots$ is the order of diffraction and f_S is the frequency of the sound wave. Usually, the shift is about 30-40 MHz, but it can also be higher, up to 400 MHz. The frequency shifted beam is then directed to the plate, whose movement adds a further Doppler shift to the frequency f_d , whose value can be calculated with Eq.4.2.

$$f_d = 2 \frac{v(t) \cos(\alpha)}{\lambda} \quad (4.2)$$

The $v(t)$ is the velocity of one point of the plate as function of time, α is the angle between the laser beam and the velocity vector, and λ is the wavelength of the beam. The beam is scattered from the plate in every direction, but

part of the light, that now has a frequency of $f_0 + f_b + f_d$, is collected by the LDV and routed to the photo detector. Here it is combined with the reference beam that comes directly from the laser source. However, the initial frequency of the beam f_0 is very high, of the order of 10^{14} Hz, much higher than the bandwidth of the photo detector. For this reason the signal f_0 is not considered. The response of the detector comes from the beat frequency between the two beams, which is at $f_b + f_d$, of the order of tens of MHz. Thus the output of the photo detector is a frequency modulated signal, with f_b as carrier frequency and f_d as modulation frequency. The signal can be demodulated to derive the velocity of the plate in the point hit by the laser beam as function of time. Modern LDV, as the Polytec PSV-400, can measure velocities from few nm/s to some m/s and are sensible to displacements of the order of picometers (10^{-12} m), whereas the sampling frequency can reach 2.56 MHz. Moreover the PSV-400 has the scanning ability, meaning that the laser beam can be moved without moving the instrument, allowing the automatic scanning of an entire area of the plate, just programming the right pattern of scanning points.

The composite plates, which have been manufactured by the Dipartimento di Ingegneria Aerospaziale of Politecnico di Milano, have the same characteristics of the FE models of Chap.2, except for the dimensions which are larger in order to make the LDV analysis easier. The main characteristics are summarized in Tab.4.1. Before starting the analysis, the plate must be

		Units	Value
Plate1	Material		T700/SE84HT
	Sequence		$[0^\circ, 45^\circ, 90^\circ, -45^\circ]_{2s}$
	Number of plies		16
	Dimensions	$[mm]$	315 x 315 x 2.3
Plate2	Material		S2/CYCOM5216
	Sequence		$[0_2^\circ, 90_2^\circ]_s$
	Number of plies		8
	Dimensions	$[mm]$	315 x 315 x 1.84
Plate3	Material		S2/CYCOM5216
	Sequence		$[0_8^\circ]$
	Number of plies		8
	Dimensions	$[mm]$	315 x 315 x 1.84

Table 4.1: Summary of the anisotropic plates analyzed in this work

prepared. A thin adhesive reflective film is applied on one side of the plate,

because, especially for the glass fiber plates, the translucency of the material does not allow a correct reflection of the laser beam. This film does not significantly alter either the mass or the stiffness of the plates because is very light and flexible.

To excite the plate an exciter is required which must be as less intrusive as possible. It must have enough force to adequately excite the plate and a band of at least 200 kHz i.e. that is the frequency of excitation used for the FE models. The only actuator that has all these characteristics is the piezoelectric one, also called PZT. A piezoelectric ceramic disk actuator is fixed in the middle of the each plate by glue, on the side which is not scanned by the LDV. The characteristics of the PZT are reported in Tab.4.2. Both the electrodes of the transducer are positioned on the same side of the

	Units	Value
Manufacturer		Steiner & Martins
Model		SMD20T21F1000R
Diameter	[<i>mm</i>]	20
Thickness	[<i>mm</i>]	2.1
Resonant frequency	[<i>MHz</i>]	$1 \pm 5 \%$
Electromechanical coupling coefficient		$\geq 40 \%$
Resonant impedance	[Ω]	≤ 4
Static capacitance	[<i>pF</i>]	$2000 \pm 15 \%$ @1kHz

Table 4.2: Characteristics of the piezoelectric disk actuator

disk. On these electrodes wires are welded. The plate prepared for the LDV analysis is pictured in Fig.4.3. Initially this plate is clamped on one side and

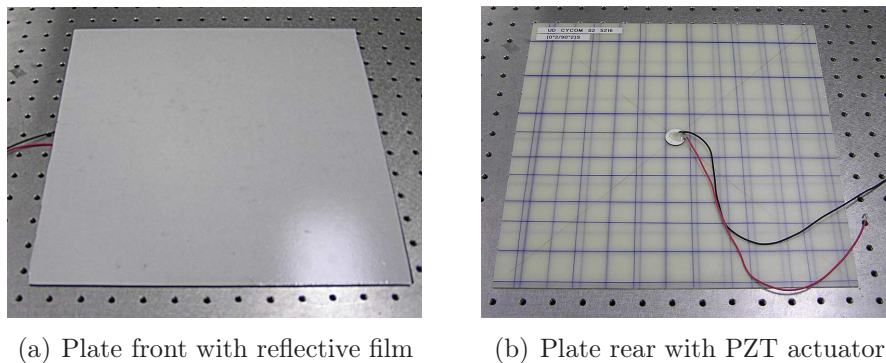


Figure 4.3: Plate2 prepared for the experimental analysis

perpendicularly positioned to the laser beam, as shown in Fig.4.4. The parts

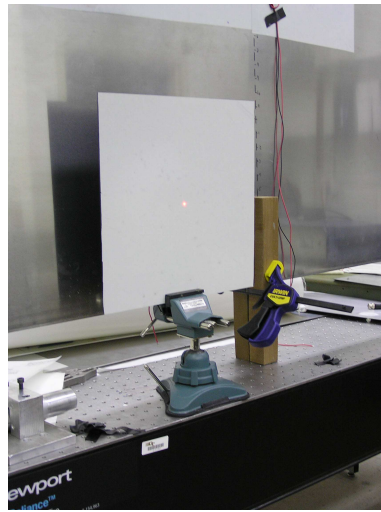


Figure 4.4: Plate clamped and positioned perpendicular to the laser beam

of the clamp which are in contact with the plate are rubber made to avoid an excessive alteration of the results with respect to an hypothetical free plate.

The input of the transducer is generated by the function generator, an Agilent 33220A pictured in Fig.4.5. The signal is a series of 7 cycles of sinu-



Figure 4.5: Function generator Agilent 33220A

oid modulated by an Hanning window. The frequency of the sine function is 200 kHz, as used in FE. With respect to the FE, the number of cycles is a bit higher (in FE is 5.5), but this has no negative effects. On the contrary it allows a longer time of observation, thus an higher resolution in frequency is obtained. This instrument is synchronized with the vibrometer controller to exactly excite the plate when required.

The vibrometer controller of Fig.4.6 manages all the instruments involved in the experiment; it defines the pattern of points in which the LDV has to



Figure 4.6: Vibrometer controller and data management system

measure displacements as well as the sample frequency and others parameters of acquisition. Moreover, it defines when the excitation signal must be applied. Then it also provides to transfer all the data acquired to the data management system, which allows storing them for a post-processing analysis. The pattern of measuring points covers the inner part of the plate, whereas the parts situated near the edges are excluded to avoid any boundary effect, as represented in Fig.4.7. A scanning area 300 mm wide allows an

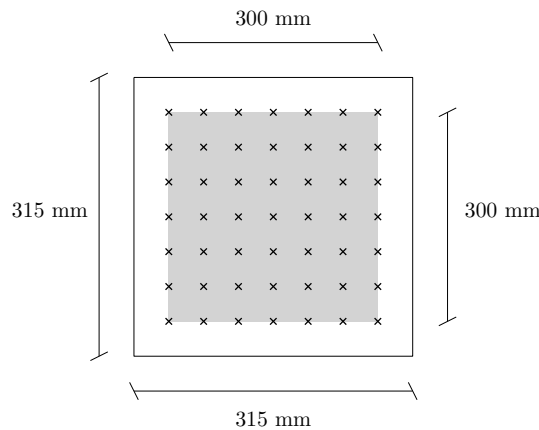


Figure 4.7: Representation of the scanned area of the plate

higher wavenumber resolution with respect to the FE model, which is just 96 mm x 72 mm. In order to achieve an high enough maximum wavenumber to represent all the waves in the plate, the number of scanning points must be very high, as explained by Eq.3.46. Resolution is preferred to maximum

wavenumber, also to reduce post-processing computational time that will derive if a very high number of points is considered. For this reason it is decided to use the maximum scanning area and a square pattern of 12100 scanning points, 110 for each side. The experimental acquisition of the data is made at the maximum sampling frequency of the instrument, that is 2.56 MHz and 512 samples are taken, to speed up the FFT algorithm. This means an observation time of 200 μs . The exciter repeats the 7 cycles excitation 10 times in a second. For each measurement point, 10 time histories are recorded and then an average operator is applied. This procedure enhance the quality of the measurement and reduces the noise. This means that the transducer is excited with a frequency of 10 Hz, meaning that every 0.1 seconds the excitation signal described before is applied to the PZT. This frequency derives from a trade-off between the time required for the plate to sufficiently damp the previous excitation and the total time of acquisition, which must not be excessive. The synchronization of the function generator with LDV is made by vibrometer controller, in order to exactly start the acquisition when the excitation is applied. This must be done not only for the repetition of the measure on the same point, but also for the changing of the measuring point. Thanks to this synchronization the final result of the analysis in every point of the pattern is as if it had been done at the same time and not in series. Finally the data exported to the data management system are the displacements of each scanning point as function of time. The specification of the experimental system are resumed in Tab.4.3.

	Units	Value
Scanned area	[mm]	300 x 300
Scanning points		12100
Sampling frequency	[MHz]	2.56
Observation time	[μs]	200
Wavenumber resolution	[rad/m]	20.9
Maximum wavenumber	[rad/m]	1151
Repetition per point		10
Measuring time		3h 30m

Table 4.3: Resume of the specification of the experimental system

4.2 Experimental results

Now the extraction from the experimental data of some measures that can be compared with the ones obtained numerically using the FE or the SAFE is proposed. The data obtained from the experimental analysis are the out-of-plane displacements of the scanning points as function of time. To these data it is possible to apply the same Fourier analysis techniques seen in previous chapter, after organizing the data in a 3D structure as in Fig.3.18. The application of a bi-dimensional FT to the displacement histories of the points along the 0° line leads to the plot of a bi-dimensional frequency-wavenumber graph, which represents the content of the wave generated by the PZT actuator for a range of frequencies. This graph, for the carbon fiber Plate1 is reported in Fig.4.8(a). In this figure it can not just be seen one peak

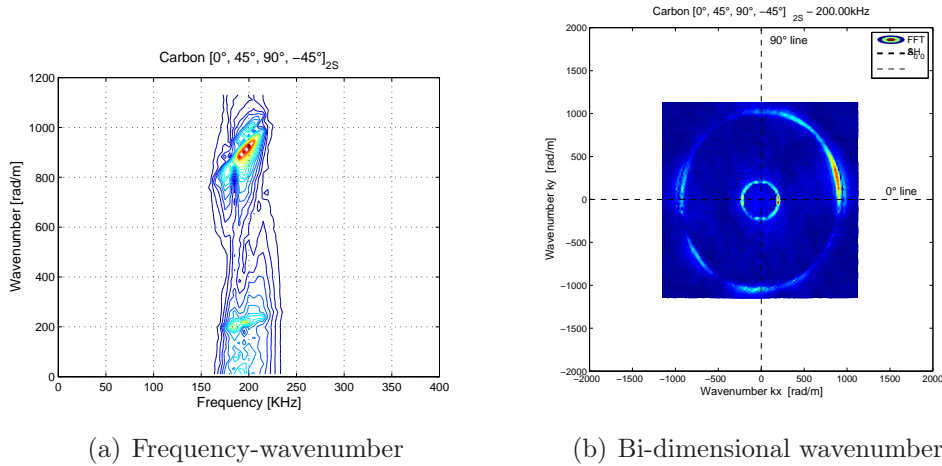


Figure 4.8: Frequency-wavenumber along 0° line and bi-dimensional wavenumber plot for experimental data of Plate1

for the anti-symmetric Lamb wave A_0 , as in the FE model, but also another smaller peak for lower wavenumbers. This peak represents the symmetrical Lamb wave S_0 that can not be caught by the FE by applying the suggested modeling technique. Thanks to the use of all the scanning points of the plate, it is possible to plot the wavenumber content of the wave for every direction at one well defined frequency, i.e. the one of the excitation signal: 200 kHz, as represented in Fig.4.8(b). Here the difference with respect to the FE model is evident: the inner and smaller circle represents the S_0 mode. The behavior of this mode, as function of angle of propagation, is almost the same and for this reason its representation is almost a circle. For this kind of plot it is decided to keep the same axes limits of the previous chapter to

simplify the comparison and to show the limited maximum wavenumber that can be represented in experimental analysis.

Experimentally with the LDV is possible to catch also the all-in-plane movements, as the SH_0 waves. To achieve this result, since the only displacement seen by the LDV is the out-of-plane one, it is possible to repeat the experiments with the plate rotated by a small angle ϕ with respect to the laser beam. This allows to the in-plane displacement to have an out-of-plane component, as shown in Fig.4.9, which can be measured. The angle chosen

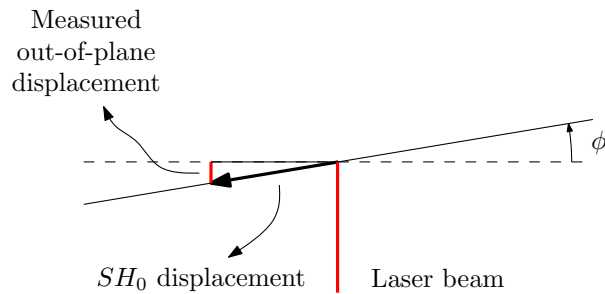


Figure 4.9: Top view of the plate rotated to catch the in-plane wave SH_0

for this analysis is 14° , because it is enough to see the SH_0 mode and is not too large to alter the scanning width. As a matter of fact the amplitude of the resulting out-of-plane component is 24% of the in-plane component, since $\sin(\phi) = 0.24$ and the scanning width just becomes 3% shorter, because $\cos(\phi) = 0.97$. However this technique does not allow the measurement of the vertical in-plane displacements, because the plate is only horizontally tilted. For this reason a part of the bi-dimensional wavenumber plot for the SH_0 wave is not visible, i.e. the part near the 90° direction. This particular observation technique allows to obtain the plots of Fig.4.10. In Fig.4.10(a) is visible another peak between the two already seen in Fig.4.8(a), which represents the SH_0 wave. Its value is higher than the one represented, but in this work the interest is focused on the position of the peak in the frequency-wavenumber plot and not on its value. The bi-dimensional wavenumber plot of Fig.4.10(b) represents the behavior of the SH_0 wave as function of propagation angle. It is also visible what already said about the impossibility of representing this wave for the 90° direction, as the locus of SH_0 peaks is open. All the composite plates provided are analyzed in a tilted position with respect to the laser beam, in order to achieve the largest amount possible of information.

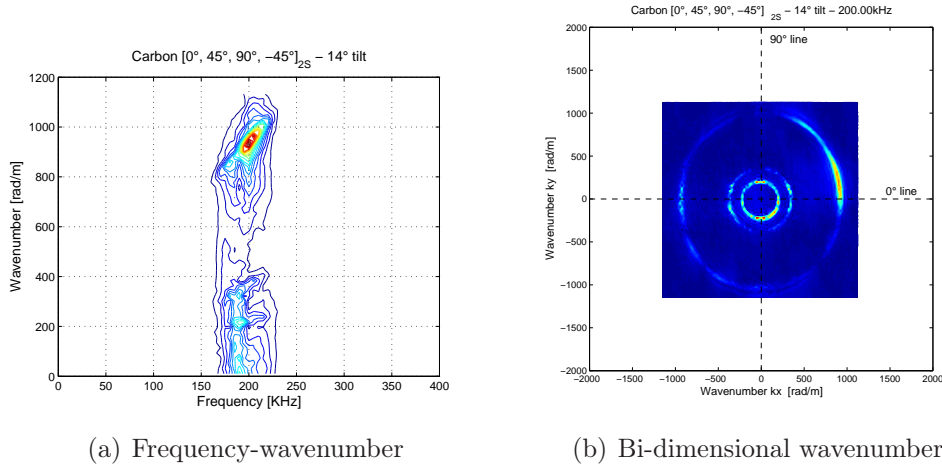


Figure 4.10: Frequency-wavenumber along 0° line and bi-dimensional wavenumber plot for experimental data of Plate1 14° tilted

4.3 Comparison with Semi-Analytical Finite Element predictions for composite plates

Now the frequency-wavenumber plots and the bi-dimensional plots, deriving from the experimental data on all the composite plates provided, are compared with the curves computed with the SAFE approach. These curves have been demonstrated, in the previous chapter, to be perfectly coincident with the same kind of plots obtained from the FE data, as far as the A_0 waves are concerned. If the agreement between SAFE and experiments is good, it can be definitely stated that the waves generated in a FE model respect the behavior of the real waves in every direction of propagation.

For Plate1 the frequency-wavenumber plot along the 0° line is reported in Fig.4.11. In this figure it can be noticed the perfect overlapping of the three peaks with the curves, even though the peaks relative to the S_0 and SH_0 waves are smaller than the one of the A_0 wave. The bi-dimensional wavenumber plot for Plate1 is reported in Fig.4.12. As already said the locus of the peaks of SH_0 wave can not be closed because the in-plane displacements can just be seen horizontally. Thus only the k_z component of the wave can be plotted and this component assumes null values along the 90° direction. Nevertheless the curves computed with the SAFE approach are perfectly overlapped to the peaks for every direction. This means that the modeling technique for the FE model of Chap.2, is valid to describe the A_0 mode for an quasi-isotropic composite plate.

The frequency-wavenumber plot along 0° direction for Plate2 is repre-

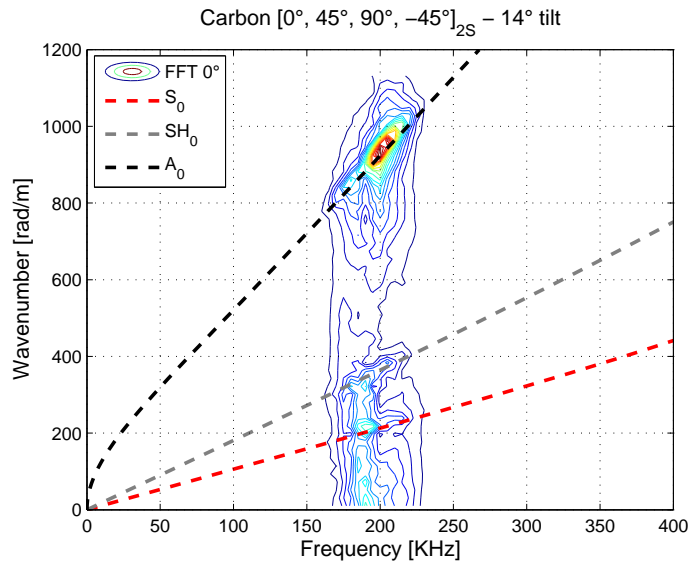


Figure 4.11: Frequency-wavenumber plot for experimental Plate1, 14° tilted along 0° line

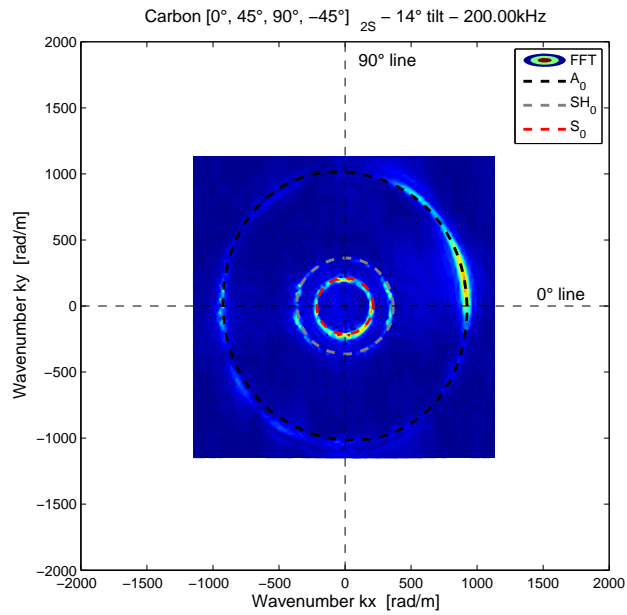


Figure 4.12: Bi-dimensional wavenumber plot for experimental Plate1, 14° tilted

sented Fig.4.13. Here the SH_0 peak is not present, because Plate2 has been accidentally measured with an orientation of 90° with respect to the correct

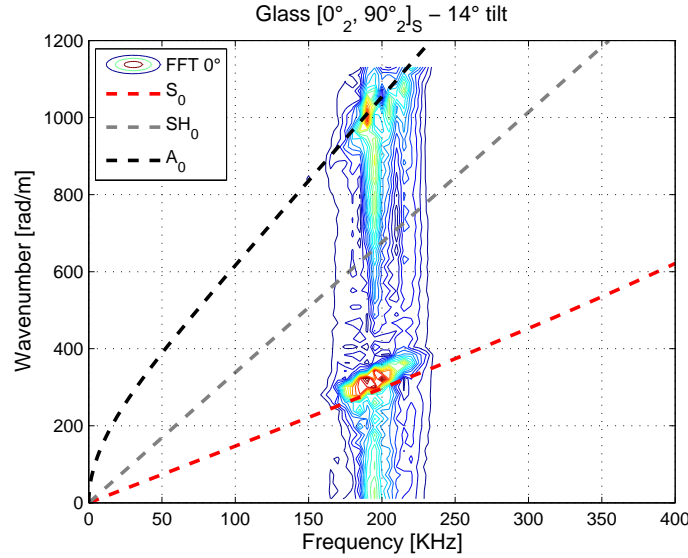


Figure 4.13: Frequency-wavenumber plot for experimental Plate2, 14° tilted along 0° line

one. In fact this is not a problem, because it is as if a plate with orientation $[90_2^{\circ}, 0_2^{\circ}]_s$ had been analyzed. This means that every information obtained is rotated by 90°. For this reason, the measured out-of-plane component of the SH_0 wave, that can be only horizontally measured, is relative to the SH_0 wave which propagates along the 90° fibers. Thus in this case the SH_0 peak can be seen only around 90° direction, whereas around 0° the peak vanishes. The frequency-wavenumber plot along 90° direction can be seen in Fig.4.14. In this figure the SH_0 peak is small, but visible. Moreover it can be seen that in this case the wavenumber limit is very close to the highest wavenumber present in the wave and this should be avoided in future analyses, by keeping the same number of scanning points, but reducing the scanning area. Despite this fact, the peaks in both Fig.4.13 and Fig.4.14 lie on the curves given by SAFE approach and the overlapping is very good. The discussion about the accidental rotation of the plate can be seen more clearly in the bi-dimensional wavenumber plot of Fig.4.15. Here it is clearly shown that the locus of peaks of SH_0 wave is open around 0° direction instead of 90° as in Plate1. However the comparison with the SAFE curves is very good, for every direction. Since also the FE bi-dimensional wavenumber plot for Plate2 perfectly overlaps to the same SAFE curves, it can be stated that the wave modeled with FE has the same behavior of the experimentally measured wave, also in this case, where fibers are coupled with the largest possible angle between them, that is 90°.

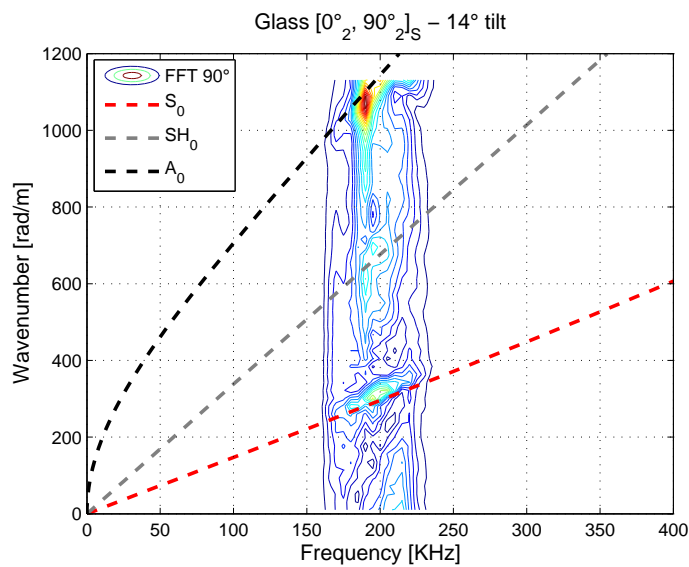


Figure 4.14: Frequency-wavenumber plot for experimental Plate2, 14° tilted along 90° line

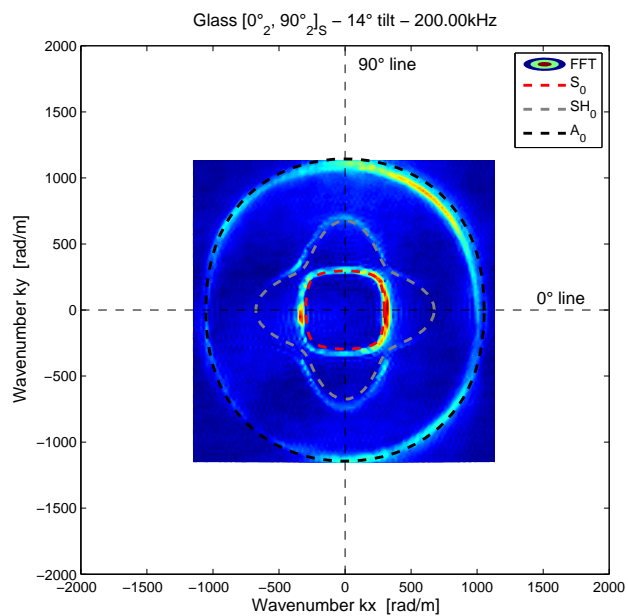


Figure 4.15: Bi-dimensional wavenumber plot for experimental Plate2, 14° tilted

Also Plate3, the unidirectional plate, has been accidentally analyzed rotated of 90°. For this reason it is proposed the frequency-wavenumber plot

along the 90° direction in Fig.4.16. In this figure the peak for the SH_0 wave

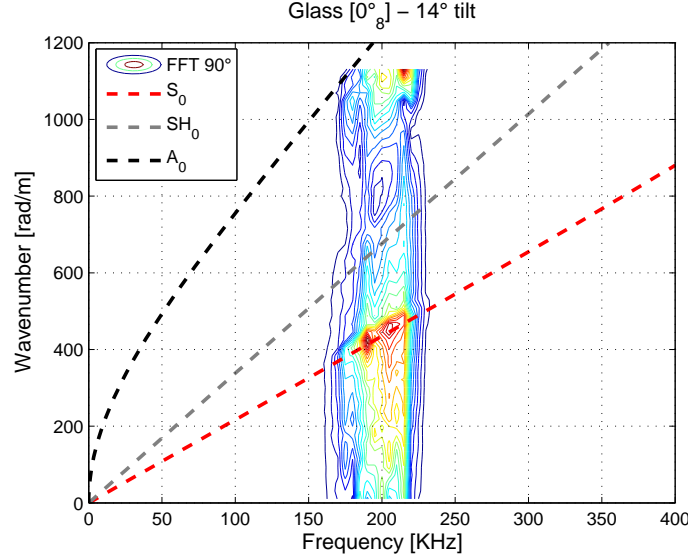


Figure 4.16: Frequency-wavenumber plot for experimental Plate3, 14° tilted along 90° line

is almost invisible. This is due to the fact that the component which can be observed is part of the SH_0 wave traveling perpendicularly to the fibers, so it is more damped. Unfortunately the maximum observable wavenumber here is not enough to contain the SAFE A_0 curve, but its peak is slightly inside the limit. This fact can be clearly seen in the bi-dimensional wavenumber plot of Fig.4.17. The locus of the peaks for the A_0 mode is just inside the maximum wavenumber in 90° direction, thus it does not overlap to the SAFE curve for that wave. On the contrary, the bi-dimensional wavenumber plot of the FE model overlaps correctly to the SAFE prediction. This means that, in the direction perpendicular to the fibers, the real behavior of a unidirectional composite plate is slightly different to the one numerically modeled. This behavior may be due to the damping effect of the resin, which is not considered in the numerical analyses of this work. It can play an important role in a direction along which no fibers are present. However, further analyses should be executed with an higher maximum wavenumber to check if this phenomenon is still present or if it is just a numerical effect. Nevertheless, the behavior of the SH_0 and S_0 waves is correctly modeled, thus meaning that also for the unidirectional plate, the FE model of Chap.2 correctly reproduces the wave propagation, only with a little imprecision in the direction perpendicular to the fibers. As a matter of fact, from a practical point of view, unidirectional laminates are rarely employed in real-world structures.

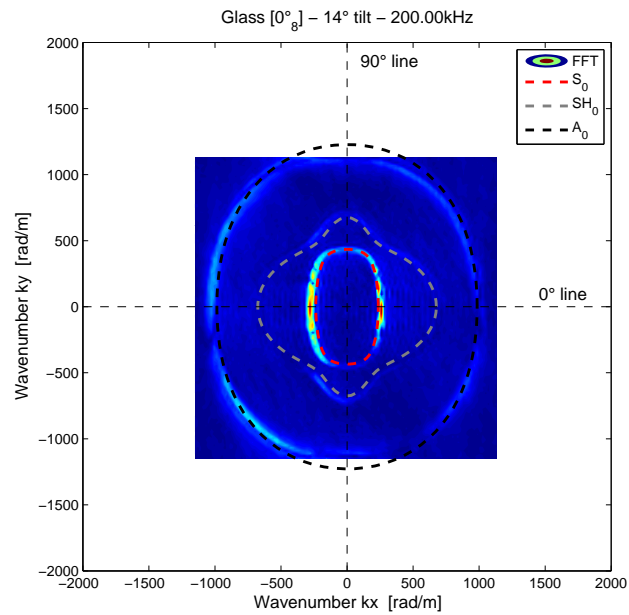


Figure 4.17: Bi-dimensional wavenumber plot for experimental Plate3, 14° tilted

It should be noted that damping is never considered in the numerical or analytical predictions of this work, and that a discrepancy seems appearing only for 90° direction in unidirectional laminates. It can be concluded that resin damping effects are not important for the definition of peak locus in laminates which are commonly used in engineering applications.

Conclusions and future works

The objective of this work is the validation of a finite element method to correctly represent the guided waves in plates. Initially the modeling technique has been presented along with all the hints to model this phenomenon using conventional solid elements. Then different models of plate in isotropic and composite materials have been created using this technique and applying explicit integration time scheme. Modeling has been carried out taking into consideration the need of reducing the computational costs, which can easily reach unacceptable levels. The possibility to reduce the number of degrees of freedom has been explored by applying solid elements with an aspect ratio greater than 1. It has been proved that the aspect ratio is indeed a fundamental parameters for the quality of the results. However, good results can be obtained by using aspect ratio up to five, which represent a dramatic reduction in the number of degree of freedom required for a ply-by-ply modeling of a composite laminate. The numerical comparisons have been focused on measuring the anti-symmetric Lamb waves, of A_0 type. However symmetric waves can be correctly reproduced by the developed model as has been demonstrated in the scattering test. This test has been presented in order to verify the possibility of the FE model to reproduce the waves that are generated after the impact of a S_0 wave against a damage i.e. a partial hole in an aluminum plate. Even though in this thesis no deep analyses have been performed on this argument, the obtained results are very promising and motivate the effort for a thoughtful validation of Lamb waves propagation in composites, where the potential of health monitoring technique could be fully exploited.

Successively a modeling technique, developed at Politecnico has been applied. Such technique implies both the use of solid and bi-dimensional elements to model composite material and it is well-suited to represent interlaminar damages between the layers. Using this technique three models have been created, in order to reproduce the largest amount of possible laminates. These models are: an quasi-isotropic carbon fiber plate with orientation $[0^\circ, 45^\circ, 90^\circ, -45^\circ]_{2s}$ called Plate1, a fiber glass plate with orien-

tation $[0_2^{\circ}, 90_2^{\circ}]_s$ called Plate2 and an unidirectional fiber glass plate $[0_8^{\circ}]$ called Plate3. Because of the particular approach adopted in these models, the symmetric waves S_0 can not propagate. This is due to the material applied to the solid elements, which does not model the link between the strains in the in-plane directions with the strains in the out-of-plane directions. For every FE model, the out-of-plane displacement histories of the nodes positioned on the top surface of the plate are measured.

To compare the obtained results another tool has been implemented in a MATLAB code and applied to the considered test cases. This tool allows calculating the phase velocity and the wavenumber for every direction and for every kind of laminate. This instrument, known as Semi-Analytical Finite Element (SAFE), can also return the dispersion curves and the frequency spectra for every direction of the laminate. Using this tool the polar plots reporting the wavenumbers, as function of the direction and for a given frequency, have been plotted for every plate modeled with the FE method. The behavior of the wave in composite plates is well represented by these plots.

To compare these plots and the results obtained from the FE analysis a post-processing operation has been applied on the displacements given by the FE analysis. Through the recursive use of the Fourier transform it has been possible to obtain, for a given frequency, the wavenumber value as function of the direction. The comparison between the results obtained using the FE approach and the polar plots returned by the SAFE approach is nearly perfect.

To definitely validate the achieved results an experimental analysis has been performed. Three plates have been manufactured at Politecnico in order to reproduce the laminates modeled with the FE. The experiment has been carried out at the Georgia Institute of Technology in Atlanta by means of a laser vibrometer. These experimental results have shown not only the anti-symmetric mode A_0 , which can be seen even in the FE model, but also the Symmetric mode S_0 and the shear horizontal mode SH_0 . Since the measures given by the vibrometer are the out-of-plane displacement histories in a series of point on the plate, i.e. the same output of the FE model, thus the same post-processing technique adopted for the FE model has been applied. Wavenumber plots have been compared with the same plot achieved by the SAFE approach. The overlapping of the two plots is very good for every plate and for every mode A_0 , S_0 and SH_0 . The only small difference is in the unidirectional fiber glass plate. In this plate the experimental anti-symmetric wave A_0 , along the 90° direction, i.e. the direction perpendicular to the fibres, presents a smaller wavenumber with respect to the curve given by the SAFE approach. However it should be noted that unidirectional laminates are rarely employed in engineering applications. Since the wavenumber polar

plots of the FE correspond to the polar plots achieved by the SAFE and that these latter correspond to the experimental polar plots, then it can be stated that the FE results given by the FE models correspond to the experimental results.

It can be stated that the propagation of anti-symmetric guided waves A_0 is correctly reproduced, for relevant engineering applications, by FE models of composite plates obtained through the use of the technique developed at Politecnico. This result has been achieved even if an aspect ratio more than one has been applied to the solid elements to reduce the number of degree of freedom and no damping has been considered.

Concluding, the present work has assessed and validated some modeling technique for representing wave propagation, including an evaluation of the possibility to employ large aspect ratio solid elements for wave propagation. The capability of qualitatively describing the wave scattering from a defect has been assessed. Limiting to the A_0 wave, the possibility to employ hybrid 2D/3D models for wave propagation analyses has been assessed. Then a semi-analytical method has been implemented and a comparison between FE, SAFE approach and experimental results has been carried out confirming that both the numerical approaches can reliably represent wave propagations. Finally, the post-processing technique that have been employed, basing on FFT algorithms, allowed a compact and meaningful comparison between the numerical and experimental results.

Among the future task there is the need for the improvement of the FE modeling technique to correctly reproduce the symmetric waves S_0 and the shear-horizontal waves SH_0 . Then great importance should be given to the study of scattering by means of the FE approach, especially for composite materials, in order to understand the behavior of guided waves in front of a delamination. When these ideas will be assimilated practical application of structural health monitoring could be designed.

Conclusioni e sviluppi futuri

L'obiettivo di questo lavoro è la validazione di un metodo ad elementi finiti per la corretta rappresentazione delle onde guidate in una piastra. Inizialmente è stata presentata la tecnica di modellazione insieme a tutti i suggerimenti per modellare questo fenomeno usando elementi solidi. Poi sono stati creati diversi modelli di piastre sia in materiale isotropo che in materiale composito usando questa tecnica e uno schema di integrazione nel tempo esplicito. La modellazione è stata eseguita prestando particolare attenzione alla riduzione del costo computazionale, che può facilmente raggiungere livelli non tollerabili. È stata valutata la possibilità di ridurre il numero di gradi di libertà utilizzando elementi solidi con un rapporto d'aspetto maggiore di 1. Inoltre è stato provato che il rapporto d'aspetto è effettivamente un parametro importante per la qualità dei risultati. Buoni risultati si possono ottenere con rapporti d'aspetto fino a 5, che rappresenta una notevole riduzione del numero di gradi di libertà necessari per la modellazione di un laminato strato per strato. Il confronto numerico è stato incentrato sulla misura del modo di Lamb anti-simmetrico A_0 . Le onde simmetriche S_0 possono comunque essere riprodotte correttamente dal modello sviluppato, come si è dimostrato nel test sulla diffusione (scattering). Questo test è stato eseguito per verificare la capacità del modello ad EF di riprodurre le onde che si generano dalla riflessione di un'onda S_0 contro un danno: in questo caso un foro parziale in una piastra di alluminio. I risultati ottenuti, sebbene non sia stata eseguita un'analisi approfondita dell'argomento, sono molto promettenti e motivano gli sforzi per eseguire una ponderata validazione della propagazione delle onde di Lamb nei compositi, dove il potenziale di una tecnica di health monitoring può essere pienamente sfruttato.

Successivamente si è applicata la tecnica, sviluppata al Politecnico, che impiega sia elementi solidi che elementi bi-dimensionali per la modellazione di materiali compositi e che ben rappresenta i danni interlaminari tra le lamine. Con questa tecnica sono stati creati tre modelli tali da riprodurre la maggior parte dei laminati possibili. Tali modelli sono: una piastra quasi-isotropa in carbonio con orientazione $[0^\circ, 45^\circ, 90^\circ, -45^\circ]_{2s}$ chiamata Plate1,

una piastra in fibra di vetro con orientazione $[0_2^{\circ}, 90_2^{\circ}]_s$ chiamata Plate2 e una piastra in fibra di vetro unidirezionale $[0_8^{\circ}]$ chiamata Plate3. Per il particolare approccio adottato in questi modelli, le onde simmetriche S_0 non si possono diffondere. Ciò è dovuto al materiale assegnato agli elementi solidi il quale non riesce a modellare le deformazioni nel piano con quelle fuori dal piano. Per tutti i modelli ad EF analizzati si sono misurate le storie temporali degli spostamenti fuori dal piano dei nodi posizionati sulla superficie superiore della piastra.

Per confrontare i risultati ottenuti si è deciso di implementare in un codice MATLAB un altro strumento in grado di calcolare, per qualunque tipo di laminato, l'andamento di grandezze come la velocità di fase o il numero d'onda in ogni direzione. Questo strumento noto come Semi-Analytical Finite Element (SAFE) è anche in grado di fornire le curve di dispersione e gli spettri di frequenza per una determinata direzione del laminato. In questo modo sono stati generati, per ogni piastra modellata ad EF, i grafici polari degli andamenti del numero d'onda in funzione della direzione di propagazione per la specifica frequenza di eccitazione. Questi grafici forniscono una buona indicazione del comportamento dell'onda in piastre di materiale composito.

Per consentire un confronto tra i grafici così ottenuti e gli spostamenti forniti dall'analisi ad EF, è stata eseguita su quest'ultimi un'operazione di processamento dei dati che, tramite l'uso ricorsivo della trasformata di Fourier, ha permesso di ricavare, per una determinata frequenza, l'andamento del numero d'onda in ogni direzione. Il confronto tra i risultati ottenuti dall'approccio ad EF e i grafici polari forniti dall'approccio SAFE mostrano una corrispondenza quasi perfetta.

Per poter avere una conferma definitiva dei risultati ottenuti è stata eseguita l'analisi sperimentale su tre piastre prodotte dal Politecnico con gli stessi materiali e le stesse orientazioni delle piastre modellate ad EF. L'analisi è stata condotta al Georgia Institute of Technology di Atlanta, utilizzando un vibrometro laser. I risultati ottenuti sperimentalmente hanno mostrato oltre alla presenza del modo A_0 , visibile anche negli EF, la presenza del modo simmetrico S_0 e del modo di taglio orizzontale SH_0 . La stessa tecnica di processamento dati utilizzata per gli EF è stata applicata a questi risultati, poichè ciò che viene misurato dal vibrometro laser sono le storie temporali degli spostamenti fuori dal piano su un certo numero di punti della piastra, esattamente come nel caso degli EF. I risultati di numero d'onda in funzione della direzione di propagazione sono stati confrontati con i grafici polari del SAFE, riscontrando una corrispondenza molto buona per tutte e tre le piastre e per tutti e tre i modi A_0 , S_0 e SH_0 . L'unica piccola discrepanza è stata riscontrata nella piastra in fibra di vetro unidirezionale, nella quale il modo anti-simmetrico A_0 in direzione 90° , ossia perpendicolarmente alle fibre, ha

un numero d'onda minore rispetto a quanto previsto dal SAFE. Tuttavia, bisogna notare che i laminati unidirezionali in applicazioni ingegneristiche sono raramente utilizzati. Quindi, dato che i grafici polari del numero d'onda degli EF corrispondono a quelli dati dal SAFE e che questi ultimi corrispondono a loro volta ai grafici polari ricavati dai dati sperimentali, si può affermare che i risultati dati dagli EF corrispondono a quelli sperimentali.

Si può quindi affermare che i modelli ad elementi finiti di piastre in materiale composito, realizzati con la tecnica sviluppata al Politecnico, sono stati in grado di riprodurre correttamente l'andamento delle onde guidate anti-simmetriche A_0 per le applicazioni ingegneristiche di rilievo. Questo risultato è stato raggiunto nonostante sia stato applicato agli elementi solidi un rapporto d'aspetto maggiore di 1, al fine di ridurre i gradi di libertà e non siano stati considerati effetti di smorzamento nei modelli numerici.

In conclusione il presente lavoro ha valutato e validato alcune tecniche di modellazione usate per rappresentare la propagazione di onde, oltre alla possibilità di utilizzare grandi rapporti d'aspetto per gli elementi solidi. Si è inoltre valutata la possibilità di descrivere qualitativamente lo scattering derivante da un difetto. Poi, limitatamente alle onde A_0 , è stata valutata la possibilità di usare un modello ibrido ad elementi 2D/3D per modellare la propagazione delle onde. In seguito un metodo semi-analitico è stato implementato, quindi è stato eseguito un confronto tra gli approcci ad EF, SAFE e i risultati sperimentali. Questo confronto ha confermato che entrambi gli approcci numerici riescono a rappresentare correttamente la propagazione delle onde guidate. Infine la tecnica di elaborazione dati usata, basata sull'utilizzo dell'algoritmo della FFT, ha consentito di confrontare in modo significativo i dati numerici e quelli sperimentali.

Tra gli sviluppi futuri, figura l'ottimizzazione della tecnica di modellazione adottata per poter riprodurre sia le onde simmetriche S_0 sia quelle di taglio orizzontale SH_0 . Poi grande importanza dovrebbe essere data allo studio dello scattering attraverso l'impiego di EF, specialmente per i materiali compositi, al fine di comprendere il comportamento delle onde guidate di fronte alla delaminazione. Quando questi concetti saranno assimilati allora si potrà procedere al progetto di sistemi di SHM.

Bibliography

- [1] C. R. Farrar and K. Worden, “An introduction to structural health monitoring,” *Philosophical transactions of the Royal Society A*, no. 365, pp. 303–315, 2007.
- [2] Z. Su, L. Ye, and X. Bu, “A damage identification technique for cf/ep composite laminates using distributed piezoelectric transducers,” *Composite Structures*, no. 57, pp. 465–471, 2002.
- [3] K. Diamanti, C. Soutis, and J. Hodgkinson, “Lamb waves for the non-destructive inspection of monolithic and sandwich composite beams,” *Composites: Part A*, no. 36, pp. 189–195, 2005.
- [4] S. Park, C.-B. Yun, and Y. Roh, “Damage diagnostics on a welded zone of a steel truss member using an active sensing network system,” *NDT&E International*, no. 40, pp. 71–76, 2007.
- [5] Z. Su, L. Ye, and Y. Lu, “Guided lamb waves for identification of damage in composite structures: A review,” *Journal of Sound and Vibration*, no. 295, pp. 753–780, 2006.
- [6] J. H. Lee and C. P. Burger, “Finite element modeling of laser-generated lamb waves,” *Computers and Structures*, vol. 54, no. 3, pp. 499–514, 1995.
- [7] K. Diamanti, C. Soutis, and J. Hodgkinson, “Detection of low-velocity impact damage in composite plates using lamb waves,” *Structural Health Monitoring*, vol. 3, no. 1, pp. 33–41, 2004.
- [8] K. Diamanti, C. Soutis, and J. Hodgkinson, “Piezoelectric transducer arrangement for the inspection of large composite structures,” *Composites: Part A*, no. 38, pp. 1121–1130, 2007.
- [9] C. Yang, L. Ye, Z. Su, and M. Bannister, “Some aspects of numerical simulation for lamb wave propagation in composite laminates,” *Composite Structures*, pp. 267–275, 2006.

- [10] Y. Lu, L. Ye, Z. Su, and C. Yang, “Quantitative assessment of through-thickness crack size based on lamb wave scattering in aluminium plates,” *NDT&E International*, no. 41, pp. 59–68, 2008.
- [11] O. Diligent, T. Grahn, A. Boström, P. Cawley, and M. J. S. Lowe, “The low-frequency reflection and scattering of the s_0 lamb mode from a circular through-thickness hole in a plate: Finite element, analytical and experimental studies,” *Journal of the Acoustical Society of America*, vol. 112, no. 6, pp. 2589–2601, 2002.
- [12] R. Basri and W. Chiu, “Numerical analysis on the interaction of guided lamb waves with a local elastic stiffness reduction in quasi-isotropic composite plate structures,” *Composite Structures*, no. 66, pp. 87–99, 2004.
- [13] K. F. Graff, *Wave motion in elastic solids*. Dover Publications, Inc., 1991.
- [14] J. L. Rose, *Ultrasonic waves in solid media*. Cambridge University Press, 1999.
- [15] J. D. Achenbach, *Wave propagation in elastic solids*. Dover Publications, Inc., 1984.
- [16] *Abaqus Analysis User’s Manual, Version 6.9-1*.
- [17] D. P. Flanagan and T. Belytschko, “A uniform strain hexahedron and quadrilateral with orthogonal hourglass control,” *International Journal for Numerical Methods in Engineering*, vol. 17, pp. 679–706, 1981.
- [18] I. Harari and F. Magoulès, “Numerical investigations of stabilized finite element computations for acoustics,” *Wave Motion*, no. 39, pp. 339–349, 2004.
- [19] S. H. Diaz Valdés and C. Soutis, “Real-time nondestructive evaluation of fiber composite laminate using low-frequency lamb waves,” *Journal Acoustical Society of America*, vol. 111, no. 5, pp. 2026–2033, 2002.
- [20] T. Grahn, “Lamb waves scattering from a circular partly through-thickness hole in a plate,” *Wave Motion*, no. 37, pp. 63–80, 2003.
- [21] M. Castaings, C. Bacon, B. Hosten, and M. V. Predoi, “Finite element predictions for the dynamic response of thermo-viscoelastic material structures,” *Journal of the Acoustical Society of America*, vol. 115, no. 3, pp. 1125–1133, 2004.

- [22] M. Drozd, E. Skelton, R. Craster, and M. Lowe, "Modeling bulk and guided waves in unbounded elastic media using absorbing layers in commercial finite element packages," *Review of Quantitative Nondestructive Evaluation*, vol. 26, 2007.
- [23] G. Neau, *Lamb waves in anisotropic viscoelastic plates. Study of the wave fronts and attenuation*. PhD thesis, L'Université Bordeaux I, 2003.
- [24] A. Airoidi, G. Sala, and P. Bettini, "Evaluation of a numerical approach for the development of interlaminar damage in composite laminates," *Composite Science and Technology*, vol. In Press, 2009.
- [25] A. Airoidi, G. Sala, and P. Bettini, "Evaluation of numerical approaches for the development of interlaminar damage in composite laminates," in *16th International Conference on Composite Materials. Kyoto, Japan*, 2007.
- [26] M. Cattaneo, "Modellazione della resistenza post-impatto di laminati in composito," Master's thesis, Politecnico di Milano, 2010.
- [27] B. Aalami, "Wave in prismatic guides of arbitrary cross section," *Journal of Applied Mechanics*, no. 40, pp. 1067–1072, 1973.
- [28] K. H. Huang and S. B. Dong, "Propagating waves and edge vibrations in anisotropic composite cylinders," *Journal of Sound and Vibration*, no. 96, pp. 363–379, 1984.
- [29] L. Gavrić, "Finite element computation of dispersion properties of thin-walled waveguides," *Journal of Sound and Vibration*, no. 173, pp. 113–124, 1994.
- [30] L. Gavrić, "Computation of propagating waves in free rail using a finite element technique," *Journal of Sound and Vibration*, no. 185, pp. 531–543, 1995.
- [31] A. C. Hladky-Hennion, "Finite element analysis of the propagation of acoustic waves in waveguides," *Journal of Sound and Vibration*, no. 194, pp. 119–136, 1996.
- [32] S. B. Dong and K. H. Huang, "Edge vibrations in laminated composite plates," *Journal of Applied Mechanics*, no. 52, pp. 433–438, 1985.
- [33] O. M. Mukdadi and S. K. Datta, "Transient ultrasonic guided waves in layered plates with rectangular cross section," *Journal of Applied Physics*, no. 93, pp. 9360–9370, 2003.

- [34] V. V. Volovoi, D. H. Hodges, V. L. Berdichevsky, and V. G. Sutyrin, “Dynamic dispersion curves for non-homogeneous, anisotropic beams with cross-section of arbitrary geometry,” *Journal of Sound and Vibration*, no. 215, pp. 1101–1120, 1998.
- [35] P. J. Shorter, “Wave propagation and damping in linear viscoelastic laminates,” *Journal of the Acoustical Society of America*, no. 115, pp. 1917–1925, 2004.
- [36] I. Bartoli, A. Marzania, F. Lanza di Scalea, and E. Viola, “Modeling wave propagation in damped waveguides of arbitrary cross-section,” *Journal of Sound and Vibration*, no. 295, pp. 685–707, 2006.
- [37] S. Finnveden, “Evaluation of modal density and group velocity by a finite element method,” *Journal of Sound and Vibration*, no. 273, pp. 51–75, 2004.
- [38] M. Bramanti, C. D. Pagani, and S. Salsa, *Matematica. Calcolo infinitesimale e algebra lineare*. Zanichelli, first ed., 2000.
- [39] The MathWork Inc., *MATLAB Reference Guide*.

Acknowledgments

I would like to express my gratitude to my supervisor, Ing. Alessandro Airoidi, whose competence and patience helped me in the writing of this thesis. I would also like to thank Prof. Giuseppe Sala for having accepted my nomination for this thesis and for the interest that he has been capable of transmitting for structures and composite materials.

A very special thanks goes out to Prof. Massimo Ruzzene and his staff: Nicole Apetre, Buli Xu, Matteo Senesi, Luca Airoidi, Filippo Casadei who have helped me in understanding the concepts behind the wave propagation and who have clearly explained the practical aspects of experimentation.

I can not forget to acknowledge all the math teachers I have found in my scholastic career: maestra Giuseppina, professoressa Ori, professoressa Zanola and professoressa Donini, whose teachings have addressed my interest in the scientific field.

I would also like to thanks my parents for the support they provided me through my entire life and my sister who makes me feel the elder brother.

I must also acknowledge a very important person to me: Elisa, without whose encouragement and infinite patience I would not have finished this thesis.

Last but not least I would like to thank all my friends: Arturo and his wife Elisa, Claudio, Francesca, Elena, Nicola, Francesco and my high-school classmate Carlo for their moral support and encouragement. Moreover a special thanks goes to my fellows at university: Alessio, Alberto and Matteo, who have helped me to pass more than one exam and with whom I have shared ideas and projects.

Ringraziamenti

Vorrei esprimere tutta la mia gratitudine al mio co-relatore Ing. Alessandro Airoidi, le cui competenze e la cui pazienza mi hanno aiutato nella stesura di questa tesi. Vorrei inoltre ringraziare il Prof. Giuseppe Sala per aver approvato la mia candidatura a svolgere questa tesi e per l'interesse che nel suo corso ha trasmesso verso le strutture e i materiali compositi.

Un ringraziamento speciale va poi al Prof. Massimo Ruzzene e a tutto il suo staff, Nicole Apetre, Buli Xu, Matteo Senesi, Luca Airoidi, Filippo Casadei che mi hanno aiutato a capire i concetti che si nascondono dietro la propagazione delle onde e mi hanno spiegato chiaramente gli aspetti pratici della sperimentazione.

Non posso poi dimenticare tutte gli insegnanti di matematica che ho incontrato nella mia carriera scolastica: la maestra Giuseppina, la professoressa Ori, la professoressa Zanola e la professoressa Donini, che grazie ai loro insegnamenti hanno indirizzato il mio interesse verso le materie scientifiche.

Vorrei poi ringraziare i miei genitori per tutto il supporto che mi hanno sempre dato e mia sorella, per la sua capacità di farmi sentire sempre un fratello maggiore.

Devo poi ringraziare una persona a cui tengo molto: Elisa, senza il cui continuo incoraggiamento e l'infinita pazienza non sarei stato in grado di completare questa tesi.

Infine vorrei ringraziare tutti i miei amici: Arturo e sua moglie Elisa, Claudio, Francesca, Elena, Nicola, Francesco e il mio compagno delle superiori Carlo sempre pronti a confortarmi in caso di bisogno o a festeggiare in caso di superamento degli esami. Inoltre un grazie speciale va ai miei compagni di università: Alessio, Alberto, Matteo che mi hanno aiutato a passare più di un esame e con i quali ho condiviso idee e progetti.